RAYLEIGH LIDAR STUDIES OF MESOSPHERIC INVERSION LAYERS AT POKER FLAT RESEARCH RANGE, CHATANIKA, ALASKA

By

Brita K. Irving

RECOMMENDED:

Advisory Committee Chair

Chair, Department of Atmospheric Sciences

APPROVED:

Dean, College of Natural Science and Mathematics

Dean of the Graduate School

August 13, 2012

Date

RAYLEIGH LIDAR STUDIES OF MESOSPHERIC INVERSION LAYERS AT POKER FLAT RESEARCH RANGE, CHATANIKA, ALASKA

A

THESIS

Presented to the Faculty

of the University of Alaska Fairbanks

in Partial Fulfillment of the Requirements

for the Degree of

MASTER OF SCIENCE

By

Brita K. Irving, B.S.

Fairbanks, Alaska

August 2012

Abstract

Rayleigh lidar observations at Poker Flat Research Range, Chatanika, Alaska (65°N, 213°E), have yielded density and temperature measurements from 40–80 km. These measurements have been made under clear nighttime skies since November 1997. This thesis presents a study of Mesospheric Inversion Layers (MILs) and lidar performance at Chatanika. MILs are identified and characterized in the 40–70 km altitude region on 55 of the 149 wintertime observations over two periods, November 1997 – April 2005 and November 2007 – March 2009, using a new detection algorithm. Investigation of the MILs compared with planetary wave activity as observed by satellite finds a strong correlation between the presence of MILs and the structure of the planetary waves. These two periods are marked by strong planetary wave activity and sudden stratospheric warming events. MILs are found to occur more frequently than previously reported at Arctic sites, but less frequently than at lower latitudes. In spring 2012 the existing lidar system was extended by incorporating a larger aperture telescope and higher power laser and field trials were conducted. The results from these field trails are presented and the ability of the new lidar system to extend the scope of future studies at Chatanika is assessed.

Table of Contents

Page

List of Figures

Page

List of Tables

Page

List of Appendices

Page

Acknowledgements

I would like to thank my advisor Dr. Richard Collins for the opportunity to work with the lidar group, for his excellent advice, constant guidance, and unwavering support of my research and involvement in the UAF Women's Hockey team. I thank my committee members Dr. Kenneth Sassen, Dr. Ruth Lieberman, and Dr. Uma Bhatt for their advice and encouragement during my graduate years at UAF. The lidar data presented in this thesis would not be possible without the dedication from students previously working at the Lidar Research Laboratory, and current students Seth Robinson, Matthew Titus, and Cameron Martus, and for the never ending support from Dr. Collins. I thank the staff of Poker Flat Research Range for their assistance and maintenance of the Lidar Research Laboratory. I will always be grateful to the faculty, staff, and students of the Department of Atmospheric Sciences and Geophysical Institute. Special thanks to the Chair of the Department of Atmospheric Sciences Dr. Nicole Mölders for supporting myself and the UAF Women's Hockey team and for her helpful comments on this thesis, Barbara Day for her patience and assistance through the years, and Flora Grabowska and all the wonderful librarians of the Keith B. Mather Library.

I thank the National Science Foundation and the National Aeronautics and Space Administration for their support of this study. Thanks to the Coupling, Energetics and Dynamics of Atmospheric Regions (CEDAR) program for supporting my attendance of the 2009 and 2011 CEDAR Workshop in Santa Fe, NM. I also would like to thank Dr. Kohei Mizutani and National Institute of Information and Communications Technology for their support of the Lidar Research Laboratory.

Many thanks to Brentha Thurairajah for all her help and knowledge over the years, Jeanie Talbot and Ketsiri Leelasakultum for their encouragement and conversation, and Matthew Titus for his help and knowledge during developmental work on the lidar systems and for his comments on this thesis. I would like to thank David Hooper for his patience, support, inspiration, and encouragement during my MS research, and for his helpful comments on this thesis.

Last, but certainly not least, I would like to thank my mom and dad (Janlee and Ken Irving), and my sister and brother (Bonnie and Geoffrey Irving), for their constant support and love. Thanks to the University of Alaska Women's Hockey team for several wonderful years and special thanks our Coach, Scott Vockeroth for his dedication, and my closest friend, Shawna Jusczak, for everything.

Dedication

To

My mom, dad, brother and sister.

Chapter 1. Introduction

1.1. The Arctic middle atmosphere

The Earth's atmosphere is divided into distinct spheres separated by "pauses", the closest of which is the troposphere from the ground to ~15 km. Above the tropopause, the stratosphere extends to the stratopause at ~50 km. Above the stratopause the mesosphere extends to ~90 km. Finally, above the mesopause the thermosphere extends upward to space. The heights of these spheres vary geographically and seasonally. For instance, the tropopause reaches a maximum height of ~17 km at the equator then decreases with latitude until reaching a minimum of ~10 km at the poles [e.g., Wallace and Hobbs, 2006]. The study of the vertical thermal structure of the atmosphere contributes to the understanding of such phenomena as the ozone layer, noctilucent clouds (NLCs), polar stratospheric clouds (PSCs), elevated stratopause events, stratospheric sudden warmings (SSWs), the aurora, airglow, and mesospheric inversion layers (MILs). The vertical temperature structure from the Extended Mass Spectrometer Incoherent Scatter (MSISE-90) model [Hedin, 1991] during solstice conditions at 65°N is shown in Figure 1.1 with regions of interesting atmospheric phenomenon highlighted.

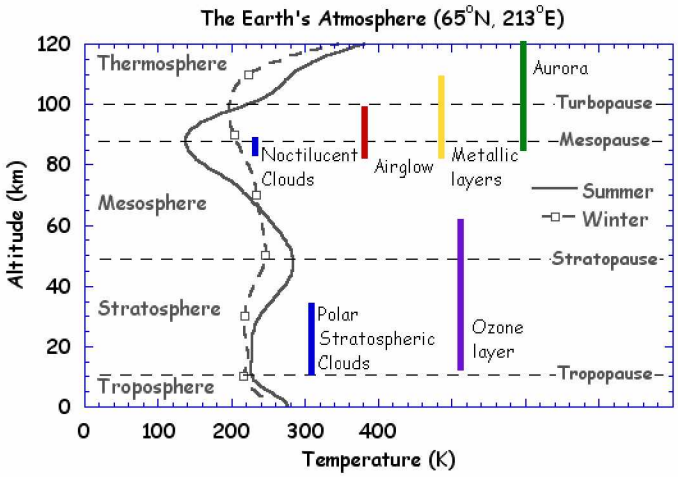

Figure 1.1. Temperature of the Earth's atmosphere as a function of height from the MSISE-90 model for 21 June 2011 and 22 December 2011 at (65°N, 213°E).

The temperature in the troposphere decreases with increasing height at a rate of approximately 6 K km^{-1}. This thermal structure is maintained through a balance between infrared heating and radiative cooling, large-scale heat transport by large-scale weather systems, and vertical transport of latent and sensible heat away from the surface by small-scale turbulence. Above the tropopause, the temperature gradient reverses as a result of radiative heating due to the absorption of solar ultraviolet (UV) radiation by ozone (O_3). The temperature then decreases with height in the mesosphere at about the same rate as the troposphere due to reduced solar heating. In the thermosphere, temperatures increase with height due to the absorption of solar UV radiation by trace amounts of atomic oxygen [e.g., Holton, 2004; Wallace and Hobbs, 2006].

Without dynamic eddy mixing, the atmosphere would relax to a radiative state in which the temperature would trail the annual solar heating cycle with a uniform increase from the winter pole to summer pole. In this state, the circulation would consist of a zonal mean zonal flow in the thermal wind balance with the meridional temperature gradient. In such a circulation, there would be no meridional or vertical circulation, and no exchange between the stratosphere and troposphere. In fact, the eddy-driven circulation has both meridional and vertical components that cause large departures from the atmosphere's radiatively determined state [Holton, 2004]. An example of this circulation is the cold summer polar mesopause and warm winter mesopause that is clearly evident in the temperature profiles in Figure 1.1. From winter to summer the stratopause warms by 20 K while the mesopause cools by 30 K.

The middle atmosphere extends from above the tropopause to approximately 100 km, where atmospheric constituents are well mixed by eddy processes. The upper boundary of the middle atmosphere is near the turbopause (dashed line at 100 km in Figure 1.1), above which the middle atmosphere is dominated by molecular diffusion. Here, the chemical composition of the atmosphere varies from species to species. Although weather and climate are primarily due to processes occurring in the troposphere, which contains approximately 85% of the mass and 99% of the water vapor of the Earth's

atmosphere, the middle atmosphere also plays an important role. The troposphere and middle atmosphere are linked through dynamical and radiative processes, and through the exchange of trace substances important to the photochemistry of the O_3 layer [e.g., Holton et al., 1995].

The circulation of the middle atmosphere is driven by seasonal variation in solar heating and wave forcing, with westerly zonal mean winds in the winter hemisphere and easterly zonal mean winds in the summer hemisphere. After the autumnal equinox, the stratosphere at high latitudes cools due to the emission of thermal radiation and reduced incoming solar radiation. The meridional thermal gradient drives a pressure gradient between the pole and midlatitudes that, along with the Earth's rotation, creates a circumpolar belt of westerly winds referred to as the polar vortex, or polar night jet. The polar vortex is a synoptic scale cyclone that isolates cold air inside the vortex and inhibits mixing with warmer mid-latitude air masses. Within the vortex temperatures can fall below 195 K, allowing PSCs to form. PSCs act as catalysts for O_3 depletion by providing a surface for heterogeneous reactions to take place [Solomon et al., 1986]. Isolation within the vortex further enhances O_3 depletion by denitrifying the air within the vortex, a necessary chemical condition for O_3 depletion [e.g., Toon and Turco, 1991; Schoeberl and Hartmann, 1991].

With the discovery of the Antarctic ozone hole in the 1980's [Farman et al., 1985], there was a surge of scientific interest and research regarding O_3 depletion and middle atmospheric circulation. O_3 is the primary reason the Earth's surface is not constantly bombarded with UV radiation from the sun. The Antarctic O_3 hole is remotely located, but as the vortex splits and dissipates in the spring the depleted air is carried to lower latitudes and poses a health threat [e.g., Atkinson et al., 1989]. Approximately 70% of the O_3 above the Antarctic (approximately 3% of the Earth's total) is lost during September and October [Toon and Turco, 1991]. In spring 2011, unprecedented ozone depletion that reached levels similar to the Antarctic ozone hole was recorded in the Arctic [Manney et al., 2011]. The record ozone loss has attracted considerable attention

due to its implications for a major health risk in the highly populated Northern Hemisphere.

The Arctic middle atmosphere has gained widespread attention in recent years due to its remarkable inter-annual variability [e.g., Manney et al., 2005; 2009; 2011]. Although initiatives focused on the Arctic such as the International Polar Year (IPY) [Collins, 2004; ICSU, 2004; NRC, 2004] have strengthened our knowledge of the atmospheric circulation in this region, our present understanding of what drives such variability is incomplete [Newman et al., 2001; Manney et al., 2011]. The study of phenomena such as SSWs, elevated stratopause events, and MILs are necessary to developing a thorough understanding of the middle atmospheric [e.g., Fritts and Alexander, 2003; Meriwether and Gerrard, 2004; Chandran et al., 2011; de la Torre, 2012].

1.2. The wave-driven circulation of the middle atmosphere

Atmospheric waves play a major role in the circulation of the middle atmosphere and have a profound influence on the temperature structure. Waves can propagate vertically and horizontally from wave sources to regions where transience, nonlinear wave breaking, or dissipation causes momentum transfer to the mean flow [Holton and Alexander, 2000]. Wave transience is the local growth or decay of wave amplitude, and dissipation can be either radiative or turbulent. Atmospheric wave motions result from a balance between inertia and restoring forces acting on fluid parcels displaced from their equilibrium longitudes or altitudes [Holton and Alexander, 2000]. Gravity waves, sometimes referred to as buoyancy waves, are small scale waves with horizontal wavelengths on the order of ten to hundreds of kilometers whose restoring force is buoyancy. Topography is one of the main sources of vertically propagating gravity waves, known as mountain or topographic waves. Planetary-scale Rossby waves (henceforth referred to as planetary waves) are generated by large-scale orography and land-sea contrast. They are large scale waves, on the order of $\sim 10^4$ km, whose restoring force is the variation of the Coriolis parameter with latitude, or the meridional gradient of

potential vorticity known as the β-effect [e.g., Salby, 1996; Holton and Alexander, 2000; Holton, 2004].

The phase speed of planetary waves is westward relative to the mean flow, and can only propagate vertically in the winter hemisphere when the westerly winds are weaker than a critical value (e.g., $\bar{u} = 0$ for quasistationary planetary waves), dependent on the horizontal scale of the waves [Charney and Drazin, 1961]. For planetary waves, wave breaking represents an irreversible process in which the wave deposits its momentum and energy into the system. Upward propagating planetary waves grow in amplitude as the atmospheric density decays with height. Therefore, at some altitude the disturbance amplitude will become so large that overturning and dissipation must occur. The irreversible deformation of material contours during planetary wave breaking is responsible for the stratospheric surf zone (dashed lines in Figure 1.2) [McIntyre and Palmer, 1984], has been shown to cause SSWs [Matsuno, 1971], and is one of the proposed formation mechanisms of MILs [Wu, 2000; Salby et al., 2002].

The zonal phase progression of gravity waves can be either westward or eastward with parcel oscillations perpendicular to the phase progression. Analogous to planetary waves, gravity wave amplitudes strengthen in the mesosphere and instability can occur when the amplitude disturbance becomes large. Wave breakdown caused by convective instability can mix through deep layers and may lead to substantial changes in the local chemical composition [Holton and Alexander, 2000; Fritts and Alexander, 2003]. Gravity wave breaking forces accelerations in the background flow and "drags" the flow toward the phase speed of the wave. The filtering of vertically propagating gravity waves by stratospheric winds allows westward propagating waves to propagate through the winter stratosphere, while only eastward winds with zonal phase speeds larger than the maximum wind speed are transmitted. The opposite is true for the summer stratosphere, and results in an eastward drag force exerted in the summer mesosphere and a westward drag force in the winter mesosphere. In the mesosphere, the mean zonal wind distribution

is maintained by the meridional drift, a consequence of this strong gravity wave forcing [Holton and Alexander, 2000], shown in Figure 1.3.

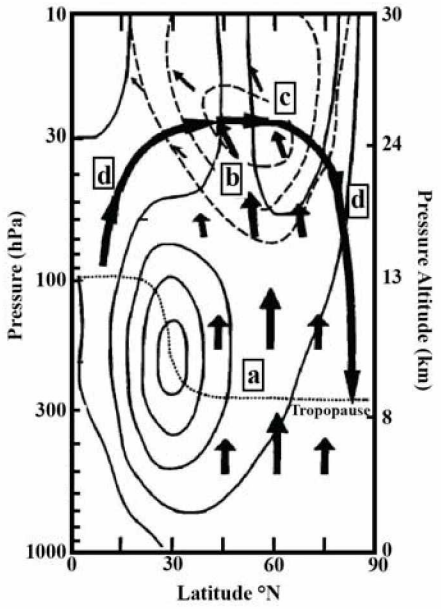

Figure 1.2. Schematic illustration of January-February stratospheric circulation and eddy heat fluxes (adapted from Newman et al. [2001]). Shown are regions of (a) planetary waves propagating into the stratosphere, (b) slowly refracting toward the equator, (c) depositing easterly momentum, and (d) inducing a residual circulation that causes uplift in the tropics and sinking in the polar region. Short arrows illustrate the wave propagation and the thick line with arrows shows the residual circulation. The thin solid lines show the wind speed, the dotted line shows the tropopause, and the dashed line shows the EP flux divergence.

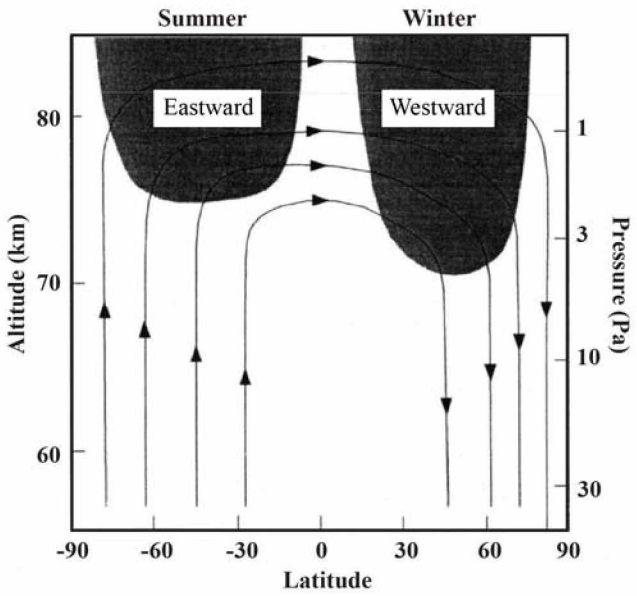

Figure 1.3. Schematic illustration of the solstice season pole-to-pole wave-driven transport circulation in the mesosphere (adapted from Holton and Alexander [2000]). Shading shows regions of zonal forcing by gravity wave breaking.

Planetary wave forcing leads to an equator-to-pole downward circulation in the winter hemisphere (Figure 1.2), known as the Brewer-Dobson circulation. Gravity wave forcing leads to a pole-to-pole circulation (Figure 1.3) from the summer to winter pole [Houghton, 1978]. In the middle atmosphere, the planetary wave forced circulation is responsible for transport of critical species such as O_3 and water vapor, but is absent in summer due to easterly mean winds. The gravity wave induced circulation is responsible for the cooling of the polar summer mesopause and the warming of the polar winter stratopause, visible in Figure 1.1 [e.g., Holton and Alexander, 2000; Fritts and Alexander, 2003]. Maximum O_3 loss in the Arctic polar vortex coincides with the return of sunlight in March, which initiates the photolysis of O_3. The interannual variability of March stratospheric temperatures in the Arctic is closely related to the January-February eddy heat flux caused by planetary waves [Newman et al., 2001]. The eddy heat flux is also correlated with the stratospheric momentum flux, Eliassen-Palmer (EP) flux divergence, and zonal mean wind. EP flux is a representation of the atmospheric eddy-mean flow

interaction and provides a measure of the zonal-forcing of the zonal mean flow. Negative EP flux divergence corresponds to the westward zonal force exerted by eddies on the atmosphere [Holton, 2004].

Figure 1.2 is a schematic illustration of the Northern Hemisphere January-February eddy heat flux adapted from Newman et al. [2001]. Upward propagation of planetary wave activity into the stratosphere (Figure 1.2a) is represented by large eddy heat fluxes. As planetary waves propagate upward, they encounter the polar vortex and can be refracted equatorward where they deposit easterly momentum (Figure 1.2b). This momentum deposition is balanced by a northward residual circulation (Figure 1.2c) which decelerates the polar night jet. This wave induced meridional residual circulation causes rising motion in the tropics and sinking motion at the poles (Figure 1.2d) [see Newman et al., 2001 and references therein]. Thus, if midwinter planetary wave activity is weak, there is little deceleration of the polar night jet, which leads to a cold stable polar vortex in March. A stronger and more stable vortex in the spring enables temperatures to fall low enough for more PSCs to form and for longer periods of time, enhancing O_3 depletion [e.g., Toon and Turco, 1991; Schoeberl and Hartmann, 1991].

The Arctic middle atmosphere is difficult to characterize due to the nonlinear wave-wave and wave-mean-flow interactions that result in the zonal asymmetric wintertime circulation. SSWs, an example of the wave-mean flow interaction, are caused by the interaction between upward propagating planetary waves and the zonal polar stratospheric flow. The mechanism for SSWs was first proposed by Matsuno [1971] and their occurrence is characterized by a displacement of the polar vortex, weakening of the zonal mean zonal flow, and an asymmetric stratospheric circulation. SSWs are defined as major when at the 10 hPa level, or below, the zonal mean temperature increases poleward of 60°N and the zonal mean zonal wind reverses [Labitzke, 1972] and minor when no wind reversal takes place. A contemporary example of an Arctic SSW was presented by Chandran et al. [2011] using a case study approach of a major SSW (Figure

1.4) followed by an elevated stratopause in the free running Whole Atmosphere Community Climate Model (WACCM).

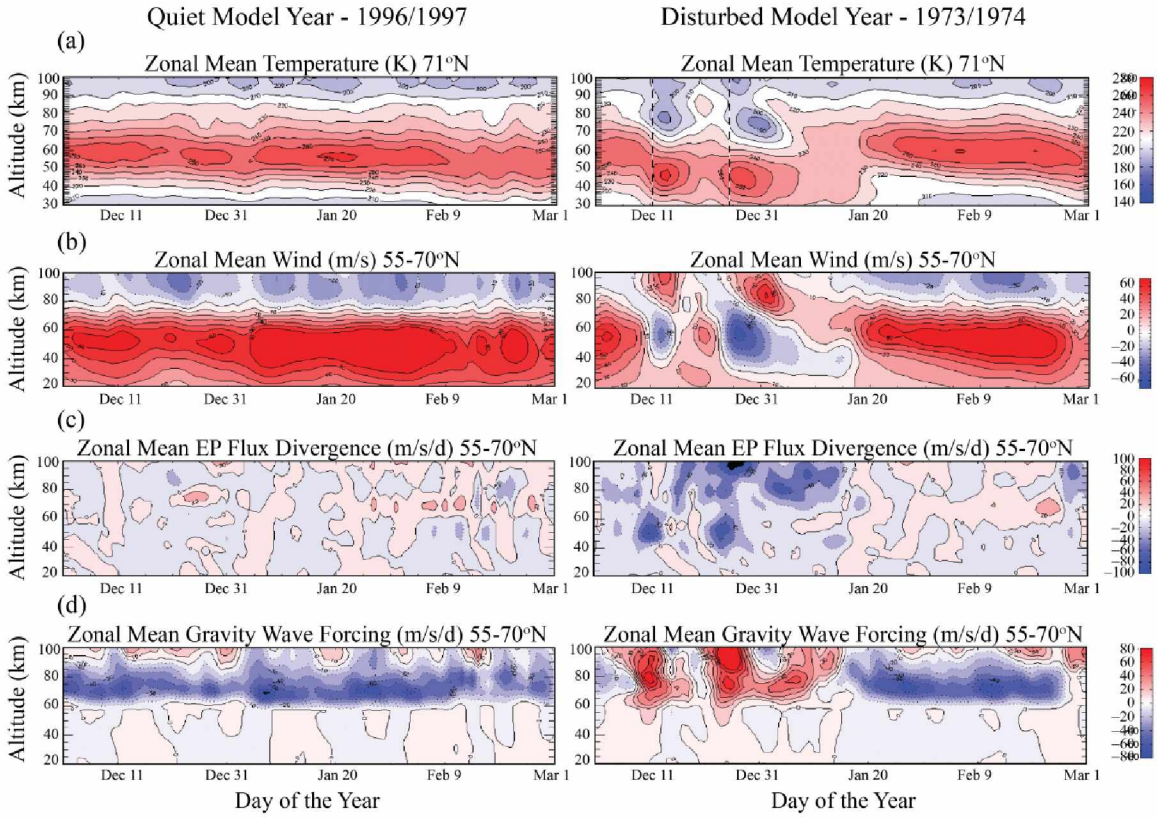

Figure 1.4. The zonal mean (a) temperatures at 70°N with dashed line indicating start of a SSW, (b) wind, (c) EP flux divergence, and (d) gravity wave forcing averaged for 55–70°N for (left) model year 1996/1997 and (right) model year 1973/1974 plotted as a function of altitude and day. In the bottom three panels, red (positive) contours denote eastward flow/forcing and blue (negative) denote westward (adapted from Chandran et al. [2011]).

During the dynamically quiet winter in the WACCM model year 1996/1997 (left) the zonal mean temperature (Figure 1.4a) behaves as a standard atmosphere, with a maximum temperature at the stratopause near 55 km and temperatures decreasing through the mesosphere. The zonal mean wind (Figure 1.4b, left) shows a strong eastward jet in the stratosphere with speeds greater than 60 m/s and winds reversing near

80 km to westward winds in the mesosphere. There is weak planetary wave forcing (Figure 1.4c, left) throughout the year with mid-winter EP flux divergence values generally less than ±10 m/s/d. Westward gravity wave forcing (Figure 1.4d, left) reaches a maximum of ~50 m/s/d in the mesosphere between 60 and 80 km. The WACCM model year 1996/1997 represents a dynamically quiet year where the stratospheric jet remains strong and eastward without reversals, contrary to 1973/1974 (Figure 1.4b, right).

The zonal mean temperature for the disturbed WACCM model year 1973/1974 (Figure 1.4a, right) shows a stratopause near 60 km through the beginning of December. On December 11th the stratopause warms and lowers in altitude to 46 km and on December 26th the stratopause again warms with maximum temperatures at 45 km. Both warming events are followed by a cooling of the stratopause and then a nearly isothermal atmosphere between 30 and 75 km from approximately January 10–January 17. Preceding both SSW is strong westward planetary wave forcing, with EP flux divergence values reaching -60 m/s/d. The strong westward planetary wave forcing reverses the stratospheric eastward jet to westward and induces a poleward and downward circulation, leading to adiabatic warming. The westward stratospheric jet allows for eastward propagating gravity waves to penetrate through the stratosphere and the eastward gravity wave forcing (Figure 1.4c, right) then reverses the mesospheric winds from westward to eastward. The eastward winds in the mesosphere result in an equatorward and upward flow. An elevated stratopause forms near 70 km following the SSWs and gradually relaxes down to ~55 km by March 1st. As westward gravity wave forcing returns and strengthens after ~January 17th, poleward and downward flow is re-established and the stratopause warms and lowers through the wave-drive diabatic descent.

The study by Chandran and co-workers demonstrates the complexity and variability that wave-wave and wave-mean flow interactions, and their nonlinear feedbacks have on the Arctic middle atmosphere [Chandran et al., 2011]. Direct observations of the wave-driven middle atmosphere are essential in furthering our understanding of the

dynamically driven Arctic, and to the development of models such as WACCM. Located in the Western Arctic, Chatanika is a natural laboratory where the understanding of wave-breaking, turbulence, and instability is advanced. Its location provides a unique opportunity to study wave-mean flow interactions, interactions between large and small-scale dynamical processes, and feedbacks from small-scale processes on the large-scale circulation in a region where the wintertime circulation is greatly influenced by the Aleutian anticyclone and polar vortex. Recent studies have found that during periods of strong planetary wave amplitudes and negative EP flux divergence, interactions between the Aleutian anticyclone and the polar vortex lead to their irreversible intertwining [Harvey et al., 2002; Thurairajah et al., 2010a; 2010b; Chandran et al., 2011]. These findings point to the Western Arctic atmosphere as a hub for planetary wave activity and subsequent planetary wave breaking.

MILs are understood to be a signature of nonlinear wave-wave and wave-mean-flow interactions and are important to study for two primary reasons: stability and energy transfer. The mechanism responsible for the formation of MILs is still ambiguous, although many have been proposed [see recent review by Meriwether and Gerrard, 2004]. MILs are identified as a layer of increasing temperature in the mesosphere, where temperatures typically decrease with height [Schmidlin, 1976]. MILs are so named because their appearance is similar to inversions capping the diurnally driven atmospheric boundary layer [Meriwether and Gerrard, 2004]. As temperatures increase on the bottom side of the MIL, atmospheric stability is increased and vertical mixing is reduced. As temperatures decrease on the topside of the MIL, atmospheric stability decreases and can approach instability at the adiabatic lapse rate. The instability above a MIL can lead to convective and/or dynamic instability and support the development of turbulence. Indeed, MILs with topside lapse rates ($-\partial T/\partial z$) approaching the adiabatic lapse rate (-9.8 K km^{-1}) have been reported [e.g., Whiteway et al., 1995; Cutler et al., 2001; Duck et al., 2001; Duck and Greene, 2004]. The generation of turbulence in the wintertime atmosphere is important in quantifying the impact of space radiation on the atmosphere. Current model studies show that turbulent transport is necessary, in addition

to the downward wave-driven circulation, for the transport of nitrogen compounds produced by energetic particle precipitation from the thermosphere into the mesosphere where they contribute to ozone depletion [Smith et al., 2011]. This transport is critical in understanding how meteorological processes control the impact of space processes on the Earth's atmosphere.

Understanding energy transport in the middle atmosphere provides further motivation for the investigation of MILs. In addition, MILs have a profound impact on the propagation of gravity waves in the mesosphere [e.g., Taylor et al., 1995; Dewan and Picard, 1998; Dewan and Picard, 2001]. Atmospheric wave breaking is the primary method by which energy is transferred up from the lower atmosphere and has been proposed as the formation mechanism of MILs [e.g., Meriwether and Gerrard, 2004; Gan et al., 2012 and references therein]. Investigation of MILs has historically relied on satellite and lidar data and a comprehensive understanding of the phenomena is incomplete. MILs have been reported from the equator and subtropics [e.g., Dao et al., 1995; Fechine et al., 2007] to high latitudes [e.g., Cutler et al., 2001; Duck and Greene, 2004], and with lifetimes ranging from days [e.g., Salby et al., 2002; Gan et al., 2012] to hours [e.g., Collins et al., 2011]. The geographic and temporal variability of MIL characteristics point to multiple formation mechanisms and illustrates the difficulty in elucidating their complete physical understanding.

1.3. Rayleigh lidar

Lidar is an acronym for LIight Ranging And Detection [Middleton and Spilhaus, 1953]. Analogous to optical radar, lidar is a form of active remote sensing that measures the laser light backscattered from a target molecule or atom. Rayleigh lidar systems measure the Rayleigh scattered light from air molecules in the cloud and aerosol free region of the middle atmosphere. Rayleigh scatter is defined as the scattering of electromagnetic radiation by particles smaller than the wavelength of radiation [Strutt, 1899].

Before the technique of temperature measurement by Rayleigh lidars was developed, the ~30 to 90 km altitude range accessible to Rayleigh lidar posed a challenge to researchers interested in the aeronomy of the middle atmosphere [Hauchecorne and Chanin, 1980]. Weather balloons pop at ~25 km, nadir pointing satellites are generally limited to below 55–60 km and above 200 km, radars face a lack of scattering media, airglow imagers observe only thin layers (e.g., the hydroxyl (OH) layer from ~84 to 94 km [Baker and Stair, 1988; Brinksma et al., 1998]), and rockets are expensive and provided only instantaneous measurements. In 1938, cloud base heights were determined for the first time using pulses of light [Bureau, 1946]. Elterman [1951] used a searchlight to sound the lower and middle atmosphere, and was the first to use the lidar integration technique to measure atmospheric temperatures. Kent et al. [1967] reported the first measurements of atmospheric constituents made with a Q-switched laser, and Hauchecorne and Chanin [1980] were the first to obtain a temperature measurement between 35 and 70 km. Today, Rayleigh lidar is a robust measurement technique and has contributed extensively to the understanding of the middle atmospheric composition and circulation [Weitkamp, 2005]. Further information on lasers is available in Verdeyen [1981] and Silfvast [1996], and on lidar methods and applications in atmospheric science in Measures [1984], Fujii and Fukuchi [2005], and Weitkamp [2005].

The National Institute of Information and Communications Technology (NICT) Rayleigh lidar observations at Poker Flat Research Range, Chatanika, Alaska (65°N, 213°E), have yielded density and temperature measurements from 40–80 km. These measurements are distributed between August and May and have been made under clear nighttime skies since November 1997. Rayleigh lidar observations at PFRR are used to study the temperature structure over Chatanika [e.g., Thurairajah et al., 2009], as well as the wave-driven circulation and turbulence [e.g., Wang, 2003; Collins and Smith, 2004; Thurairajah et al., 2010a; 2010b; Collins et al., 2011; Nielsen et al., 2012], and phenomena such as NLCs [e.g., Collins et al., 2003; Collins et al., 2009; Taylor et al., 2009; Kelley et al., 2010; Varney et al., 2011].

1.4. Scope of this study

In this thesis I present a scientific study of MILs observed by lidar and a technical study of the extension of the lidar system at Chatanika. Based on these studies, I show how the extended lidar system will broaden the scope of future studies at Chatanika.

In Chapter 2, I review the principles and technique of Rayleigh lidar. I present the lidar equation used for temperature retrievals from 40 km to 80 km and its application to study atmospheric structure over Chatanika. The NICT Rayleigh lidar system and system performances at Chatanika are reviewed.

In Chapter 3, I present results of the field tests I conducted during the extension of the NICT Rayleigh lidar system in spring 2012. I assess the ability of this new lidar system, which incorporates a larger aperture telescope and higher power laser, to extend the scope of future studies at Chatanika. I investigate the nonlinear response in the detector electronics below 50 km and their effects on the lidar temperature retrieval.

In Chapter 4, I present a climatology of MILs observed at Chatanika based on observations made over a twelve year period. Their relationship to the planetary wave structure is examined based on satellite measurements made over a six year period. Geopotential height and temperature data from the Sounding of the Atmosphere using Broadband Emission Radiometry (SABER) instrument on the Thermosphere Ionosphere Mesosphere Energetics Dynamics (TIMED) satellite are used to study the planetary wave field at 65°N.

In Chapter 5, I summarize the key findings of my study and present conclusions. Direction and suggestions are given for future studies of MILs and development of the Rayleigh lidar at the Lidar Research Laboratory, PFRR, Chatanika, Alaska.

Chapter 2. Principles and Techniques of Rayleigh lidar

2.1. NICT Rayleigh lidar

The National Institute of Information and Communications Technology (NICT) Rayleigh lidar was deployed at Poker Flat Research Range (PFRR), Chatanika, Alaska (65°N, 213°E) in November 1997. The NICT Rayleigh lidar was deployed by researchers from NICT and the Geophysical Institute of the University of Alaska Fairbanks (GI–UAF) as part of the Alaska project. The goal of the Alaska project was to establish a comprehensive measurement system capable of enduring and documenting the Arctic environment [Mizutani et al., 2000; Murayama et al., 2007]. The Rayleigh lidar system was initially installed in the Optics Laboratory (OL) at PFRR. The Rayleigh lidar was relocated to the Davis Science Center, PFRR, in April 1999 while the OL was demolished and the Lidar Research Laboratory (LRL) was built on the OL site. The lidar was installed in LRL in July 2000 and has operated there since.

A detailed schematic of the NICT lidar system is shown in Figure 2.1 and the specifications of the system are listed in Table 2.1. The NICT Rayleigh lidar transmitter consists of a laser, a laser beam expander (BE), a beam steering mirror (BSM), and a laser pulse detector (LPD), consisting of a laser diode. The NICT lidar system laser is a Nd:YAG Continuum® Powerlite 8020 Q-switched laser operating at a repetition rate of 20 pulses-per-second (pps) and with a wavelength of 532 nm. Further information on Nd:YAG lasers can be found in current textbooks [e.g., Verdeyen, 1981; Silfvast, 1996]. The telescope used in the receiver system is a classic Newtonian telescope with a 62 cm diameter (further information on astronomical optics can be found in Schroeder [2000]).

Table 2.1. NICT Rayleigh lidar system specifications.	
Transmitter	
Laser	Nd:YAG
Model	Continuum Powerlite 8020
Wavelength (λ_L)	532 nm
Repetition Rate (R_L)	20 Hz
Pulse Energy (E_L)	375 – 460 mJ
Pulse Width	5 – 7 ns
Line Width	1.0 cm^{-1} (28 pm, 30 GHz)
Beam Expander	× 10
Divergence	0.45 mrad
Receiver	
Telescope	Newtonian
Outer Diameter	620 mm
Inner Diameter	200 mm
Collecting Area	0.270 m^2
Range Resolution	75 m
Optical Bandwidth	0.3 nm
Field of view (FOV)	1 mrad
Detector	Photomultiplier Tube
Model	Hamamatsu R3234–01
Pulse duration	5 ns
Dark Count	50 – 150 counts/second
Preamplifier Gain	× 5
Model	Stanford Research Systems SR445
Bandwidth	DC to 300 MHz
Digital Recorder	Multichannel Scalar
Model	Ortec Turbo MCS T914
Maximum Count Rate	150 MHz

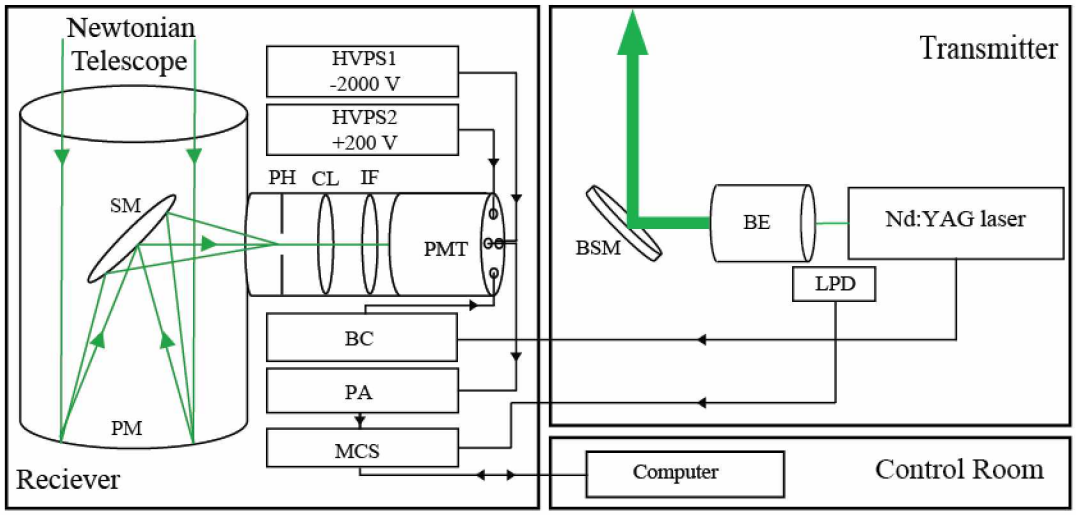

Figure 2.1. Schematic diagram of the NICT Rayleigh lidar system at PFRR, Chatanika, Alaska (65°N, 213°E).

BC – Blanking Control
BE – Beam Expander
BSM – Beam Steering Mirror
CL – Collimating Lens
HVPS – High Voltage Power Supply
IF – Interference Filter
LPD – Laser Pulse Detector
MCS – MultiChannel Scalar
PA – Pre-Amplifier
PH – Pin Hole
PM – Primary Mirror
PMT – Photo Multiplier Tube
SM – Secondary Mirror

The Nd:YAG laser emits a pulse of light in a beam that passes through the beam expander (BE). The expanded beam is reflected by the beam steering mirror (BSM) into the sky. Photons of light that are Rayleigh scattered in the atmosphere are detected by the telescope. The light incident on the telescopes primary mirror (PM) is reflected to the secondary mirror (SM). The light is reflected from the SM through the pinhole at the focal point of the telescope. The use of the pinhole defines the telescopes field-of-view (FOV). The light within the telescopes FOV passes the pinhole and is collimated by the collimating lens (CM). The telescope FOV is determined by the pinhole (PH) placed in front of the photomultiplier tube (PMT). The collimated light at 532 nm passes through the interference filter (IF) where it is focused on the PMT. Note: previous system descriptions [e.g., Wang, 2003; Nadakuditi, 2005] included a beam splitter before the

interference filter. The beam splitter was taken out in early 2008 when Resonance lidar measurements were made through a separate telescope [Light, 2009].

The transmitter communicates with the receiver system through the laser pulse detector and the lasers Q-switch. The Q-switch signal triggers the blanking control (BC) to transmit a pulse of 150 μs duration (known as a gate pulse) to the PMT (a general discussion of PMTs can be found in Hamamatsu Photonics [2005; 2006]). The gate pulse biases the first dynode of the PMT by +200 V (HVPS2) above its normal operating voltage of -2000 V (HVPS1), reducing the gain of the PMT by a factor of greater than 10^6. The gate pulse acts as electronic blanking causing return signals from altitudes below ~25 km to be detected at low gain and allows for the detection of high altitude signal returns at high gain. The LPD detects the transmitted laser pulse and triggers the multichannel scalar (MCS), a high-speed counter, to count the incoming PMT pulses in a given time window at rates up to 150 MHz. The time window determines the spatial resolution. For example, a bin time of 0.5 μs results in a 75 m vertical resolution. The current signal from the PMT is first amplified by the pre-amplifier (PA) before being sent to the MCS. The MCS typically records 4096 range bins, resulting in an echo profile from the ground to ~300 km. The next laser pulse triggers the next MCS profile acquisition which is added coherently to the previous one. The profiles are added together for a predetermined number of laser pulses, typically 1000 or 2000, to yield a single raw data profile. The single raw data profile is transferred to the computer where it is stored and then initiates the MCS to begin a new profile on the next laser pulse.

Nighttime lidar observations at PFRR are taken under clear sky conditions between August and May with the majority of observations taken between October and March. These observations have yielded temperature measurements of the Arctic middle atmosphere [Thurairajah et al., 2009]. No temperature measurements are taken from mid May through late July due to the background light levels in summer twilight at Chatanika. Lidar retrieval methods have been developed by students at UAF to allow measurements at different resolution to yield robust characterizations and estimates of the

geophysical variability of the Arctic middle atmosphere [e.g., Cutler, 2000; Wang, 2003; Nadakuditi, 2005; Thurairajah, 2009].

2.2. The lidar equation

The lidar signal is composed of a sequence of pulses that is governed by photon counting statistics. The expected returned lidar signal is proportional to the atmospheric density. Under clear sky conditions, the expected total lidar signal from an altitude range ($z-\Delta z/2$, $z+\Delta z/2$) in a time interval Δt is given by the lidar equation,

$$N_{TOT}(z) = N_S(z) + N_B + N_D \tag{2.1}$$

where $N_S(z)$ is the lidar signal count proportional to the atmospheric density, N_B is the background skylight count, and N_D is the detector dark count given by,

$$N_S(z) = \eta T^2 \frac{E_L R_L \Delta t}{hc/\lambda_L} \rho(z) \Delta z \sigma_\pi^R \frac{A_T}{z^2} \tag{2.2}$$

$$N_B = \eta \left[H_N R_L \Delta t \pi \left(\frac{\Delta\Theta_R}{2} \right)^2 A_T \Delta\lambda \right] \left(\frac{2\Delta z}{c} \Big/ \frac{hc}{\lambda} \right) \tag{2.3}$$

$$N_D = (C_N R_L \Delta t) \left(\frac{2\Delta z}{c} \right) \tag{2.4}$$

In the above equations, η is the receiver efficiency, λ_L is the transmission wavelength (m), T is the atmospheric transmission at λ_L, E_L is the laser energy per pulse (J), R_L is the laser repetition rate (s^{-1}), $\rho(z)$ is the number concentration of scatterers at an altitude z (m^{-3}), A_T is the telescope area (m^2), σ_π^R is the effective backscatter cross section at λ_L (5.22×10^{-31} m^2), h is Planck's constant ($\sim6.63\times10^{-34}$ J s), c is the speed of light ($\sim3.0\times10^8$ m s^{-1}), $\Delta\Theta_R$ is the FOV of the receiver (radians), H_N is the background sky irradiance (W m^{-2} μm sr), $\Delta\lambda$ is the bandwidth of the detector (μm), and C_N is the dark count rate for the detector (s^{-1}). Standard atmosphere densities at 20 km, 40 km, 60 km, and 80 km are

8.8×10^{-2}, 3.9×10^{-3}, 2.9×10^{-4}, and 1.6×10^{-5} kg m^{-3} respectively. Pressures at these altitudes are 5.5×10^{1}, 2.8×10^{0}, 2.0×10^{-1}, and 8.9×10^{-3} hPa, respectively [USSA, 1976].

Figure 2.2 shows the total lidar signal profile, $N_{TOT}(z)$, as a function of altitude measured by the NICT Rayleigh lidar system on 2–3 January 2012. The laser pulse energy was 400 mJ. The total lidar signal represents the signal collected from 784,000 laser pulses over an 11.7 h window from 2127–0913 LST (LST = UT – 9 h) on the night of 2–3 January 2012. Between approximately 25 km and 90 km the profile decays with altitude as the density of the atmosphere decreases with altitude. Above ~90 km, the signal is dominated by background skylight, N_B, and detector dark signal, N_D. Below 25 km the lidar signal is reduced due to electronic switching of the lidar receiver detector to avoid the high signal returns from the dense lower atmosphere.

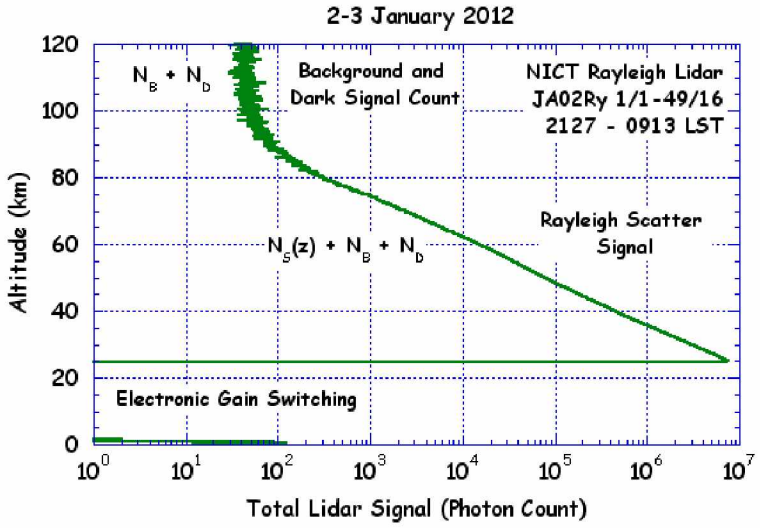

Figure 2.2. Photon count profile plotted as a function of altitude measured by the NICT Rayleigh lidar at PFRR on the night of 2–3 January 2012. The profile was acquired by integrating the signal from 784,000 laser pulses over a period of 11.7 h.

While Figure 2.2 shows the lidar signal integrated over the whole observation period, the raw lidar signals are acquired in the following fashion. As described above, the lidar signal from several (typically 1000) laser pulses is integrated over a short period

(typically 50 s) period in the MCS unit and stored as a single raw data photon count profile. The profile is then transferred to the computer and then displayed on the computer screen. The computer initiates a new profile. This process continues for several profiles (typically 16) called a set. Each set is associated with an individual data file. The data files are named by date and sequentially by set number (e.g., the first set on January 2 is names JA02RY.001). Once a set is completed the data acquisition program pauses for the operator to review the data, make system adjustments (e.g., adjust laser energy, adjust interference filter, pause acquisition due to increasing cloud cover) as required, and begin the next set. Each set takes less than 14 minutes to complete and typically 50 sets are acquired over the course of a 12 h observation period. On 2–3 January 2012 the observation period lasted 11.7 h while the laser operated for 10.9 h, with 0.8 h of time spent on making adjustments to the lidar system during the observation.

Under clear sky conditions, the lidar signals remain relatively constant through the observation and provide uniform measurements of density and temperature through the whole observation period. The operator uses the lidar signal per-laser-pulse as an operational indicator of signal quality. The lidar signal per-laser-pulse is calculated as the lidar signal profile over a certain number of laser pulses divided by the number of laser pulses (e.g., 1000 for a single raw data profile or 16000 for a data set). Under good conditions (i.e. clear skies and maximum laser energy) the lidar signal per-laser-pulse of one photon count per-laser-pulse is expected from the 60–65 km altitude region. Signals lower than this indicates reduced atmospheric transmission due to clouds and/or aerosols, laser pulse energy, or receiver efficiency. Figure 2.3 shows the lidar signal per-laser-pulse calculated for each set on the night of 2–3 January 2012. The average total signal per-laser-pulse from 60–65 km was 0.84 on 2–3 January 2012. While the signals remain constant over the first 45 sets (2126–0816 LST) the signals at all altitudes rise steadily over sets 46 through 49 (0817–0914 LST). The rise is most pronounced in the signal at the higher altitudes (80–85 km, 90–95 km, and 100–105 km) after set 45. This increase in signal begins at an approximate solar angle of -12° [USNO, 2012] and reflects the fact

that the total signal is dominated by the background signal at these higher altitudes. The data also shows the limitations of using the NICT Rayleigh lidar system for daytime observing.

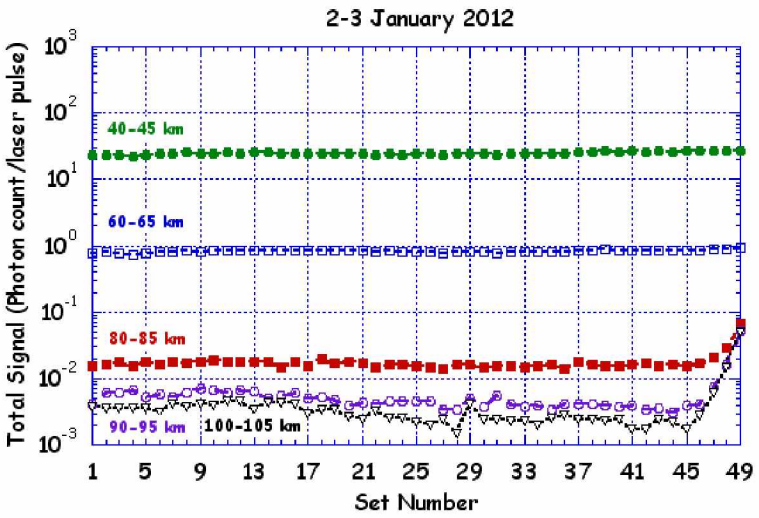

Figure 2.3. Signal levels per-laser-pulse as a function of set number on 2–3 January 2012 (2127–0913 LST).

The combined background skylight and dark signal ($N_B + N_D$) is 44 photon counts on 2–3 January 2012. This signal is evident as the value of the lidar signal that remains constant with altitude above 110 km in Figure 2.2. The specific value is calculated as the average of the lidar signal over 5 km altitude range centered around 225 km. The PMT has typical anode dark counts for the PMT of 50 s^{-1} [Hamamatsu Photonics, 2006]. In a 75 m range bin, this would result in a signal of 2.5×10^{-5} photon counts per-laser-pulse. Thus, the dark current contributes a dark signal of 20 photon counts to the total lidar signal (Figure 2.2) and a signal of 1.7×10^{-3} to the total signal per-laser-pulse (Figure 2.3). During nighttime conditions (corresponding to astronomical darkness with the sun twelve or more degrees below the horizon), the background skylight and dark detector signals have similar contributions to the total lidar signal.

The photon counting process acts as a Poisson random variable [e.g., Papoulis, 1984; Taylor, 1996]. For Poisson random variables, the variance equals the expected value and

there is an inherent standard deviation $N_{TOT}^{-1/2}$ for an expected photon count signal of value N_{TOT}. The relative error in the total signal photon count is given by,

$$\frac{\Delta N_{TOT}}{N_{TOT}} = \frac{\sqrt{N_{TOT}}}{N_{TOT}} = \frac{1}{\sqrt{N_{TOT}}} \tag{2.5}$$

and the signal photon counting error is,

$$\frac{\Delta N_S}{N_S} = \frac{\Delta N_{TOT}}{N_S} = \frac{\sqrt{N_{TOT}}}{N_S} = \frac{\sqrt{N_S + N_B + N_D}}{N_S} \tag{2.6}$$

In an ideal lidar world (i.e. a perfect detector and no skylight) N_B and N_D would be zero and from Equation 2.6 we can see that the relative uncertainty in the photon counting signal decreases to $\Delta N_S/N_S = N_S^{-1/2}$. The lidar relative error profile for 2–3 January 2012, expressed as a percentage, is shown in Figure 2.4. The relative error increases with altitude as the lidar signal reduces in height.

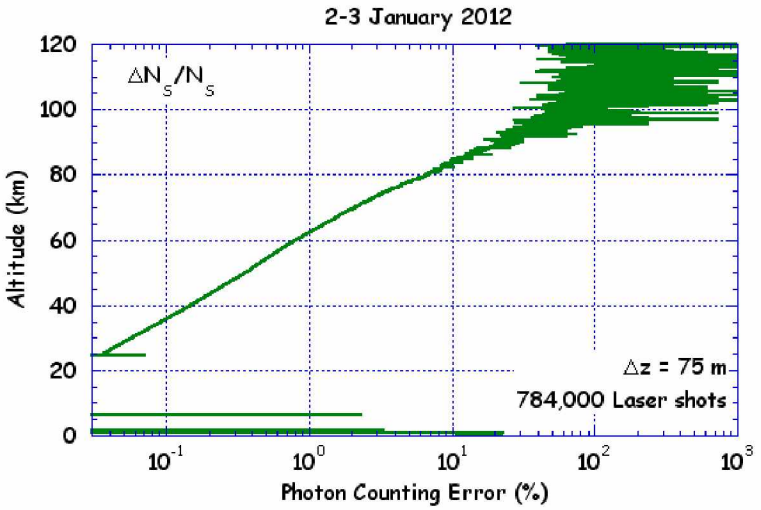

Figure 2.4. Relative photon counting error (%) plotted as a function of altitude from 2–3 January 2012.

The relative errors in the photon count profile in Figure 2.2 are calculated for 13 altitudes in Table 2.2. The signals are averaged over 5 km altitude and thus represent the statistically robust signal in a 75 m range bin at the center of the altitude range. The

relative error increases from less than 0.2% at 40 km to over 100% at 100 km. The error increases more rapidly with height as the total lidar signal is dominated by the combined background skylight and dark detector signals. Above 92.5 km, the combined background and dark signals are larger than the atmospheric density component of the lidar signal and the relative errors are greater than 30%. Similar analyses can be found in Wang [2003] and Nadakuditi [2005] for 20–21 December 2002 and 7–8 March 2002, respectively.

Table 2.2. Lidar signal statistics for 2–3 January 2012 (2127–0913 LST).

Altitude (km)	Total Signal, N_{TOT} [1,2] (Photon count)	Signal, N_S [1,2,3,4] (Photon count)	Relative Error $\Delta N_S/N_S$ (%)
42.5	296658	296614	1.8×10^{-1}
47.5	122868	122824	2.9×10^{-1}
52.5	53004	52960	4.3×10^{-1}
57.5	23775	23731	6.5×10^{-1}
62.5	9899	9855	1.0×10^{0}
67.5	3933	3889	1.6×10^{0}
72.5	1505	1461	2.7×10^{0}
77.5	529	485	4.7×10^{0}
82.5	213	169	8.6×10^{0}
87.5	110	66	1.6×10^{1}
92.5	72	28	3.0×10^{1}
97.5	57	13	5.8×10^{1}
102.5	50	6	1.2×10^{2}

1: Signals are averaged over 5 km altitude and represents signal in 75 m range bins
2: Numbers are rounded to the nearest whole number
3: Background signal, $N_B + N_D = 44$ photon counts
4: 784,000 laser pulses transmitted

From Equation 2.2 we can see that all components of the lidar system are directly proportional to the temporal resolution, Δt, and the spatial resolution, Δz, and can be rewritten in terms of systematic constants defined by Equations 2.10–2.12.

$$N_S(z) = K_S \frac{\rho(z)}{z^2}(\Delta z \Delta t) \tag{2.7}$$

$$N_B = K_B H_N (\Delta z \Delta t) \tag{2.8}$$

$$N_D = K_D (\Delta z \Delta t) \tag{2.9}$$

Where,

$$K_S = \eta T^2 \frac{E_L R_L}{hc/\lambda_L} \sigma_\pi^R A_T \tag{2.10}$$

$$K_B = \eta R_L \pi \left(\frac{\Delta\Theta_R}{2}\right) A_T \Delta\lambda \left(\frac{1}{c} \Big/ \frac{hc}{\lambda}\right) \tag{2.11}$$

$$K_D = C_N R_L \left(\frac{2}{c}\right) \tag{2.12}$$

By integrating the photon count profiles in time and/or space, the product of the spatial and temporal resolution increases by a factor k (i.e., $\Delta t \Delta z \rightarrow k\Delta t \Delta z$). Thus, all the components of the total lidar signal, Equations 2.7–2.9, increase by a factor k (i.e. $N_S \rightarrow kN_S$, $N_D \rightarrow kN_D$, $N_B \rightarrow kN_B$, $N_{TOT} \rightarrow kN_{TOT}$) and the relative error decreases by a factor of $k^{1/2}$.

$$\frac{\Delta N_S}{N_S} \rightarrow \frac{\sqrt{kN_S + kN_B + kN_D}}{kN_S} = \frac{\sqrt{N_S + N_B + N_D}}{\sqrt{k}N_S} = \frac{\Delta N_S}{\sqrt{k}N_S} \tag{2.13}$$

Therefore, the raw photon count profiles can be acquired at high-resolution and then post-processed at lower resolution to increase the signal and decrease the relative error. For example, raw lidar profiles with a resolution of Δt = 50 s and Δz = 75 m can be post-

processed at a resolution of $\Delta t = 30$ min and $\Delta z = 1875$ m, increasing the signal levels by a factor of 900 and decreasing the relative error by a factor of 30. This ability to manipulate the resolution and statistical accuracy of the lidar measurements allows the operator to conduct the observations at high resolution and optimize the performance of the lidar system in real time and then post process the measurements at lower resolution that yields a desired statistical accuracy. As the error depends on the product of the temporal and spatial resolution, so the resolution in time and space can change while maintaining a constant product $\Delta t \Delta z$ with no change in error. For example, to have 1% errors at 62.5 km (Table 2.2) requires measurements at a resolution of 75 m and 39,200 s (= 784,000 laser pulses/20 pps, 653 min) or 2.94×10^6 m s. Measurements at a resolution of 1 km and 2,940 s (49 min) or a resolution of 2 km and 1,470 s (24.5 min) would also have 1% errors.

The quality of the lidar signal can also be described by the signal-to-noise ratio (SNR), which is just the square of the inverse of the relative error,

$$SNR = \frac{N_S(z)^2}{\Delta N_S(z)^2} \tag{2.14}$$

On 2–3 January 2012 the SNR is 3.0×10^5 at 42.5 km and decreases to 9.8×10^3 at 62.5 km, 1.2×10^2 at 82.5 km, 1.1×10^1 at 92.5 km, and 7.1×10^{-1} at 102.5 km.

While decreasing the measurement resolution improves the quality of the lidar signal through increases in all components of the total signal, there are ways to more dramatically increase the signal quality. For example, by increasing the atmospheric signal, N_S, while not increasing the background skylight signal, N_B, and dark detector counts, N_D. Increases in the laser pulse energy, E_L, increase K_S while leaving K_B and K_D unaltered. Increasing the repetition rate, R_L, of the laser increases all three signals just as it does in the case of changes in measurement resolution. Increases in the telescope area, A_T, the receiver efficiency, η, and the atmospheric transmission, T, increase K_S and K_B while leaving K_D unaltered. If the dark detector signal is negligible compared to the

background skylight signal, then changes in each of these three quantities (A_T, η, T) will have the same effect as changes in the measurement resolution.

2.3. Lidar density and temperature retrievals

The raw photon counts profiles are binned and then used to calculate the density profiles using Equation 2.2 and lidar standard inversion techniques [Leblanc et al., 1998; Wang, 2003]. The densities are smoothed by 2 km (i.e. 27 range bins) and normalized at the lowest altitude, typically 40 km, to yield a relative density profile,

$$\frac{\rho(z_1)}{\rho(z_2)} = \frac{N_S(z_1)}{N_S(z_2)}\left(\frac{z_1}{z_2}\right)^2 \tag{2.15}$$

The normalized relative density profile (RD) is a robust measurement that is independent of system parameters and sky conditions; a very powerful aspect of the lidar method that highlights the fact that the lidar technique does not require absolute knowledge of the system parameters, such as the transmitted power or atmospheric transmission. The normalized density profile for 2–3 January 2012 is shown in Figure 2.5.

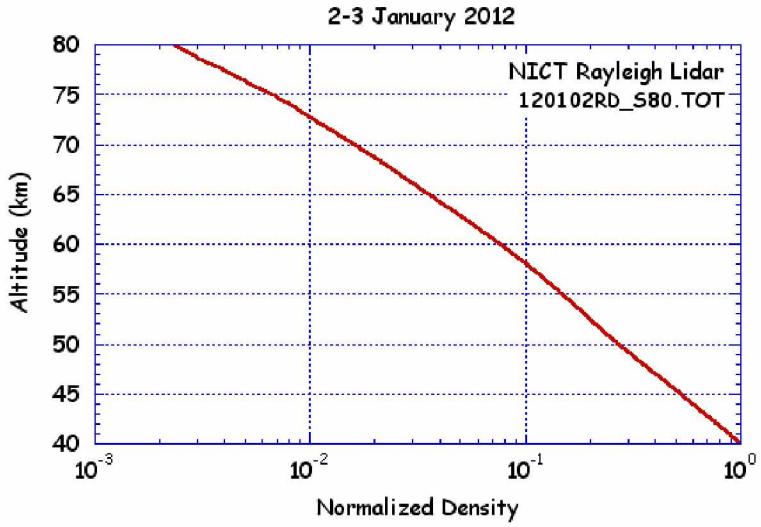

Figure 2.5. Density profile plotted as a function of altitude retrieved from the total photon count profile measured on 2–3 January 2012 by the NICT Rayleigh lidar and normalized to one at 40 km.

The determination of the temperature profile from the normalized relative density profile assumes that both the hydrostatic approximation (Equation 2.16) and ideal gas law (Equation 2.17) are viable in the middle atmosphere. Departures from hydrostatic balance are only necessary to consider during intense small-scale systems (e.g., tornadoes or squall lines that occur in the troposphere) [Holton, 2004]. This method assumes that the air is essentially dry and very small amounts of water vapor are present in the stratosphere and mesosphere. However, this assumption may be invalid in the presence of aerosols, polar stratospheric clouds, or noctilucent clouds [e.g., Stevens et al., 2003; 2005; Kelley et al., 2010].

$$\frac{\partial p}{\partial z} = -\rho(z)g(z) \tag{2.16}$$

$$p = \frac{\rho RT}{M} \tag{2.17}$$

Where g is the acceleration of gravity (9.8228 m s^{-2} at LRL [Thurairajah, 2009]), p is the atmospheric pressure, ρ is the atmospheric density (mol m^{-3}), R is the ideal gas constant

(8.3145 J K^{-1} mol^{-1}), T is the temperature (K), and M is the mean molecular weight of air, where dry air is assumed to be a uniform mixture of O_2, N_2, CO_2, etc. (2.8964×10^{-2} kg mol^{-1}). Under the assumption that the atmosphere is in hydrostatic equilibrium (Equation 2.16), the atmosphere is homogeneous and behaves as a uniform gas. Using the ideal gas law (Equations 2.17) as the equation of state, atmospheric pressure is determined by,

$$p(z) = -\int_{z_0}^{z} \rho(r)g(r)dr + \frac{R}{M}\rho(z_0)T(z_0) = \frac{R}{M}\rho(z)T(z) \tag{2.18}$$

Rearranging Equation 2.18 for temperature, T, results in a function whose first term is dependent on an initial temperature, $T(z_0)$, and second term can be determined from the normalized relative density profile (Equation 2.15),

$$T(z) = \frac{\rho(z_0)}{\rho(z)}T(z_0) - \frac{M}{R}\int_{z_0}^{z} \frac{\rho(r)}{\rho(z)}g(r)dr \tag{2.19}$$

Temperature is initiated at 80 km using the Stratospheric Processes And their Role in Climate (SPARC) climatology [SPARC, 2002; Randel et al., 2004]. Temperature is integrated downward from an initial altitude to avoid the error in the initial temperature growing substantially as z increases (Equation 2.20). The top altitude was chosen at 80 km during the International Polar Year (IPY) [Collins, 2004; ICSU, 2004; NRC, 2004] as a conservative approach [e.g., Thurairajah et al., 2009] but has been extended upwards to 90 km for specific experiments [e.g., Collins et al., 2011].

$$T(z) = T(z_0)\frac{N(z_0)}{N(z)}\left(\frac{z_0}{z}\right)^2 + \frac{M}{R}\int_{z}^{z_0} \frac{N(r)}{N(z)}\left(\frac{r}{z}\right)^2 g(r)dr \tag{2.20}$$

Due to the data acquisition method, the lidar profile is a series of discrete values per range bin. The downward integration method becomes a summation of the 75 m range bins,

$$T_i = T_1 \frac{N_1 z_1^2}{z_i^2 N_i} + \frac{M}{R} \Delta z \sum_{j=2}^{i} \frac{N_j g_j z_j^2}{N_i z_i^2} \tag{2.21}$$

The lowest altitude of the temperature retrieval is chosen at 40 km to ensure no contamination from aerosols and the count rate does not exceed the maximum determined by the system detector. The temperature profile for 2–3 January 2012 is shown in Figure 2.6, representing the integrated signal from 784,000 laser pulses. There are two sources of uncertainty in the temperature calculation; the statistical uncertainty in the raw photon count signal (which decreases as the resolution parameters are increase), and the uncertainty due to the initial temperature estimate at 80 km, taken as 25 K. The initial temperature from SPARC contributes 100%, 21%, 4%, and 1% of the total error at 80 km, 70 km, 60 km, and 50 km, respectively [Thurairajah et al., 2009].

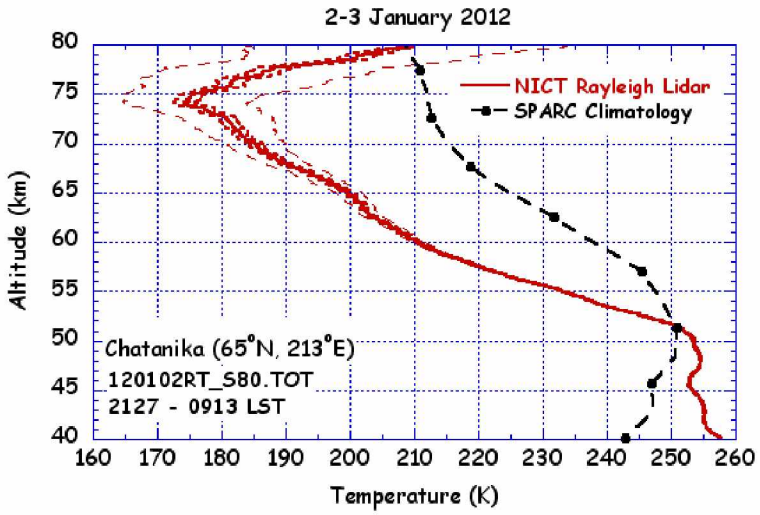

Figure 2.6. The temperature profile plotted as a function of height, measured by the NICT Rayleigh lidar on 2–3 January 2012 (2127–0913 LST). Also plotted is the photon counting error profile (thick red dotted line), the error due to the initial temperature at 80 km from SPARC (thin red dashed line), assumed to be 25 K at 80 km, and the January climatological temperature profile from SPARC (think black dashed line with filled circles).

In Figure 2.6, the SPARC reference atlas shows a stratopause at approximately 51 km with a temperature of 251 K. Above the stratopause, SPARC temperatures decay with height, as expected from radiative balance. The NICT Rayleigh lidar temperature has no clear stratopause and departs from the climatological temperature by as much as 38 K where the lidar temperature reaches a minimum of 174 K at 74 km. At 74 km, the error in the total temperature profile due to the uncertainty in the initial temperature and photon counting statistical uncertainty is 10 K and 2 K, respectively. The departure from climatological temperatures, seen on 2–3 January 2012 in Figure 2.6, is a common occurrence in temperatures measured by the NICT Rayleigh lidar during the winter months (~October – February) due to high gravity and planetary wave activity. The average temperature, $\overline{T}$, density, $\overline{\rho}$, temperature error due to the initial temperature, $\Delta\overline{T}$, temperature error due to photon counting statistics, $\Delta\overline{T}_1$, density error, $\Delta\overline{\rho}$, and their absolute magnitudes are given in Table 2.3 for the average temperature profile and Table 2.4 for the 2 hour period centered on 0100 LST. The relative errors $\Delta\overline{T}_1/\overline{T}$ and $\Delta\overline{\rho}/\overline{\rho}$ increase by a factor of 2.33 from the 10.9 h to 2 h observation.

Table 2.3. Temperature and density statistics for 2–3 January 2012 (2127–0913 LST).

Alt (km)[1]	$\overline{T}$	$\overline{\rho}$	$\Delta\overline{T}$	$\Delta\overline{T}_1$	$\Delta\overline{\rho}$	$\Delta\overline{T}/\overline{T}$	$\Delta\overline{T}_1/\overline{T}$	$\Delta\overline{\rho}/\overline{\rho}$
42.5	255.3	7.42×10^{-1}	1.48×10^{-1}	1.13×10^{-1}	3.43×10^{-4}	5.79×10^{-4}	4.44×10^{-4}	4.63×10^{-4}
47.5	253.8	3.85×10^{-1}	2.56×10^{-1}	1.76×10^{-1}	2.44×10^{-4}	1.01×10^{-3}	6.92×10^{-4}	6.34×10^{-4}
52.5	245.0	2.04×10^{-1}	4.35×10^{-1}	2.56×10^{-1}	1.84×10^{-4}	1.78×10^{-3}	1.04×10^{-3}	9.02×10^{-4}
57.5	220.8	1.10×10^{-1}	7.60×10^{-1}	3.53×10^{-1}	1.44×10^{-4}	3.44×10^{-3}	1.60×10^{-3}	1.31×10^{-3}
62.5	204.6	5.39×10^{-2}	1.51×10^{0}	5.27×10^{-1}	1.08×10^{-4}	7.37×10^{-3}	2.58×10^{-3}	2.00×10^{-3}
67.5	192.0	2.48×10^{-2}	3.24×10^{0}	8.29×10^{-1}	7.87×10^{-5}	1.69×10^{-2}	4.32×10^{-3}	3.17×10^{-3}
72.5	179.7	1.08×10^{-2}	7.62×10^{0}	1.41×10^{0}	5.60×10^{-5}	4.24×10^{-2}	7.86×10^{-3}	5.21×10^{-3}
77.5	191.0	4.09×10^{-3}	1.71×10^{1}	2.28×10^{0}	3.79×10^{-5}	8.96×10^{-2}	1.19×10^{-2}	9.26×10^{-3}

1: Center altitude of the 5 km average.

Table 2.4. Temperature and density statistics for 2–3 January 2012 (2353–0202 LST).

Alt (km)[1]	$\overline{T}$	$\overline{\rho}$	$\Delta\overline{T}$	$\Delta\overline{T}_1$	$\Delta\overline{\rho}$	$\Delta\overline{T}/\overline{T}$	$\Delta\overline{T}_1/\overline{T}$	$\Delta\overline{\rho}/\overline{\rho}$
42.5	257.9	7.26×10^{-1}	2.83×10^{-1}	2.68×10^{-1}	7.82×10^{-4}	1.10×10^{-3}	1.04×10^{-3}	1.08×10^{-3}
47.5	255.3	3.80×10^{-1}	4.47×10^{-1}	4.10×10^{-1}	5.60×10^{-4}	1.75×10^{-3}	1.61×10^{-3}	1.47×10^{-3}
52.5	244.6	2.03×10^{-1}	6.79×10^{-1}	5.91×10^{-1}	4.24×10^{-4}	2.77×10^{-3}	2.42×10^{-3}	2.09×10^{-3}
57.5	221.6	1.09×10^{-1}	1.04×10^{0}	8.23×10^{-1}	3.30×10^{-4}	4.71×10^{-3}	3.71×10^{-3}	3.03×10^{-3}
62.5	205.0	5.37×10^{-2}	1.80×10^{0}	1.22×10^{0}	2.49×10^{-4}	8.80×10^{-3}	5.93×10^{-3}	4.63×10^{-3}
67.5	189.1	2.50×10^{-2}	3.52×10^{0}	1.89×10^{0}	1.83×10^{-4}	1.86×10^{-2}	1.00×10^{-2}	7.29×10^{-3}
72.5	176.6	1.07×10^{-2}	7.74×10^{0}	3.18×10^{0}	1.29×10^{-4}	4.38×10^{-2}	1.80×10^{-2}	1.20×10^{-2}
77.5	185.9	4.04×10^{-3}	1.74×10^{1}	5.21×10^{0}	8.64×10^{-5}	9.34×10^{-2}	2.80×10^{-2}	2.14×10^{-2}

1: Center altitude of the 5 km average.

2.4. Expectations of the upgraded lidar system

During spring 2012, the Rayleigh lidar system was upgraded to allow measurements of higher accuracy to higher altitudes. This was accomplished in two stages: first, with the replacement of the 62 cm Newtonian telescope with a 104 cm Cassegrain telescope, and second, with the replacement of the Nd:YAG laser operating at 20 pps with a Nd:YAG laser operating at 30 pps with higher energy pulses. As discussed earlier, the accuracy of the lidar measurement is determined by photon counting statistics, i.e. raw lidar signal. Since the upgraded system will yield increased raw lidar signals, the accuracy of the lidar measurements are expected to improve. The increase in laser power allows the upper altitude limit to be extended. The upper altitude had been conservatively set to 80 km prior to, and during, the IPY [Thurairajah et al., 2009; 2010a; 2010b]. Chapter 3 presents the actual performance of the improved lidar system based on field trials. In this section, the changes in the lidar system performance for a temporal resolution of a 2 h and a spatial resolution of 75 m are analyzed, based on an increase,

i. by a factor of ~3.0 in the area of the telescope (A_T),

ii. by a factor 1.9 in the laser pulse energy (E_L),

iii. by a factor of 1.5 in the laser pulse repetition rate (R_L).

For the 20 pps laser system, an integration time of 2 h leads to a total of 144,000 laser pulses. The night of 2–3 January 2012 represents the signal from 784,000 laser pulses, a factor of ~5.4 in laser pulses compared to the 2 h duration. The total signals observed on 2–3 January 2012 are divided by 5.4 and are assumed to approximate the signal levels observed under similar sky conditions over a 2 h period, with total signal per-laser-pulse levels staying the same (i.e. signal levels in Figure 2.3 unchanged). Due to the simple scaling technique applied, the expected errors scale as one over the square root of the ratio of total laser pulses by the hypothetical laser pulses (i.e., $0.43 = 5.4^{-1/2}$). The lidar signal statistics for the integrated signal from 144,000 laser pulses on 2–3 January 2012 are presented in Table 2.5 for the period of 2352–0202 LST (JA02RY 11/1–19/16). The SNR at 42.5 km, 62.5 km, 82.5 km, 92.5 km and 102.5 km are 5.4×10^{4}, 1.8×10^{3}, 2.6×10^{1}, 2.6×10^{0} and 3.2×10^{-1}, respectively. The decrease relative to the nightly average is due to the decrease in temporal resolution.

Table 2.5. Lidar signal statistics for 2–3 January 2012 (2353–0202 LST).

Altitude (km)	Total Signal, N_{TOT} [1,2] (Photon count)	Signal, N_S [1,2,3] (Photon count)	Relative Error $\Delta N_S/N_S$ (%)
42.5	54353	54346	4.3×10^{-1}
62.5	1846	1839	2.3×10^{0}
77.5	96	89	1.1×10^{1}
82.5	38	31	2.0×10^{1}
92.5	12	5	6.9×10^{1}
102.5	8	1	2.8×10^{2}

1: Signals are averaged over 5 km altitude and represents signal in 75 m range bins
2: Numbers are rounded to the nearest whole number
3: Background signal, $N_B + N_D = 6.8$ photon counts

If the area of the telescope, A_T, increased by a factor of ~3.0, both $N_S(z)$ and N_B would increase but not N_D, seen by Equations 2.7–2.12. Therefore, both the total photon counts and signal photon counts are scaled by 3.0 to represent the increase from a 62 cm

diameter telescope to a 104 cm diameter telescope, shown at selected altitudes in Table 2.6. The background signal is not dependent on laser energy, so the total photon count signals from Table 2.5 are scaled by 1.9 while the background counts remain unchanged, Table 2.6. From the lidar equation (Equations 2.7–2.12) it is clear that all components will be affected by an increase in laser repetition rate. Therefore, the total photon count and signal photon counts are scaled by 1.5, Table 2.6. Table 2.7 is the expected signal from 144,000 laser pulses if the laser repetition rate increased from 20 pps to 30 pps. The number of laser pulses (144,000) was chosen because that is the standard number of laser pulses acquired over a 2 h window with the current 20 pps laser. The expected integrated signal from 144,000 laser pulses with the larger telescope, higher power, higher repetition rate laser are given in Table 2.7.

Table 2.6. Expected lidar signal statistics for 2 h measurements with individual system upgrades[1,3].

Altitude (km)[1]	Signal, N_S[2] (Photon count)			Relative Error $\Delta N_S/N_S$ (%)		
	3.0 A_T	1.9 E_L	1.5 R_L[3]	3.0 A_T	1.9 E_L	1.5 R_L
42.5	163038	103257	81519	7.4×10^{-1}	5.9×10^{-1}	5.3×10^{-1}
62.5	5517	3494	2759	4.0×10^{0}	3.2×10^{0}	2.9×10^{0}
77.5	267	169	134	1.9×10^{1}	1.5×10^{1}	1.3×10^{1}
82.5	93	59	47	3.3×10^{1}	2.6×10^{1}	2.4×10^{1}
92.5	15	10	8	1.1×10^{2}	8.1×10^{1}	8.4×10^{1}
102.5	3	2	2	4.1×10^{2}	2.9×10^{2}	3.4×10^{2}

1: Based on lidar observations on 2–3 January 2012

2: Background signal, $N_B + N_D = 14.2$, 6.8, and 10.3 photon counts

3: Signal now based on 216,000 laser pulses at 30 pps in 2 h

Table 2.7. Expected lidar signal statistics for 2 h measurement[2] with all upgraded system parameters.

Altitude (km)	Total Signal, N_{TOT} (Photon count)	Signal, N_S[1] (Photon count)	Relative Error $\Delta N_S/N_S$ (%)
42.5	464680	464658	1.5×10^{-1}
62.5	15745	15723	8.0×10^{-1}
77.5	782	761	3.7×10^{0}
82.5	286	265	6.4×10^{0}
92.5	64	43	1.9×10^{1}
102.5	30	9	6.4×10^{1}

1: Background signal, $N_B + N_D = 21.4$ photon counts
2: JA02RY 11/1–19/16

In Table 2.7, the SNR decreases from 4.6×10^{5} at 42.5 km to 2.4×10^{0} at 102.5 km. The relative errors in the 2 h measurement (Table 2.5) are representative of January signals at Chatanika. The relative errors at 77.5 km of 11% and 82.5 km of 20% are important because temperatures are typically initiated at 80 km. The signals expected with the new system (Table 2.7) have relative errors of 3.7% at 77.5 km and 6.4% at 82.5 km. Therefore, the new system will permit the extension of top altitudes used for temperature retrievals. The relative error reaches 64% at 102.5 km (Table 2.7) and gives a best case scenario for the extended top altitude.

2.5. Summary

In this Chapter, I have used the lidar equation to review the performance of the original NICT Rayleigh lidar and determined the accuracy of the lidar measurements as a function of measurement resolution and system parameters. I have shown how changes in resolution and system parameters can change the accuracy of the lidar measurements. An initial estimate of the expected signals of the extended lidar system was performed by directly scaling the signals to account for the upgraded system parameters. In Chapter 3, I describe the extended Rayleigh lidar system and present field tests with the upgraded system taken in spring 2012.

Chapter 3. Performance of the Extended Rayleigh Lidar System

3.1. Introduction

In Chapter 2, I reviewed the operation and performance of the NICT Rayleigh lidar system and predicted the improvement in performance based on two upgrades to the system. The upgrades were increasing the area of the receiver telescope and increasing the power of the Nd:YAG laser. In this Chapter, I implement these upgrades to the lidar system and evaluate the performance based on a series of field trials that I conducted in spring 2012. These field tests are important as they allow me to characterize two aspects of the lidar system that did not appear in the Chapter 2 analysis. The first is consideration of nonlinearities in the photon counting receiver and the second is differences in the efficiency of the receiver telescopes. The analysis in Chapter 2 assumed that the lidar signal increases linearly with increase in the area of the receiver telescope and increases in the laser power (given by the product of the laser pulse energy and the pulse repetition rate). In this Chapter, the assumption of linear signal increase is disproven as the Photo-Multiplier Tube (PMT) produces pulses of finite width (~5ns) and the MultiChannel Scalar (MCS) has a maximum counting rate (150 MHz). Thus, if photons arrive within 5 ns of each other they will not be converted to separate electronic pulses by the PMT, furthermore if an electronic pulse arrives at the input of the MCS within 6.67 ns of the preceding pulse it will not be counted. Thus, at large signals the measured lidar signal can be increasingly lower than the true lidar signal as the signal increases. Therefore, as the lidar signal increases with the use of larger telescopes and higher power lasers, we need to ensure that these nonlinearities in the lidar system response are understood. This phenomenon is called pulse pileup [Evans, 1955; Donavan et al., 1993]. The analysis in Chapter 2 also assumed that the efficiency of the receiver system remained constant as the area of the telescope increased. In reality, two different receivers with two different telescopes and detector systems were used so it is necessary to characterize the actual improvement in the performance of the lidar system.

3.2. Extending the Rayleigh lidar system

The NICT lidar system includes a Newtonian telescope with an annular primary mirror with an outer diameter of 620 mm and an inner diameter of 200 mm. The area of the Newtonian primary mirror is 0.270 m^2. The new telescope is a Cassegrain telescope that was donated to the University of Alaska Fairbanks by the University of Illinois at Urbana Champaign. This Cassegrain telescope was aligned and commissioned in 2007–2008 [Light, 2009] and supported resonance lidar measurements at PFRR in 2009 [Collins et al., 2011]. The Cassegrain telescope has an annular primary mirror with an outer diameter of 1040 mm and an inner diameter of 260 mm. The area of the Cassegrain primary mirror is 0.805 m^2. The ratio of the Cassegrain area to the Newtonian area is ~3.0. The Newtonian and Cassegrain telescopes are referred to as the 24-inch and 41-inch telescopes, respectively.

The NICT lidar system includes an Nd:YAG laser (Continuum Powerlite 8020, PL8020) that produces laser pulses of wavelength 532 nm and energy ~400 mJ at a repetition rate of 20 pps. Another Nd:YAG laser (Continuum Powerlite 9030, PL9030) had been deployed at LRL in 2005 as part of a Doppler wind lidar system [Murayama et al., 2007]. This laser had been operated during testing and acquisition of initial wind lidar measurements in 2005 and 2006. The laser failed in 2011, due to a failure in the laser cooling system. After working on and troubleshooting the laser in spring and fall 2011, funds became available in 2012 to repair the laser. In March 2012, an engineer from Continuum (Cliff Holt) spent two days repairing the laser and oversaw the operation of the laser as a lidar transmitter on the night of 28–29 March 2012.

The system specifications are given in Table 3.1 for the extended Rayleigh lidar system and a schematic of the extended lidar system is shown in Figure 3.1. The extended receiver system was triggered from the original NCIT lidar system to ensure precise timing during these initial field tests. The Nd:YAG laser Q-switch triggered the blanking control (BC) which then sent a gate pulse to both PMTs. Similarly, the laser pulse

detector (LPD) triggered the high speed counters (MCSs) to begin counting the incoming PMT pulses.

Table 3.1. Extended Rayleigh lidar system specifications.

Transmitter	
Laser	Nd:YAG
Model	Continuum Powerlite 9030
Wavelength (λ_L)	532 nm
Repetition Rate (R_L)	30 Hz
Pulse Energy (E_L)	733 – 800 mJ
Pulse Width	7 ns
Line Width	1.0 cm^{-1} (28 pm, 30 GHz)
Beam Expander	× 10
Divergence	0.50 mrad
Receiver	
Telescope	Cassegrain
Outer Diameter	1040 mm
Inner Diameter	260 mm
Collecting Area	0.805 m^2
Range Resolution	75 m
Optical Bandwidth	1 nm
Field of view (FOV)	1 – 2 mrad
Detector	Photomultiplier Tube
Model	Hamamatsu R3234–01
Pulse duration	5 ns
Dark Count	50 – 150 counts/second
Preamplifier Gain	× 20
Model	EG&G Ortec VT120C
Bandwidth	10 to 350 MHz
Digital Recorder	Multichannel Scalar
Model	Ortec Turbo MCS T914
Maximum Count Rate	150 MHz

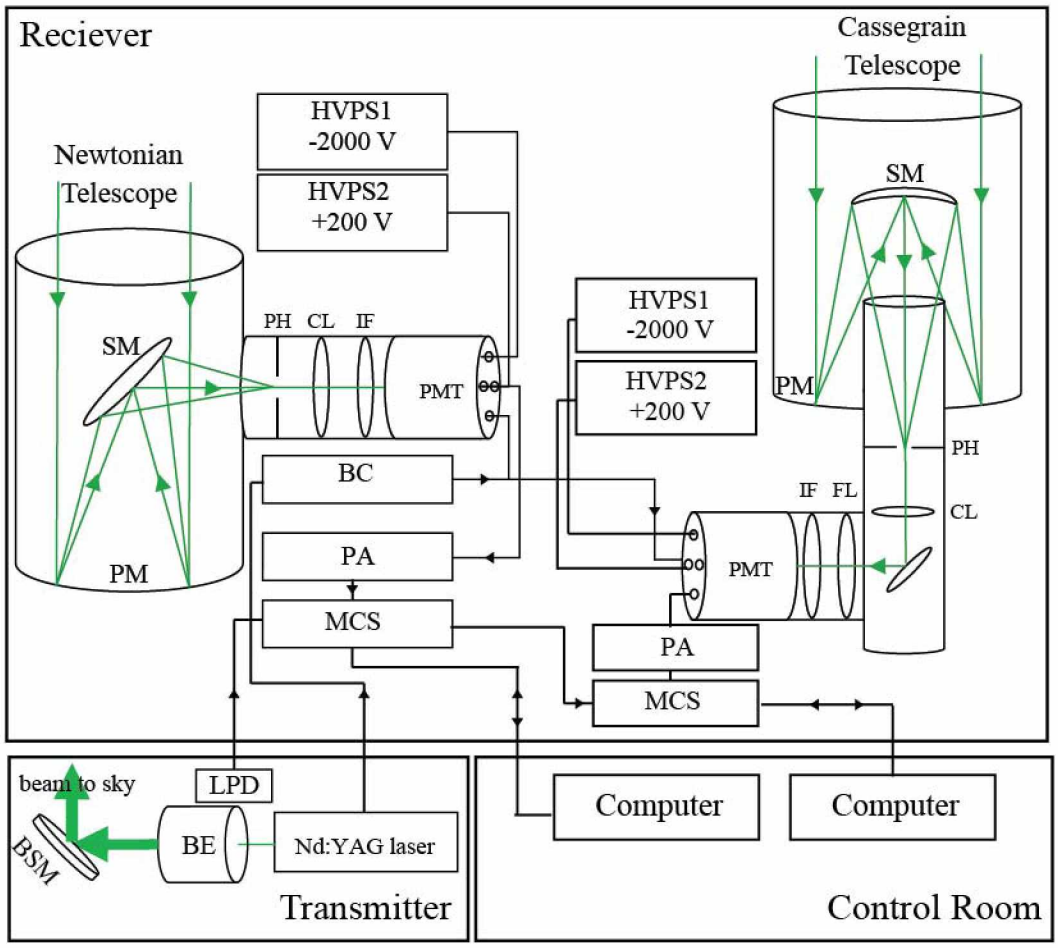

Figure 3.1. Schematic diagram of the Extended Rayleigh lidar system at PFRR, Chatanika, Alaska (65°N, 213°E).

BC – Blanking Control
BE – Beam Expander
BSM – Beam Steering Mirror
CL – Collimating Lens
FL – Focal Lens
HVPS – High Voltage Power Supply
IF – Interference Filter
LPD – Laser Pulse Detector
MCS – MultiChannel Scalar
PA – Pre-Amplifier
PH – Pin Hole
PM – Primary Mirror
PMT – Photo Multiplier Tube
SM – Secondary Mirror

The spring 2012 field tests were conducted while ongoing lidar observations were carried out at PFRR. The NICT Rayleigh lidar has operated, as described in Chapter 2, since its deployment at PFRR in 1997. The system has not been changed in order to guarantee consistency in the observations over several years, in particular during the IPY (2007-2009) and new studies initiated in 2010 [e.g., Nielsen et al., 2012]. These observational programs require observations on a weekly basis and I was able to conduct tests of the new telescope and laser without compromising ongoing studies. Each week I worked with the rest of the lidar team to prioritize the acquisition of ongoing observational data before conducting tests of the new telescope and laser. In this Chapter, I present results from several of these field trails as follows. I first present tests of the relative performance of lidar system using the 24-inch Newtonian and 41-inch Cassegrain telescopes and the PL8020 laser, termed telescope trials. These telescope tests were conducted on the nights of 18–19 February 2012, 22–23 March 2012, 23–24 April 2012, and 24–25 April 2012. I then present tests of the relative performance of the PL9030 and PL8020 lasers using both the 24-inch Newtonian and 41-inch Cassegrain telescopes, termed laser trials. These laser tests were conducted on the nights of 28–29 March 2012 and 3–4 April 2012. I characterize the effects of pulse pileup on the lidar signal at the lower altitudes (< 50 km) and the linear increase in lidar signal at upper altitudes (> 50 km). Before presenting the field trails, I review the phenomenon of pulse pileup in photon counting receivers.

3.3. Pulse Pileup

As discussed in Chapter 2, the lidar photon counting signals have Poisson statistics and behave as Poisson random variables. Poisson's Theorem gives the probability distribution P of measuring k counts in a time interval τ_d [e.g., Papoulis, 1984; Taylor, 1996] as,

$$P\{k\ in\ \tau_d\} = e^{-x}\frac{x^k}{k!} \tag{3.1}$$

where C is the expected or mean number of counts per unit time and $x = C\,\tau_d$ and P must satisfy,

$$\sum_{i=0}^{i=\infty} P\{i\} = 1 \tag{3.2}$$

Pulse overlap occurs if the pulses have a finite nonzero width, in the case of PMTs ~5 ns [Hamamatsu Photonics, 2005; 2006]. If a pulse arrives and a subsequent pulse arrives within 5 ns then the two pulses will overlap and appear as a single pulse. Thus the two pulses have "piled up" like traffic on the highway. When pulse pileup does not occur we have a linear relationship between the input and output signals from the receiver, when pulse overlap or pileup does occur we have a nonlinear relationship. As signal levels increase, the pulses pileup more often and the nonlinear effects increase. The probability of no pulse pileup is the probability that only one or zero pulses arrive in the time interval (i.e. the probability of a linear response) and is denoted P_{linear}.

$$P_{linear} = P(0 \cup 1) = e^{-x}(1 + x) \tag{3.3}$$

Of particular interest is the case where x = 1 which corresponds to the maximum count rate. At the maximum count rate, uniform pulses arrive every 5 ns with an instantaneous gap between them. When x=1, the probability of no pulse pileup, or linear behavior, is 74%. A designer can limit the maximum expected count rate or signal by specifying the acceptable value for the probability of no pulse pileup or alternatively the probability of pulse pileup, $P_{nonlinear}$ (= 1 – P_{linear}). For example, the values of x = 1, 1×10^{-1}, 1×10^{-2}, 1×10^{-3}, and 1×10^{-4} correspond to probabilities of pulse pileup of 26%, 0.47%, 5.0×10^{-3}%, 5.0×10^{-5}%, and 5.0×10^{-7}%, respectively. The conditions for pulse pileup may also be defined by the MCS unit. The maximum count rate of the MCS is 150 MHz and thus a pulse arriving less than 6.67 ns after a count has begun will not be counted. The detector dead time τ_d can be thought of as the finite response time or resolving time of the PMT (5 ns) and the MCS (6.67 ns) and both instruments can be analyzed in the same way.

The signal can be calculated as a function of the true or expected signal based on the type of system. There are two types of systems, paralyzable and non-paralyzable [Evans, 1955]. A paralyzable system is so named because it is unable to count an event (i.e. the arrival of a photon) unless τ_d has elapsed since the last event was counted. If the arrival of a photon is counted at T_i and a second photon arrives at T_{i+1}, the second photon will not be counted unless $T_{i+1} \geq T_i + \tau_d$. Furthermore, τ_d is extended by an additional time τ_d for every event that occurs before the full recovery time τ_d (i.e. τ_d restarts at T_{i+1} if it arrives before the previous τ_d). If the intervals between successive events become consistently shorter than τ_d, the detector will not be able to recover and is therefore considered "paralyzed". Non-paralyzable systems are not affected by the arrival of events during τ_d. They are simply unable to count events during the interval τ_d after an initial event is counted. For a non-paralyzable system, the detector immediately recovers after $T_i + \tau_d$ and is therefore not paralyzed if the intervals between events become increasingly shorter than τ_d. A simplified schematic illustration of pulse pileup in both paralyzable and non-paralyzable systems is shown in Figure 3.2. In Figure 3.2, incoming pulses are represented as instantaneous or infinitely narrow pulses when, in reality, lasers have finite pulse width.

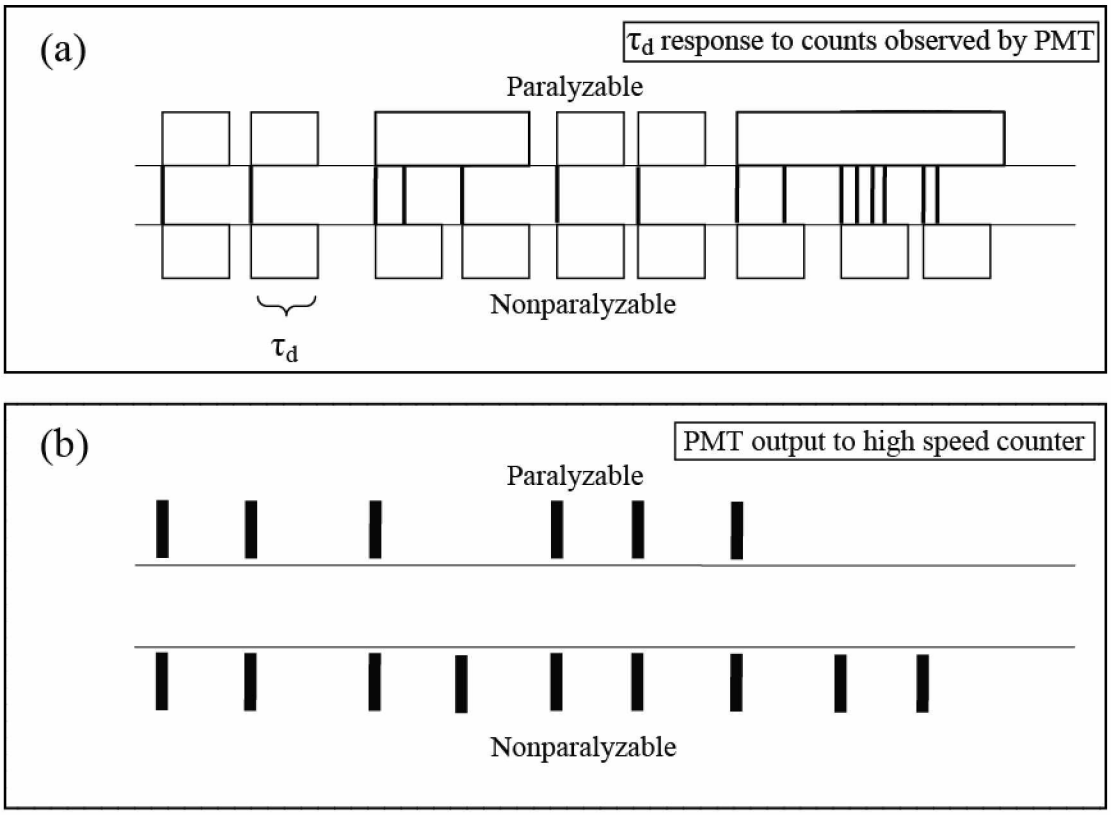

Figure 3.2. Schematic illustration of pulse pileup behavior in paralyzable and non-paralyzable PMTs (adapted from Evans [1955]).

In a paralyzable system only pulses that are followed by intervals longer than τ_d are counted. From Poisson's distribution, the fraction of intervals longer than τ_d is given by e^{-x}, where $x = C_{TRUE}\tau_d$ and C_{TRUE} is the expected or true counting rate. Following the approach of Evans [1955], the observed counting rate for a paralyzable system C_{OBS} is given as,

$$C_{OBS} = C_{TRUE}e^{-x} \tag{3.4}$$

For a value of x = 1 the observed count rate is 37% of the true count rate. For a non-paralyzable system, the detector is unresponsive to incoming pulses for a time interval τ_d after a pulse arrives. If a pulse arrives during that interval τ_d the pulse is ignored but the

interval is not extended. Thus a pulse arriving τ_d after an initial pulse is detected regardless of whether any pulses arrive in the intervening τ_d. Thus, the non-paralyzable detector cannot be paralyzed by succeeding pulses. The observed counting rate for a non-paralyzable system, C_{OBS} is given as,

$$C_{OBS} = \frac{C_{TRUE}}{1 + x} \tag{3.5}$$

For a value of x = 1 the observed count rate is 50% of the true count rate, 35% greater than for the paralyzable system. At low count rates ($x = C_{TRUE}\tau_d << 1$) the behavior of non-paralyzable and paralyzable systems converge. The behavior is shown in Figure 3.3 where we consider a detector with a detection time of 1 s. The 100% linear detector is the (ideal) one where the observed count rate equals the true count rate, and the 50% linear detector is one where the observed count rate is 50% off the true count rate. The non-paralyzable and paralyzable systems depart further and further from the ideal detector, reaching 50% of the true count rate at values of C_{TRUE} equal to 1 s^{-1} and 0.69 s^{-1}, respectively. The paralyzable system has a maximum count rate at a value of C_{TRUE} equal to 1 s^{-1}. This result can be confirmed by direct differentiation of C_{OBS} by C_{TRUE}, and finding that the maximum corresponds to when the true count rate is the reciprocal of the detector time (i.e., $x = C_{TRUE}\tau_d = 1$). As true count rate increases, the observed count rate of the paralyzable system approaches zero and the observed count rate of the non-paralyzable system asymptotically approaches τ_d^{-1}.

In Figure 3.4, the characteristic of pulse pileup are summarized by plotting the probabilities of pulse pileup, P_{linear}, and the fraction of observed to true count rates C_{OBS}/C_{TRUE} for paralyzable and non-paralyzable systems. As x increases, the probability of pulse pileup increases and the ratio of the observed counts to the true counts decrease. At x = 0.1, 1, and 10, the probability of pulse pileup is 0.5%, 26%, and 100%, respectively. The corresponding ratios of observed to true counts for the paralyzable

system are 91%, 37%, and 0.005%. The corresponding ratios of observed to true counts for the non-paralyzable system are 91%, 50%, and 9%.

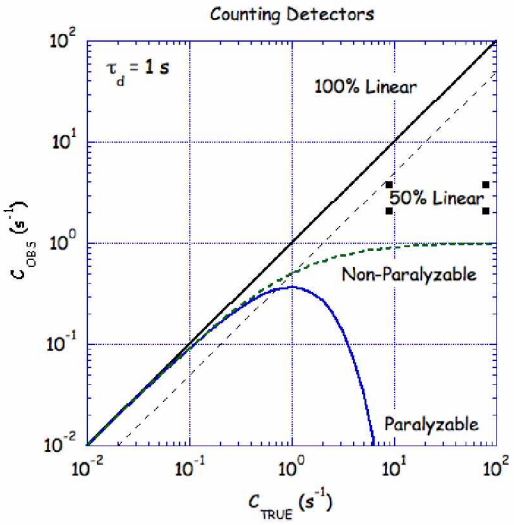

Figure 3.3. Variation of observed count rate C_{OBS} with true count rate C_{TRUE} for a detector with a one second dead time. The detectors are 100% linear (black solid), 50% linear (black dashed), non-paralyzable (green dashed), and paralyzable (blue solid).

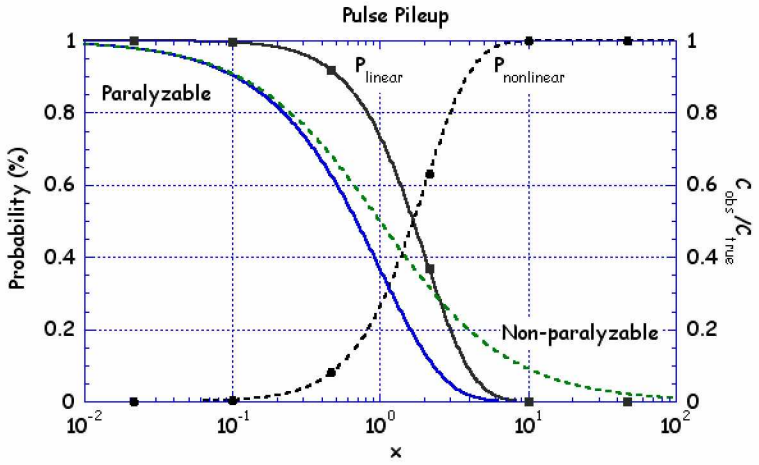

Figure 3.4. Statistical characteristics of pulse pileup as a function of the product of true (or observed) count rate and detector dead time, $x = C_{TRUE}\tau_d$. Probability of no pulse pile up P_{linear} (black closed square), probability of pulse pile up $P_{nonlinear} = 1–P_{linear}$ (dashed black closed circle), ratio of observed to true counts (C_{OBS}/C_{TRUE}) for a non-paralyzable system (green dashed) and for a paralyzable system (blue solid).

3.4. Telescope Trials

3.4.1. 18–19 February 2012

The NICT Rayleigh lidar was operated on the night of the 18–19 February 2012 from 2100 LST until 0654 LST. The lidar system was set up with the PL8020 laser and the 24-inch telescope operating in standard configuration to make standard NICT Rayleigh lidar measurements. The laser beam was first bore-sighted with the 24-inch telescope by steering the laser beam across the telescope FOV and maximizing the lidar signal from 60 km to 65 km. Once the transmitter and receiver were aligned, the observations were started. The raw data profiles consisted of the lidar signal integrated over 1000 laser pulses. Each data set consisted of 16 raw data profiles. Forty-one data sets were acquired during the observation (FB18RY.001–FB18RY.041). Once the NICT Rayleigh lidar was operating routinely, the 41-inch telescope was steered into the laser beam and bore-sighted with the beam based on the lidar signal from 60 to 65 km. Once the 41-inch telescope was bore-sighted, parallel data was acquired with the 41-inch telescope and the 24-inch telescope. The 41-inch telescope observations began at 2245 LST and continued through 0654 LST. The raw data profiles consisted of the lidar signal integrated over 1000 laser pulses. Each data set consisted of 16 raw data profiles. Thirty-four data sets were acquired during the observation (FB1ZRY.001–FB18RZ.034). The operator synchronized the data sets so that FB18RZ.001 was begun at the same time as FB18RY.008 and was acquired simultaneously. Then FB18RZ.002 was begun at the same time as FB18RY.009 and was acquired simultaneously. Finally, FB18RZ.034 was begun at the same time as FB18RY.041 and was acquired simultaneously. Coincident data was taken over 35 sets with both telescopes from 2245 LST to 0654 LST for a total of 544,000 laser pulses. The total signal integrated over this whole observation is plotted as function of altitude in Figure 3.5. The relative error is also plotted in Figure 3.5. The key lidar system parameters are given in Table 3.2. From Figure 3.5, the total lidar signal at 60 km is a factor of approximately three times larger in the 41-inch telescope system

than the 24-inch telescope system. The relative error at 60 km in the 41-inch telescope system is approximately 60% of that in the 24-inch system.

Table 3.2. Rayleigh lidar acquisition parameters for 18–19 February 2012.

Date	Telescope Diameter	Laser	Filter (nm)	Time Period (LST)	Set Name	Number Laser Pulses	Average Per Pulse	FOV (mrad)
02/18/12	Newtonian 24-inch	PL8020	0.3	2245–0654	8/1–41/16	544,000	0.655	1.0
02/18/12	Cassegrain 41-inch	PL8020	1.0	2245–0654	1/1–34/16	544,000	1.79	1.5

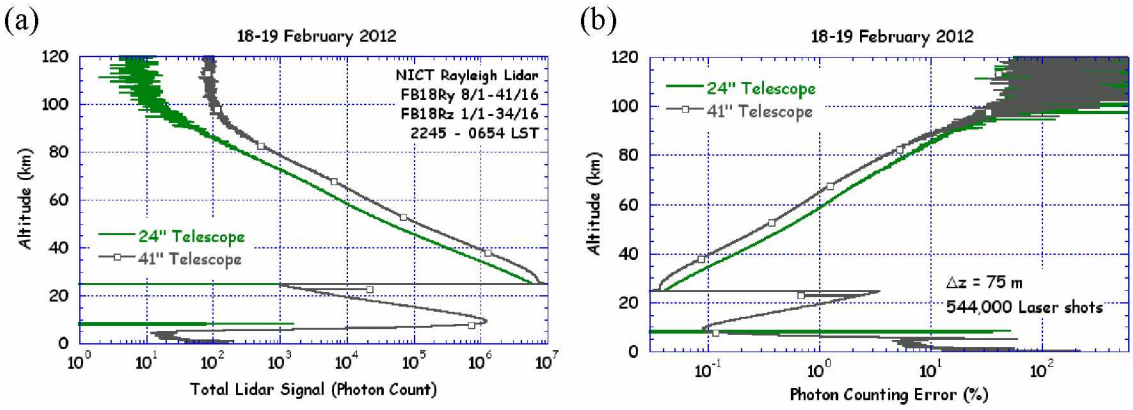

Figure 3.5. (a) Total lidar signal and (b) photon counting error (%) profiles plotted as a function of altitude on 18–19 February 2012 (2245–0654 LST). Signals measured through the 24-inch telescope (green solid line) and 41-inch telescope (gray line with open squares).

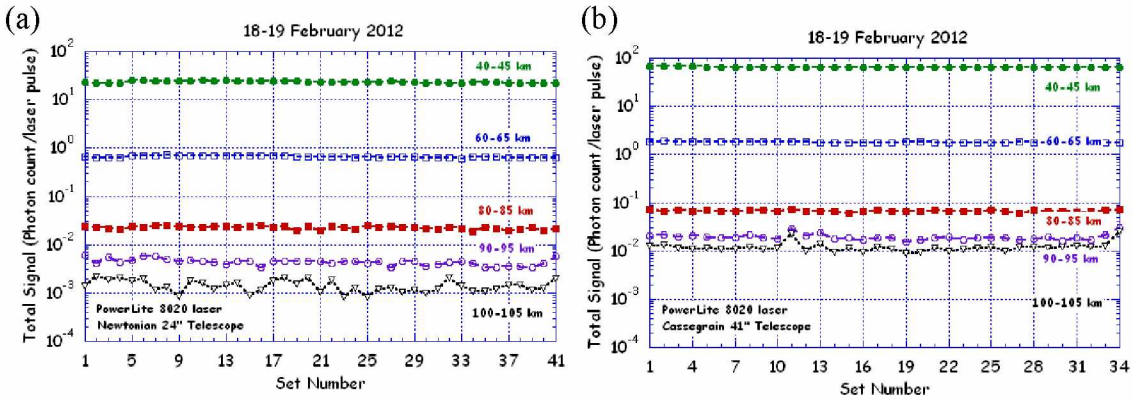

Figure 3.6. Signal levels per-laser-pulse plotted as a function of set number on 18–19 February 2012 (2245–0654 LST). Signals measured through the (a) 24-inch telescope and (b) 41-inch telescope.

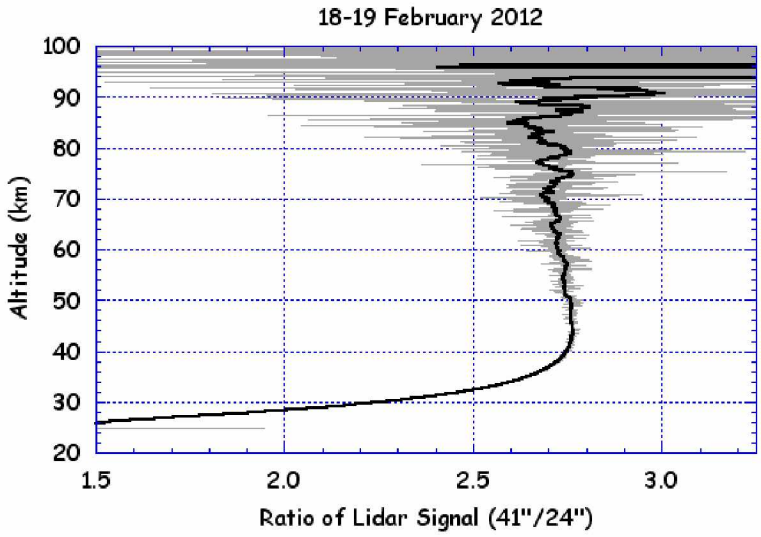

Figure 3.7. Ratio of lidar signal (41-inch/24-inch) on 18–19 February 2012 plotted as a function of altitude (gray line). The 2 km smoothed ratio profile is also plotted (thick black line).

The full statistics of the lidar signal are tabulated in Appendix A. The signal level per laser pulse is plotted as a function of set (16000 laser pulses per set) in Figure 3.5. The 24-inch telescope yields a signal of 0.655 photon counts per-laser-pulse in the 60–65 km altitude range. The 41-inch telescope yields a signal of 1.79 photon counts per-laser-pulse in the 60–65 km altitude range. The signal levels are constant through the night with the incresase in background light levels evident before dawn in the last three sets

(FB18RY.039–FB18RY.041, FB18RY.032–FB18RY.034). This constancy in the lidar signal levels is critical as it means that the effects of pulse pileup are constant through the night. Thus, I can conclude that my analysis based the total lidar signal profile for the night is accurate.

The ratio of the lidar signal in the 41-inch telescope (integrated over 544,000 laser pulses) to that of the 24-inch (integrated over 544,000 laser pulses) is plotted as function of altitude in Figure 3.7. I interpret the ratio profile in Figure 3.6 as follows. I assume that the alignment of the laser beam into the 24-inch telescope is accurate. The technique for steering the laser beam with a divergence of less than 0.1 mrad into the 1 mrad FOV of the 24-inch telescope is well established and robust [Cutler, 2000]. The beam steering mirror is precisely adjusted by the operator using prescision micrometers and the beam can be directed into the center of the telescope FOV based on maximizing the lidar signal from 60 to 65 km. The steering of the 41-inch telescope is done with three rotary mounts at the base of the telecope and is less precise. There is some settling in the telescope when it is moved and so while the FOV of the 41-inch telescope is larger (1.5 mrad) the alignment of the telescope into the beam is less accurate than the alignment of the beam into the telescope. The two telescopes are seperated by about 2 m and the telescopes are about 6 m from the laser beam. In Figure 3.7, the ratio increases with altitude upto 40 km, reaches a maximum of 2.76, and then gently decreases with altitude above 50 km. Thus, I conclude that the laser and 41-inch telescope are slightly misaligned, with complete overlap upto 50 km and then vignetting of the signal above that altitude. The ratio has a value of 2.76 over the 40–50 km altitude region. The ratio of the 60–65 km altitude signals is 2.73. The ratio is much less below 40 km due to more pronounced pulse pileup in the larger 41-inch telescope signals than the 24-inch telescope signals.

I can use these signals to determine the detector dead time for the 41-inch receiver system. I assume that the 24-inch signal is unaffected by pulse pileup above 30 km. The signal (integrated over 544,000 laser pulses in a 75 m (500 ns) range bin) at 30 km based on a 2 km average is 2.39×10^{6} photon counts. The corresponding count rate is 8.79×10^{6}

counts/s. For a detector time of 10 ns, the corresponding value of x is 8.79×10^{-2} or ~0.1. From Figure 3.4, at x = 0.1 the probability of pulse pileup is 0.5%. At 35 km the signal is 8.76×10^{5} photon counts and the corresponding count rate is 3.22×10^{6} counts/s. For a detector time of 10 ns, the corresponding value of x is 3.22×10^{-2} or ~0.03. From Figure 3.4, at x = 0.03 the probability of pulse pileup is 0.05%. At 40 km, the signal is 3.12×10^{5} photon counts and the corresponding count rate is 1.15×10^{6} counts/s. For a detector time of 10 ns the corresponding value of x is 1.15×10^{-2} or 0.01. From Figure 3.4, at x = 0.01 the probability of pulse pileup is 0.01%. Over the 30 to 40 km altitude range, the observed count in the 24-inch telescope increases from 91% to 99% of the true count. In comparison the 41-inch signals at 30 km, 35 km and 40 km are 5.37×10^{6}, 2.32×10^{6}, and 8.56×10^{5} photon counts. The corresponding count rates are 1.98×10^{7}, 8.54×10^{6}, and 3.15×10^{6} counts/s. For a detector time of 10 ns, the corresponding values of x are 0.2, 0.08, 0.03 respectively. From Figure 3.4, the corresponding the probabilities of pulse pileup are 2%, 0.3%, and 0.05%. Over the altitude range of 30 to 40 km the observed count in the 41-inch telescope increases from 82% to 97% of the true count.

I used the Interactive Data Language (IDL©) program routine CURVEFIT to determine the detector dead time for the 41-inch receiver system. I estimated C_{OBS}/C_{TRUE} by taking the ratio in Figure 3.4 and normalizing it by dividing by 2.76. I then fit the non-paralyzable and paralyzable curves to this normalized ratio over the 30 km to 50 km altitude range. The fit yielded a value for the detector dead time of 7.0 ns for the paralyzable system and 7.4 ns for the non-paralyzable system. The result appears robust as a fit over the 30 km to 42.5 km altitude region yielded identical results. For lidar signals at 40 km, the observed count in the 24-inch telescope is 99.2% of the true count.

3.4.2. 22–23 March 2012

The NICT Rayleigh lidar was operated on the night of 22–23 March 2012 from 2039 LST until 0529 LST. The lidar system was set up with the PL8020 laser and the 24-inch telescope operating in the standard configuration mode, detailed above. The 41-inch

telescope was bore-sighted with the laser beam based on the lidar signal from 60–65 km following the procedure used on 18–19 February 2012. Data was taken in parallel with the 24-inch telescope and 41-inch telescope from 2133 LST until 0529 LST (MR22RY.003–MR22RY.034, MR22RZ.004–MR22RZ.035). The 41-inch telescope aperture was reduced by placing a cover around the outer edge of the primary mirror, obscuring ~7-inches of the outside radius. I took reduced aperture data for 13 sets from 2039 LST until 2329 LST (MR22RZ.001–MR22RZ.013). I then removed the cover and took data at full aperture from set 14 through set 35 at 0529 LST (MR22RZ.014–MR22RZ.035).

In this section, I present a 10 set comparison of the 41-inch full aperture (MR22RZ.014–MR22RZ.023) and the 41-inch reduced aperture (MR22RZ.004–MR22RZ.013) for a total of 160,000 laser pulses. The 41-inch reduced aperture telescope is hereafter referred to as the 41-inch-ra telescope. The total lidar signal and relative error is plotted in Figure 3.8 as a function of height. The key lidar system parameters are given in Table 3.3. The full statistics of the lidar signal are tabulated in Appendix A. The signal level per-laser-pulse is plotted as a function of set (16000 laser pulses per set) in Figure 3.9. The 41-inch-ra telescope yields a signal of 0.647 photon counts per-laser-pulse in the 60–65 km altitude range from set 4 through 13. From Figure 3.9, the 41-inch telescope yields a signal of 1.27 photon counts per-laser-pulse in the 60–65 km altitude range from set 14 through 23. The signal levels are relatively constant through the night, with an increase in signal levels at set 14 is due to the increased telescope aperture. The high background signal levels from sets 1 through 4 and sets 29 through 35 reflect the skylight contamination from dusk and dawn. This 9 set comparison of the 41-inch reduced aperture and full aperture signals allow for the determination of the detector dead time without the added nonlinear effects of vignetting at the high altitudes due to misalignment.

Table 3.3. Rayleigh lidar acquisition parameters for 22–23 March 2012.

Date	Telescope Diameter	Laser	Filter (nm)	Time Period (LST)	Set Name	Number Laser Pulses	Average Per Pulse	FOV (mrad)
03/22/12	Cassegrain 41-inch-ra	PL8020	1.0	2133–2329	4/1–13/16	160,000	0.647	2.0
03/22/12	Cassegrain 41-inch	PL8020	1.0	2359–0223	14/1–23/16	160,000	1.27	2.0

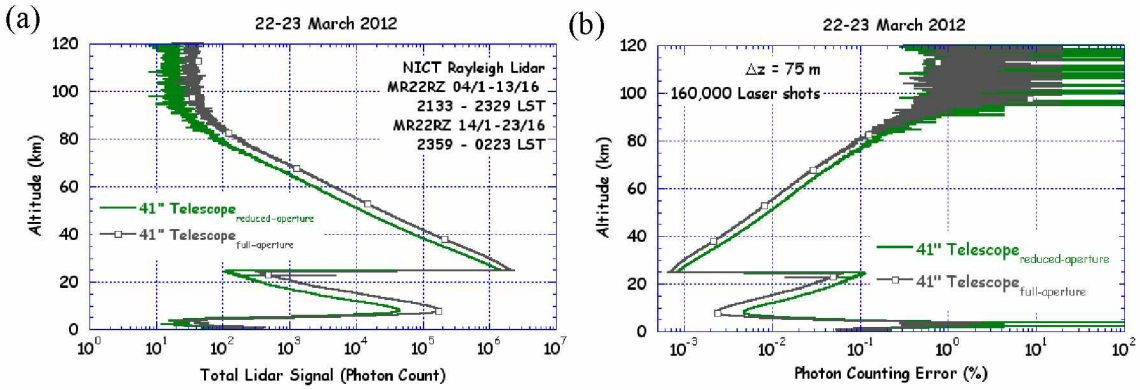

Figure 3.8. (a) Total lidar signal and (b) photon counting error (%) profiles plotted as a function of altitude on 22–23 March 2012 LST. Signals measured through the 41-inch telescope (green solid line) and 41-inch-ra telescope (gray line with open squares).

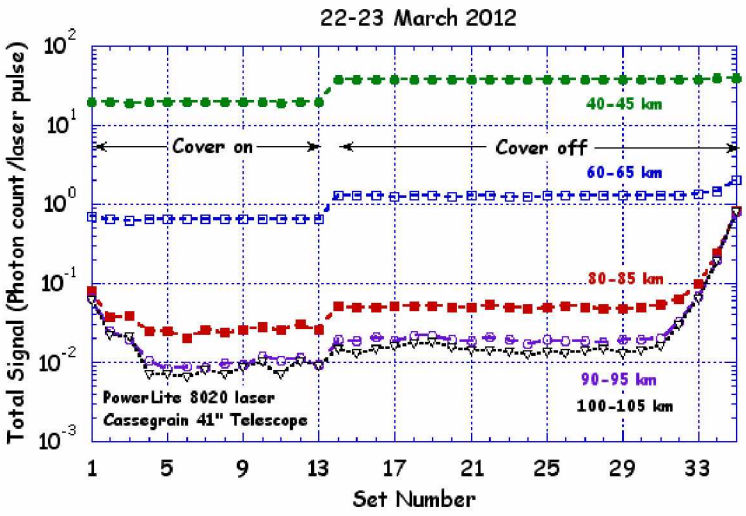

Figure 3.9. Signal levels per-laser-pulse plotted as a function of set number on 22–23 March 2012 (2039–0529 LST).

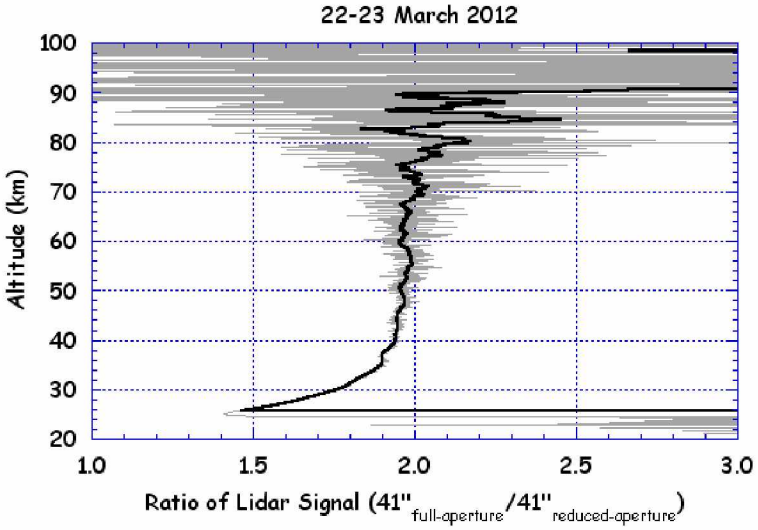

Figure 3.10. Ratio of lidar signal (41-inch/41-inch-ra) on 22–23 March 2012 plotted as a function of altitude (gray line). The 2 km smoothed ratio profile is also plotted (thick black line).

The ratio of lidar signal in the 41-inch-ra telescope (integrated over 160,000 laser pulses) to the lidar signal in the 41-inch telescope (integrated over 160,000 laser pulses) is

plotted in Figure 3.10. The ratio increases with altitude in Figure 3.10, with rapid increase below approxmiately 50 km. An average ratio of 1.95 over the 40 km to 50 km range increases to 1.97 from 50 km to 60 km. The ratio of the 60 to 65 km altitude signals is 1.97. The signal at 30 km based on a 2 km average is 5.61×10^5 photon counts, corresponding to a counting rate of 7.01×10^6 counts/s. For a detector dead time of 10 ns, this gives x = 0.07 and from Figure 3.4 the probability of pulse pileup is 0.2%. At 35 km the signal is 1.98×10^5 photon counts, resulting in a count rate of 2.46×10^6 counts/s. This corresponds to x = 0.08 and gives the probability of pulse pileup of 0.3%. At 40 km the signal from 160,000 laser pulses is 6.68×10^4 photon counts and yeilds 8.35×10^6 counts/s. The probability for this count rate is 0.03%.

The ratio of signals from over the 50–65 km altitude range of 1.97 is assumed to be representative of the signal increase with the 41-inch telescope to the 41-inch-ra telescope. Therefore, I estimated C_{OBS}/C_{TRUE} to be 1.97 and fit the paralyzable and non-paralyzable models over the 30 km to 50 km altitude range. This fit gives a detector dead time of 8.3 ns for the paralyzable system and 8.7 ns for the non-paralyzable system. This represents a robust fit as results were reproducable over the 30 km to 42.5 km alitutde range. For lidar signals at 40 km, the 8.7 ns detector dead time results in the observed counts in the 41-inch-ra telescope 92.9% that of the true count.

3.4.3. 23–24 April and 24–25 April 2012

In this section, I compare lidar signals from measurements made in April 2008 and 2012. Observations in April are important for two reasons. Namely, the atmosphere is warm enough that there are not significant amounts of ice crystals in the air and the variability of the middle atmosphere is less in April than in winter. The presence of these crystals is easily seen by the operator as the lidar beam becomes significantly brighter and there is considerable twinkling in the beam. During winter there can be significant variations in the lidar signal (~50%) due to changes in the atmospheric transmission associated with the presence of ice crystals (also called diamond dust) in the lower atmosphere. For example, measurements taken between November 1997 and April 2005 (116 nightly lidar

temperature profiles over the 40 to 80 km altitude range) had a night-to-night rms variability of 6 K and 9 K in April and March compared with 14 K in both December and January [Thurairajah et al., 2009].

On the nights of 23–24 April 2012 (0004–0308 LST) and 24–25 April 2012 (2319–0224 LST), I made measurements with the Rayleigh lidar system employing the PL8020 and the 41-inch Cassegrain telescope. The PL8020 beam was steered into the FOV of the 41-inch telescope by maximizing the signal in the 70–75 km range. The 41-inch telescope had a 1 mrad FOV defined by a pinhole at the focal point of the telescope. The receiver employed an interference filter with a bandwidth of 1.0 nm and 0.3 nm on the night of 23–24 April, and 24–25 April 2012, respectively. On both nights, 13 sets of data were acquired (AR23RZ.001–AR23RZ.013, AR24RZ.001–AR24RZ.013). The relevant lidar system characteristics are tabulated in Table 3.4. The laser pulse energy was determined from laser power measurements made during the night. The total lidar signal per-laser-pulse as a function of data set is plotted in Figure 3.11. The increase in background signals before sunrise is clearly visible on the morning of the 24 April 2012 from set 6 onwards. The increase in background signals after sunset and before sunrise is clearly visible on the night of 24–25 April 2012 in the initial 4 sets and in set 9 onwards.

On the night of 23–24 April 2008 (2237–0258 LST), measurements were taken with the NICT Rayleigh lidar system employing the PL8020 and the 24-inch Newtonian telescope. The PL8020 beam was steered into the FOV of the 24-inch telescope by maximizing the signal in the 60–65 km range. The 24-inch telescope had a 1 mrad FOV and the receiver had an interference filter with a bandwidth of 0.3 nm. On this night 18 sets of data were acquired (AR23RY.001–AR23RY.018). The relevant lidar system characteristics are given in Table 3.3. The laser pulse energy was determined from laser power measurements made during the night. The total lidar signal per-laser-pulse for each data set is plotted in Figure 3.8.

A comparison of the lidar signals on 23–24 April 2008, 23–24 April 2012, and 24–25 April 2012 for a 2 h period from approximately 0000 through 0200 LST is presented.

During this period the solar altitude angle was between –11.3° to –10.3° [USNO, 2012]. The total lidar signal and relative errors are plotted as function of altitude in Figure 3.12. The lidar signal increases by a factor of approximately 4 at 60 km and the relative error decreases by a factor of 2 between 2008 and 2012 (Figure 3.12). The variation in laser pulse energy between 406 mJ and 364 mJ is typical due to aging of the flashlamps in the laser. In order to compare the signals, I compensate the 2012 signals by the laser pulse energy by multiplying the lidar signal on the 23–24 April 2012 by a factor of 1.11 (= 406/365) and the lidar signal on the 24–25April 2012 by a factor of 1.12 (= 406/364). I then take the ratio of the compensated lidar signals measured in 2012 to that measured in 2008 to assess the impact of the change in telescope. I also take the ratio of the signal measured on the 24–25 April 2012 to that measured on the 23–24 April 2012 to assess the impact of the change in interference filter. I plot these ratio profiles in Figure 3.13. The lidar signals are tabulated in Appendix A and I summarize the ratio profiles in Table 3.5.

Table 3.4. Rayleigh lidar acquisition parameters in late April 2008 and 2012[1, 2].

Date	Telescope Diameter	Filter (nm)	Time Period (LST)	Set Name	Average Per Pulse	Laser energy per pulse (mJ)
04/24/12	Cassegrain 41-inch	1.0	0004–0211	1/1–9/16	2.77	365
04/25/12	Cassegrain 41-inch	0.3	0002–0210	4/1–12/16	3.04	364
04/24/08	Newtonian 24-inch	0.3	0007–0215	7/1–15/16	0.766	406

1: Laser is PL8020
2: 144,000 Laser pulses

Table 3.5. Comparison of power compensated lidar signals in April 2008 and 2012.

Altitude (km)[1]	23–24 April 2012	24–25 April 2012	April 2012
	N_S^*/N_{S2008}	N_S^*/N_{S2008}	Ratio
42.5	3.72	4.12	1.11
62.5	4.24	4.67	1.10
82.5	3.73	4.17	1.12

1: Average over 5 km

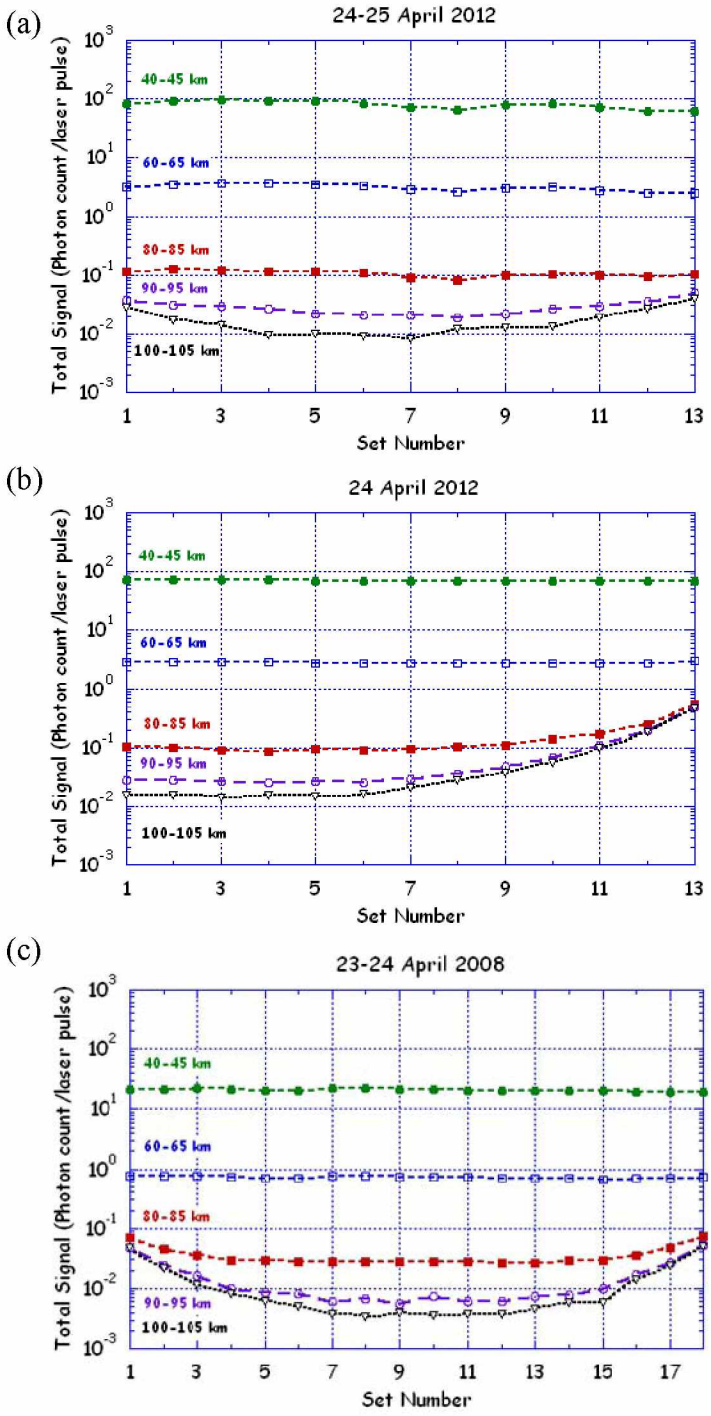

Figure 3.11. Signal levels per-laser-pulse as a function of set number for April 2008 and 2012. Signals measured on (a) 0004–0308 24 April 2012, (b) 2319 24 April–0224 25 April 2012 LST, and (c) 2237 23 April–0258 24 April 2008 LST.

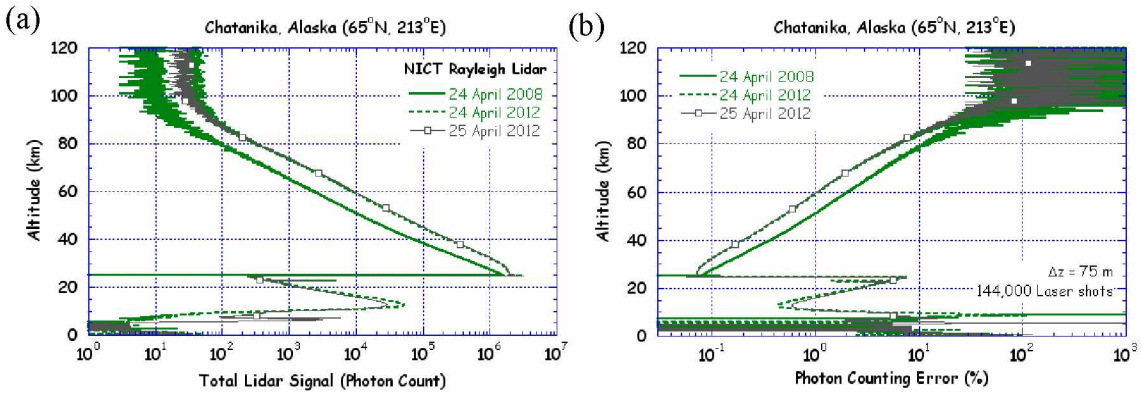

Figure 3.12. (a) Photon count profiles and (b) photon counting error (%) plotted as a function of altitude for April 2008 and 2012. The measurements cover the 2 h period around solar midnight on the nights of 23–24 April 2008 (green solid line), 23–24 April 2012 (green dashed line), and 24–25 April 2012 (gray dotted line).

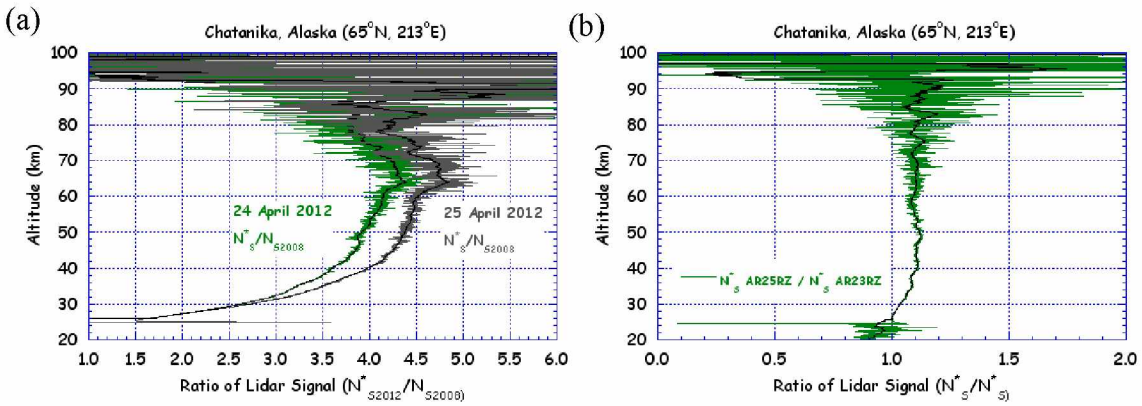

Figure 3.13. (a) Ratio of power compensated lidar signals for 24 April 2012 (dark green line) and 25 April 2012 (gray line), and (b) the ratio of power compensated April 2012 lidar signals. The ratios smoothed by a running 2 km window are also plotted (thin black line).

The effect of pulse pileup due to the larger signal count rates in 2012 is evident at lower altitudes (Figure 3.13). In Figure 3.13, it is clear there is enhanced scattering in the 60–70 km altitude region. This enhanced lidar signal may reflect the presence of aerosol at this altitude range. Therefore, the increase in signal by a factor of approximately 3.72 and 4.17 based on the signals at 42.5 km and 82.5 km on the 23–24 April 2012, and the 24–25 April 2012, respectively. The ratio of the 2012 signals also shows the effect of pulse pileup due to the larger signal count rates on the night of 24–25 April 2012. The 0.3 nm interference filter appears to have a higher transmission than the 1 nm interference filter yielding an increase in signal by a factor of 1.11. On the 18–19 February 2012, I found that the increase in telescope area from the 24-inch Newtonian telescope to the 41-inch Cassegrain telescope yielded an increase in signal by a factor of 2.76. If we correct for the transmission of the interference filter the increase in signal is 3.04. This value is very close to the expected ratio of the areas of the primary mirrors in the telescope of 3.0. The improvement of the lidar signal between 2008 and 2012 is larger than expected from the change in telescope. The change in lidar signal by a factor of 4.17 is a factor 1.37 larger than the ratio of 3.04. The larger ratio than expected probably reflects changes in the atmospheric transmission between the observations. The lidar observers noted that the sky had a white haze on the night of 23–24 April 2008 while the sky was bluer on the nights of 23–24 April 2012 and 24–25 April 2012. The presence of the enhanced scattering at 60–70 km in 2012 will require further investigation beyond the scope of this study.

3.5. Laser Trials

3.5.1. 28–29 March 2012

The NICT Rayleigh lidar was operated on the night of 28–29 March 2012 from 2215 LST through 0442 LST and is first night of measurements using the high power Powerlite 9030 Nd:YAG laser (PL9030). From 2116–2358 LST, measurements were taken with the PL8020 steered into the 24-inch telescope. The PL8020 was beam steered into the 24-

inch telescope by optimizing signal in the 60–65 km altitude range. The 41-inch telescope was then steered into the laser beam and bore-sighted by maximizing signals in the 60–65 km altitude range. The two telescopes took synchronized data sets from 2215–2358 LST with the PL8020 (MR28RY.005–MR28RY.011, MR28RZ.001–MR28RZ.007). The PL9030 was then visually steered into the PL8020 in the sky. The steering procedure was repeated by optimizing signals in the 60–65 km altitude range in both telescopes with the PL9030. The telescopes took synchronized data sets from 0035–0442 LST with the PL9030 (MR28RY.012–MR28RY.037, MR28RZ.008–MR28RZ.034).

The lidar system set up employing the PL8020 and 24-inch telescope is referred to as the NICT system and the set up employing the PL9030 and 41-inch telescope is referred to as the extended system. In this section, I present the comparison of signals integrated over 64,000 laser pulses measured with The NICT system and the extended system (MR28RY.08–MR28RY.011, MR28RZ.008–MR28RZ.011). The total lidar signal and photon counting error profiles are shown in Figure 3.14. The signal level per-laser-pulse is plotted as a function of set (16,000 laser pulses) in Figure 3.15. The full lidar signal statistics are given in Appendix A. The key system parameters are given in Table 3.6.

Table 3.6. Rayleigh lidar acquisition parameters for 28–29 March 2012.

Date	Telescope Diameter	Laser	Filter (nm)	Time Period (LST)	Set Name	Number Laser pulses	Average Per Pulse	FOV (mrad)
03/28/12	Newtonian 24-inch	PL8020	0.3	2258–2358	8/1–16/16	64,000	0.891	1.0
03/28/12	Cassegrain 41-inch	PL9030	1.0	0035–0111	8/1–16/16	64,000	3.64	2.0

The NICT system yields a signal of 0.891 photon counts per-laser-pulse in the 60–65 km altitude range. The extended system yields a signal of 3.64 photon counts per-laser-pulse in the 60–65 km altitude range, a factor of 6.46 times that of the NICT system. From 40–45 km, the NICT system signal was 29.9 photon counts per-laser-pulse and the NICT

system signal was 108 photon counts per-laser-pulse, 3.61 times larger than the NICT system. The ratio is much lower from 40–45 km due to the appreciable amount of pulse pileup in the extended system signal. At 50 km, the signal averaged over 2 km is 2.56×10^4 photon counts in the extended system and 6.27×10^3 in the NICT system system, yielding a ratio of 4.08. From Figure 3.16, we can see that the ratio of the extended system signal to the NICT system signal is nearly constant at 4.14. The data is very noisy because signals are only integrated over 64,000 laser pulses. It is clear in Figure 3.14 that the extended system signals are more statistically robust than the NICT system signals even though the temporal resolution of the extended system signals is lower. The extended system (30 pps) signals represent the integrated signal over 35.6 minutes whereas The NICT system signals (20 pps) has a temporal resoltuion of 53.3 minutes.

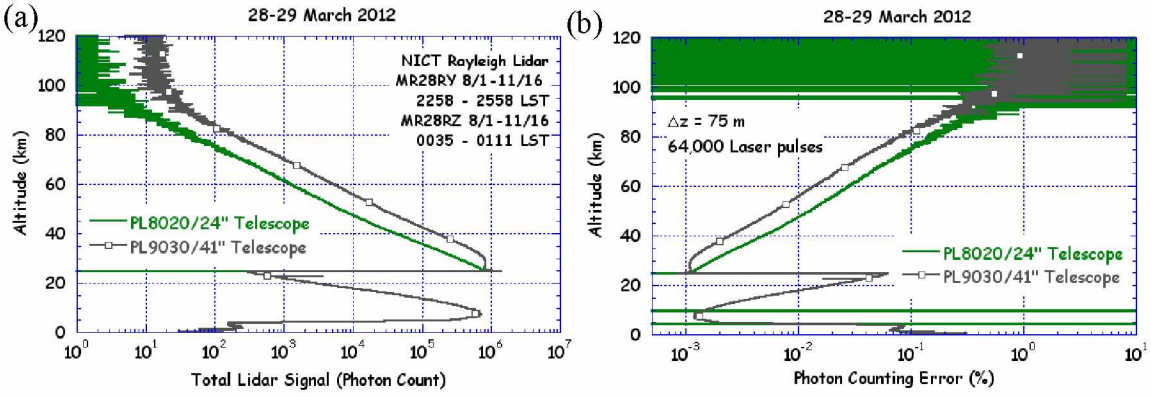

Figure 3.14. (a) Total lidar signal and (b) photon counting error (%) profiles plotted as a function of altitude on 28–29 March 2012 LST. Signals measured through the 41-inch telescope with PL9030 laser (green solid line) and 24-inch telescope with PL8020 laser (gray line with open squares).

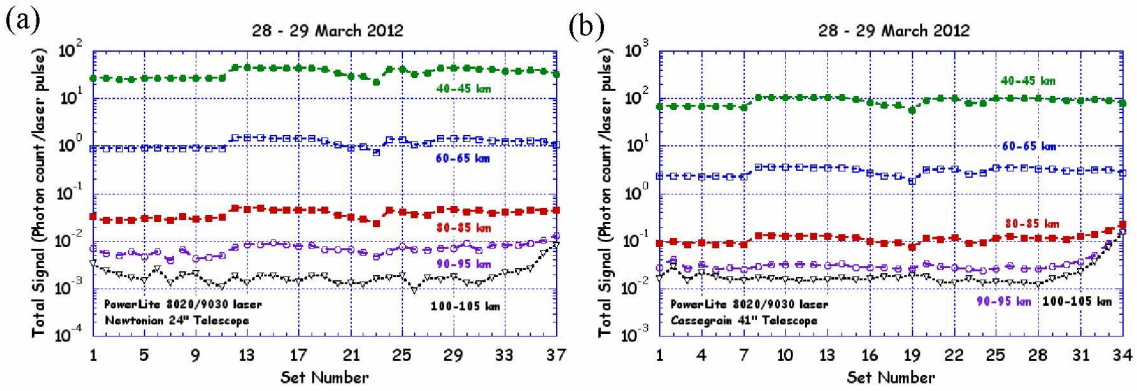

Figure 3.15. Signal levels per-laser-pulse plotted as a function of set number on 28–29 March 2012 (2215–0442 LST). Signals measured through the (a) 24-inch telescope and (b) 41-inch telescope.

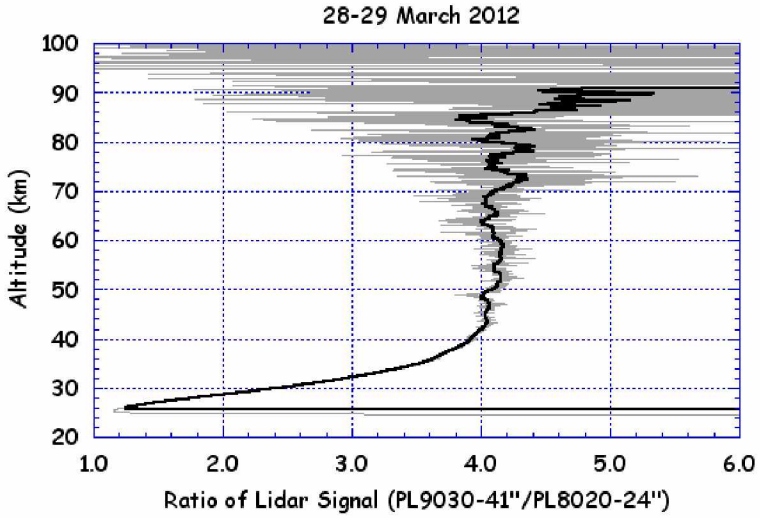

Figure 3.16. Ratio of lidar signal (PL9030 41-inch/PL8020 24-inch) on 28–29 March 2012 plotted as a function of altitude (gray line). The 2 km smoothed ratio profile is also plotted (thick black line).

3.5.2. 3–4 April 2012

Alternating sets of data were taken through the 41-inch telescope with the PL8020 and PL9030 on the night of 3–4 April 2012. Both lasers were bore-sighted in the 41-inch

telescope by maximizing signal in the 60 km to 65 km altitude range. The first two and last two sets represent the signal from the PL8020 and PL9030, respectively. A schematic of the method of data acquisition is shown in Figure 3.17. The specific sets measured with the PL8020 and PL9030 are listed in Appendix A. The data was processed to yield individual measurements with each laser by using bad files (AR8020RZ.BAD and AR9030RZ.BAD) that are read by the data processing programs (see Wang [2003] for a discussion of the processing method). The key parameters are shown in Table 3.7 and the full lidar signal statistics are given in Appendix A. The total lidar signal and photon counting error are shown in Figure 3.18.

The total signal per-laser-pulse measured on 4 April 2012 (Figure 3.19a) clearly shows the difference in the two lasers. Sky conditions are stable over the course of observations, with background signals rising at set 15 in Figure 3.19a, corresponding to a sun elevation angle of approximately –12° [USNO, 2012]. Between the 40 and 80 km altitude range, the ratio of signals stabilizes at approximately 2.4. Below ~40 km the signal is dominated by pulse pileup and above ~90 km signals are dominated by background skylight.

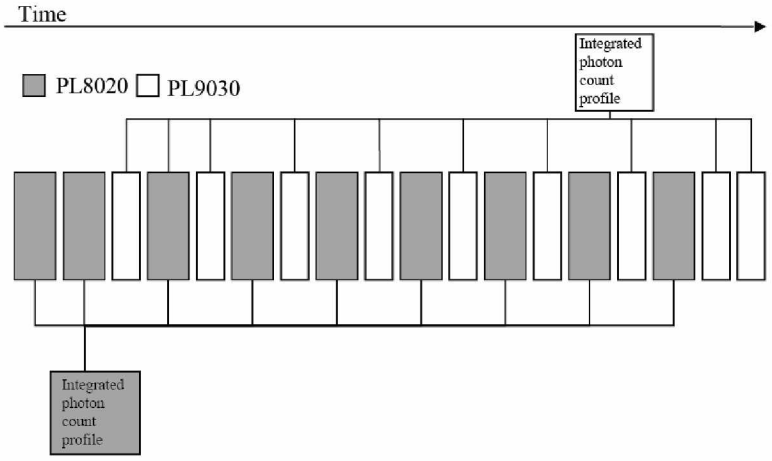

Figure 3.17. Schematic illustration of real time data set acquisition and processing method on the night of 4 April 2012.

Table 3.7. Rayleigh lidar data acquisition parameters for 4 April 2012.

Date	Telescope Diameter	Laser	Filter (nm)	Time Period (LST)	Set Name	Number Laser pulses	Average Per Pulse	FOV (mrad)
04/04/12	Cassegrain 41-inch	PL8020	1.0	0024–0355	Alternating	144,000	1.95	2.0
04/04/12	Cassegrain 41-inch	PL9030	1.0	0109–0414	Alternating	144,000	4.57	2.0

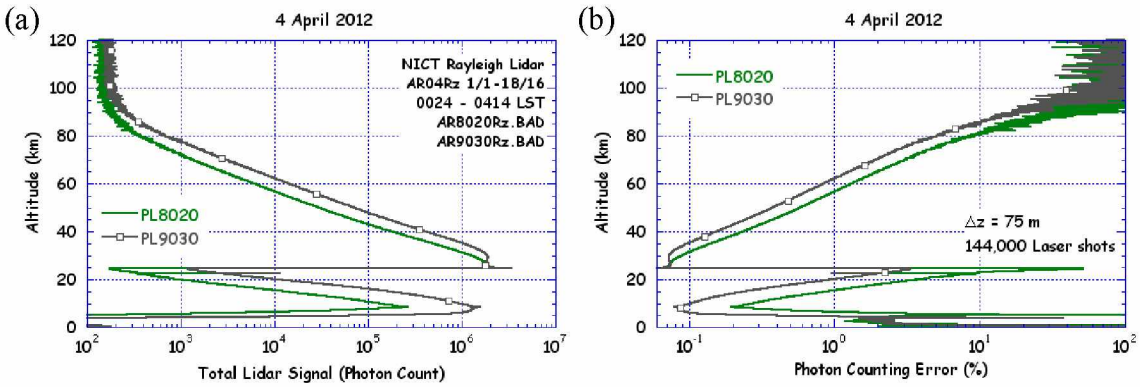

Figure 3.18. (a) Total lidar signal and (b) photon counting error (%) as a function of altitude on 4 April 2012.

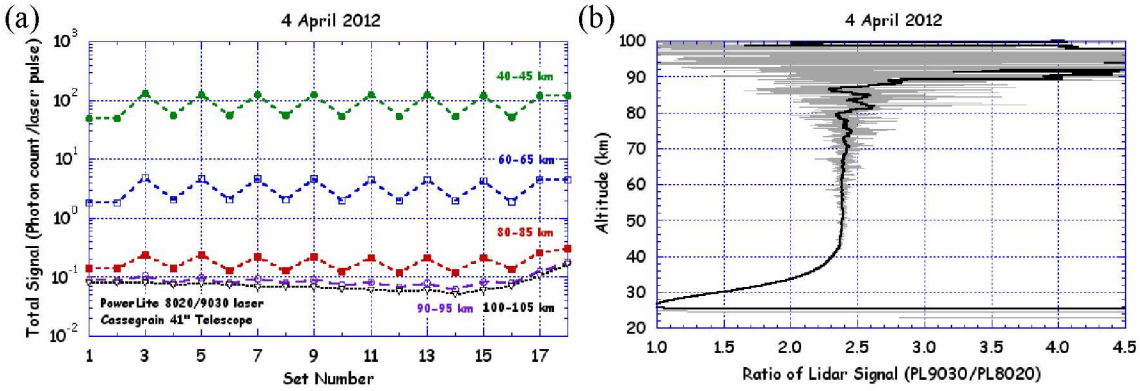

Figure 3.19. (a) Signal levels and (b) ratio of lidar signal (PL9030/PL8020) on 4 April 2012.

The ratio of the PL9030 lidar signal to the PL8020 lidar signal at 40 km based on a 2 km average is 2.31. The ratio increases to 2.37 at 45 km then remains at 2.38 between 50 km and 65 km. The constant ratio above 50 km is confirmation that steering the laser beam into the telescope FOV rather than steering the telescope into the laser beam yields better alignment. The signal (integrated over 144,000 laser pulses) at 40 km based on a 2 km average is 1.82×10^{5} photon counts and gives a count rate of 2.53×10^{6} counts/s measured with the PL8020. Using a conservative estimate of 8.7 ns for the detector dead time, the observed count rate gives a value of $x = 2.20\times10^{-2}$ or ~0.02, and gives a 0.02% probability of pulse pileup in the PL8020 and 41-inch telescope system. This results in the observed count rate being 98% of the true or expected count rate for both a paralyzable and non-paralyzable detector system. The signal at 40 km measured with the PL9030 and 41-inch telescope system is 4.21×10^{5} photon counts and gives a count rate of 5.85×10^{6} counts/s. Using a detector dead time of 8.7 ns, the observed count rate results in $x = 5.09\times10^{-2}$ or ~0.05. From Figure 3.4, at x = 0.05 there is a 0.12% probability of pulse pileup in the PL9030. For a paralyzable and non-paralyzable detector, the observed count rate is 95% of the true or expected count rate.

Nonlinearities in the raw photon count signal corrupt the temperature because the lidar retrieval method interprets the reduced signal as a decrease in atmospheric density. The lidar retrieval method depends on the assumption of hydrostatic equilibrium and uses the ideal gas law. Thus, lower densities appear as higher temperatures. The temperature profiles generated from the lidar signals integrated over 144,000 laser pulses is plotted in Figure 3.20a and the absolute value of the temperature difference is plotted in Figure 3.20b.

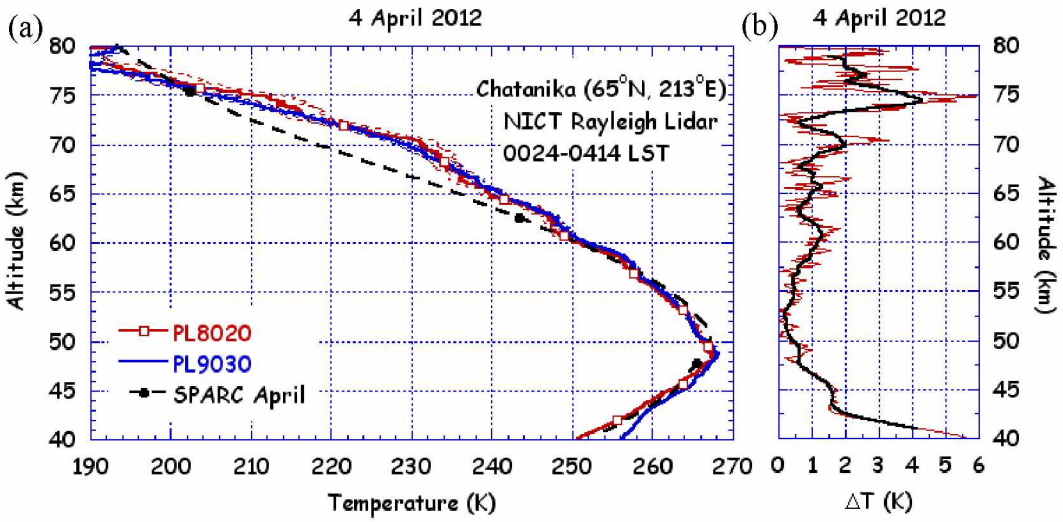

Figure 3.20. Temperatures measured by the PL8020 and PL9030 on 4 April 2012. Plotted are (a) temperatures measured by the PL8020 (red) and PL9030 (blue) on 4 April 2012 and temperatures from the SPARC reference atlas (black dashed with solid circles), and (b) temperature difference ΔT (thin red) and ΔT smoothed by 2 km (thick black).

Lidar temperatures on the night of 3–4 April 2012 and temperatures reported by SPARC show the stratopause at 49 km and 269 K with temperatures uniformly decreasing with height above. The increase in the temperatures reported by the lidars above 78 km is due to the initial temperature at 80 km. The agreement between the PL8020 temperatures and the PL9030 temperatures is not perfect. The difference is greatest at the 40 km and 75 km when the temperatures depart by nearly 6 K. At 40.1 km, PL9030 temperature is warmer than the PL8020 temperature by 5.7 K, and at 74.9 km the PL8020 temperature is 5.9 K warmer than the PL9030 temperature.

The difference in temperature near 75 km could possibly be due to the difference in temporal resolution between the two lasers. While the lasers operated for the same number of laser pulses, the PL8020 was taking measurements of the atmosphere for 120 minutes whereas the PL9030 was only sampling the atmosphere for 80 minutes. Therefore, although the data was taken in alternating sets to avoid biases in atmospheric

variability, the temperature retrieved from the PL8020 data represents the average over a longer period of time. At 80 km, the 2 km averaged lidar signal measured by the PL9030 and 41-inch telescope was 5.18×10^2 photon counts, 3.00×10^2 photon counts more than the lidar signal of 2.18×10^2 photon counts measured by the PL8020 and 41-inch telescope. I attribute the difference of 5.7 K at the lowest altitude to signal contamination from pulse pileup. At 40 km, the 2 km averaged lidar signal measured by the PL9030 and 41-inch telescope was 4.21×10^5 photon counts, 2.39×10^5 photon counts greater than the lidar signal of 1.82×10^5 photon counts measured by the PL8020 and 41-inch telescope.

The warmer temperature due to the nonlinear lidar signals at low altitudes underscores the importance of correcting for pulse pileup. If left unresolved, this would lead to a bias in reported temperatures. The magnitude of the temperature difference is significant, especially when warming and cooling trends in the middle atmosphere are on the scale of 1–2 K per decade. For example, lidar observations from the Observatoire de Haute Provence (OHP) in France (44°N, 6°E) over a 20 year period yielded a cooling of 0.4 K per year in the mesosphere and 0.1 K per year in the stratosphere [Keckhut et al., 1995].

3.6. Summary

In this Chapter, I have presented field tests from telescope trials in February, March, and April 2012, and laser trials in March and April 2012. These field trials were carried out while supporting the continuous routine operation of the NICT Rayleigh lidar system at Chatanika. The field test have allowed me characterize the effects of nonlinearities in the photon counting receiver and determine an experimental range of detector dead times in the system. Based on two nights of observations, the detector dead time estimates ranged from 7.0 to 8.7 ns, larger than the 5 ns pulse duration of the PMT and the 6.7 ns counting interval of the MCS unit.

Furthermore, the field tests have allowed me to characterize the performance of the extended lidar system and determine the upper altitude accessible for temperature retrievals. Table 3.8 summarizes the lidar signal integrated over 144,000 laser pulses

(64,000 laser pulses on 28–29 March 2012) and the relative photon signal error from these field tests. Table 3.9 is the average 2 h lidar signals and relative photon signal error. From Table 3.9, the lidar signal measured with the PL9030 and 41-inch telescope shows an improvement of 6.5, 6.7, 6.6, and 7.4 times the lidar signal measured with the PL8020 and 24-inch telescope over the 60–65, 70–75, 80–85, and 90–95 km altitude range, respectively. The improvement of 5.9 over the 40–45 km altitude range is contaminated by pulse pileup and therefore does not reflect the accurate improvement. The measured improvements are less than the expected improvement with the extended lidar system of 8.4 compared to the NICT lidar system and reflect the systematic differences in system optics and electronics.

Table 3.8. Performance of the NICT and extended lidar systems.

Date	Laser	Telescope	N_S (Photon Count)[1]/ΔN_S / N_S (%)				
			40–45 km	60–65 km	70–75 km	80–85 km	90–95 km
2/18-19/12	20 pps[2]	24-inch	$53954/4.3\times10^{-1}$	$1505/2.6\times10^{0}$	$285/5.9\times10^{0}$	$49/1.5\times10^{1}$	$7/4.3\times10^{1}$
3/28-29/12	20 pps[3]	24-inch	$26096/6.2\times10^{-1}$	$868/3.4\times10^{0}$	$161/7.9\times10^{0}$	$29/1.9\times10^{1}$	$4/5.7\times10^{1}$
4/23-24/08	20 pps[2]	24-inch	$45704/4.7\times10^{-1}$	$1586/2.5\times10^{0}$	$314/5.7\times10^{0}$	$51/1.5\times10^{1}$	$7/6.0\times10^{1}$
2/18-19/12	20 pps[2]	41-inch	$144127/2.6\times10^{-1}$	$3997/1.6\times10^{0}$	$752/3.7\times10^{0}$	$128/9.6\times10^{0}$	$21/3.1\times10^{1}$
3/22-23/12	20 pps[2]	41-inch	$82723/3.5\times10^{-1}$	$2758/1.9\times10^{0}$	$474/4.7\times10^{0}$	$82/1.3\times10^{1}$	$13/5.0\times10^{1}$
4/23-24/12	20 pps[2]	41-inch	$152782/2.6\times10^{-1}$	$6042/1.3\times10^{0}$	$1154/3.0\times10^{0}$	$173/8.4\times10^{0}$	$26/3.1\times10^{1}$
4/24-25/12	20 pps[2]	41-inch	$168617/2.4\times10^{-1}$	$6635/1.2\times10^{0}$	$1262/2.8\times10^{0}$	$192/7.7\times10^{0}$	$26/2.8\times10^{1}$
4/03-04/12	20 pps[2]	41-inch	$116015/2.9\times10^{-1}$	$4127/1.6\times10^{0}$	$820/3.8\times10^{0}$	$140/1.2\times10^{1}$	$21/6.2\times10^{1}$
4/03-04/12	30 pps[2]	41-inch	$272567/1.9\times10^{-1}$	$9852/1.0\times10^{0}$	$1978/2.3\times10^{0}$	$347/6.6\times10^{0}$	$57/2.6\times10^{1}$
3/28-29/12	30 pps[3]	41-inch	$104251/3.1\times10^{-1}$	$3532/1.7\times10^{0}$	$676/3.9\times10^{0}$	$113/9.9\times10^{0}$	$18/3.1\times10^{1}$

1: Measurements represent the integrated signal averaged over 5 km
2: 144,000 laser pulses
3: 64,000 laser pulses

Table 3.9. Assessment of the extended lidar system over 2 h[1].

Laser	Telescope	N_S (Photon Count)/ΔN_S / N_S (%)				
		40–45 km	60–65 km	70–75 km	80–85 km	90–95 km
20 pps	24-inch	52791 / 0.44%	1681 / 2.5%	320 / 5.6%	55 / 14%	8 / 47%
20 pps	41-inch	132853 / 0.28%	4712 / 1.5%	892 / 3.6%	143 / 10%	21 / 40%
30 pps	41-inch	312207 / 0.18%	10886 / 0.96%	2130 / 2.2%	364 / 6.0%	59 / 21%

1: Average of the signals presented in Table 3.6 scaled to signals integrated over 2 h.

These field tests establish that the upper altitude of 80 km previously used for temperature retrievals [e.g., Thurairajah et al., 2009] can be extended by 10 km.

However, the lidar signal at the lowest altitude of temperature retrieval (40 km) is contaminated by pulse pileup and requires further development of a method to systematically correct for this. These tests have demonstrated that a system employing a dual telescope receiving system [Alpers et al., 2004] to detect signals from the lower atmosphere at reduced rates is not practical. Both telescopes cannot be aligned with sufficient accuracy to ensure bore-sighting of both telescopes with the laser. Various methods have been developed to correct for count loss due to pulse pileup. These include having two channels within the receiver to separate the incoming light from lower altitudes (e.g., below 50 km) and from the higher altitudes (e.g., above 50 km) [von Zahn et al., 2000], and combining analog-to-digital (AD) and photon counting signal detection in the PMT [Liu et al., 2009].

The maximum count rate for the receiver system is found using the experimentally determined detector dead time of 8.7 ns and given an acceptable linear operating threshold. For example, signals measured by a system with a detector dead time of 8.7 ns and with a 99.9% probability of no pulse pileup correspond to the maximum count rate of 5.17×10^6 counts/s. To have 99.99% confidence that the signal is free of pulse pileup, the maximum count rate is 1.95×10^6 counts/s. To estimate the true count rate from the 40–45 km altitude range in the extended system, I scale the signal in Table 3.9 of 312207 photon counts by the ratio of the extended system lidar signal to the original lidar system from 90–95 km (i.e. 7.4/5.9) to yield 3.92×10^5 photon counts. The scaled lidar signal of 3.92×10^5 photon counts yields a count rate of 5.44×10^6 counts/s, 1.05 times larger than the maximum count rate of 5.17×10^6 counts/s determined by the 99.9% threshold. Therefore, if a beam splitter were placed before the PMT that directed 10% of the incident light to another PMT, the count rate would fall below the 99.9% threshold. A 10% reduction to the incoming signal would reduce the 80 km signal to 3.28×10^2 photon counts and would still allow for the upper altitude to be extended by 10 km.

Chapter 4. Mesospheric Inversion Layers at Chatanika and their Relationship to Planetary Wave Structure

4.1. Introduction

Schmidlin [1976] was the first to report MILs using temperature measurements from acoustic grenades, falling spheres, thermistors, and pitot probes. Schmidlin recognized MILs as a regular climatological feature in the mesospheric temperature profile. MILs are defined as a layer of increasing temperature in the mesosphere and represent a departure from the expected positive atmospheric lapse rate ($\Gamma = -\partial T/\partial z$) observed in the mesosphere due to reduced solar heating. Many formation mechanisms have been proposed for MILs, such as gravity wave breaking [Hauchecorne et al., 1987], nonlinear interactions of gravity waves and tides [Liu and Hagan, 1998; States and Gardner, 2000], chemical heating [Meriwether and Mlynczak, 1995], and planetary wave breaking and dissipation [Wu, 2000; Salby et al., 2002; Sassi et al., 2002; Oberheide et al., 2006], underscoring the complexity of the phenomenon.

The review by Meriwether and Gerrard [2004] identifies two types of MILs as the "upper" (~85–100 km) and "lower" MIL (~65–80 km) in an attempt to better quantify the complex physical processes responsible for their formation. The proposed formation mechanism for the "upper" MIL is a nonlinear gravity wave–tidal interaction and the "lower" MIL is the dissipation of upward propagating planetary waves as they encounter a critical wind line. However, Meriwether and Gerrard [2004] note that the distinction between the upper and lower MIL can become complicated because the altitude distribution of the two mechanisms vary with season and latitude.

MILs reported by ground based lidars emphasize the presence of near adiabatic lapse rates above the inversion [e.g., Whiteway et al., 1995; Thomas et al., 1996; Collins et al., 2011]. A persistent near adiabatic topside lapse rate allows for the development of

convective and/or dynamic instability and regions of turbulent mixing. Below the inversion, atmospheric stability is enhanced due to the negative lapse rate. Instabilities associated with MILs contribute to the development of phenomena such as mesospheric radar echoes [Thomas et al., 1996] and atmospheric bores [Taylor et al., 1995; Dewan and Picard, 1998; Dewan and Picard, 2001; Nielsen et al., 2012]. The occurrence of MILs in the mesosphere and lower thermosphere (MLT) adds complexity to the fluid mechanics of the region where physics are governed by hydrodynamics below (~80 km) and free molecular flow dominates above [Meriwether and Gerrard, 2004].

Recently, Collins et al. [2011] analyzed a MIL observed in the presence of the mesospheric sodium layer at Chatanika. Collins and co-workers were able to retrieve temperatures from 40–90 km in the average profile and from 40–82 km in the successive 2 h profiles with the use of simultaneous ionization gauge measurements from a rocket as the initial temperature (rather than a climatology) in the temperature retrieval. The authors used the observation to characterize vertical diffusive transport coincident with the adiabatic lapse rate on the topside of the MIL. A lower bound to the eddy diffusion coefficient was found to be significantly larger than those reported by Lübken [1997] for Arctic mean wintertime values, and similar to those found in a super-adiabatic layer near 75 km [Lehmacher and Lübken, 1995] and a region of static instability near 85 km [Bishop et al., 2004].

Wave breaking is a principle mechanism of wave dissipation and leads to the formation of distinct surf zones in the stratosphere and mesosphere [McIntyre and Palmer, 1984]. The stratospheric surf zone forms when planetary waves that are refracted by the polar night jet encounter a critical wind line on the equatorward side of the vortex (for quasistationary waves the critical wind line is $\bar{u} = 0$). The formation of the mesospheric surf zone (~70–80 km) is formed through the interaction of gravity and planetary waves. Gravity waves that propagate up through the polar night vortex break near 75 km at middle and high latitudes and deposit easterly momentum, decelerating the polar night jet and causing a reversal in the zonal circulation [Holton, 1983; Garcia and Solomon, 1985].

Sassi et al. [2002] used the Whole Atmosphere Community Climate Model (WACCM) to model the propagation and dissipation of planetary waves as they encounter the critical line where the zonal winds reverse near 75 km at middle at high latitudes. The planetary waves break in the 10 km deep mesospheric surf zone. If the wind reversal setup by gravity waves was not present, planetary waves could dissipate into the lower thermosphere.

Oberheide et al. [2006] used November 1994 data from the Cryogenic Infrared Spectrometers and Telescopes for the Atmosphere (CRISTA) experiment to analyze the relationship between MILs and the mesospheric surf zone. The observations revealed that planetary waves decayed rapidly in the mesospheric surf zone and the abrupt vertical phase shift of planetary waves was large enough to induce strong vertical geopotential curvature. Through hydrostatic equilibrium, the induced vertical curvature in geopotential was large enough to yield inversions in the temperature profiles, consistent with the interpretation of Sassi et al. [2002] and Salby et al. [2002]. The observations were reproduced in the simulations of the Thermosphere–Ionosphere–Mesosphere-Electrodynamics General Circulation Model (TIME-GCM), although the model features were seen approximately 10 km higher in altitude due a higher zero wind line than observed in CRISTA. The zero wind line in the CRISTA geostrophic zonal winds was found at 80 km at high latitudes and 90 km in subtropical and middle latitudes. They found that strong vertical curvature in geopotential wave perturbations was the dominant process of MIL generation in the subtropics and a large contributor to MIL generation at high latitudes. Observations at higher latitudes (56°N) revealed smoother geopotential phase transitions than observed at subtropical latitudes (26°N) and the MIL no longer coincided with the maximum temperature perturbation. High latitude MILs were more prominent and their altitude distribution was more variable compared to subtropical MILs. Oberheide et al. [2006] concluded that their observations indicated that additional processes are involved in the formation of MILs at high latitudes.

Recently, Gan et al. [2012] presented the global characteristics of the lower MIL using the Sounding of the Atmosphere using Broadband Emission Radiometry (SABER) instrument aboard the Thermosphere Ionosphere Mesosphere Energetics Dynamics (TIMED) satellite from 2002 to 2010. The occurrence rate, amplitude, bottom height, and thickness all exhibited strong latitudinal dependences, with the occurrence rate and amplitude at middle latitudes lower than those at low latitudes. Low and middle latitude lower MILs showed clear semi-annual and annual cycles, respectively, with low latitude MILs in spring and autumn higher and narrower than midlatitude winter MILs. The occurrence rate exhibited weak inter-annual variation in the winter Northern Hemisphere. Gan and co-workers focused on low and middle latitudes due to discontinuity of SABER data poleward of 52°. Gan et al. [2012] concluded that low latitude MILs are formed primarily by the joint contribution of the diurnal migrating tide present in the equatorial mesosphere and the semi-annual oscillation of the background temperatures. The occurrence and amplitude of the MILs correlated with the amplitude of the tides and the semi-annual oscillation. At higher latitudes, the authors found that the stationary and traveling planetary wave-one are the dominant large-scale waves. MILs observed from November–January were closely correlated with the planetary wave transient structures. In a case study in December 2003, Gan and co-workers found that the stationary planetary wave-one and 16-day wave were the dominant contributions to the formation of MILs. Therefore, in addition to the planetary wave dissipation mechanism proposed by Salby et al. [2002], Gan et al. concluded that the transient structure of planetary waves contribute to the formation of large spatiotemporal MILs at middle latitudes.

Measurements of density and temperature profiles over Chatanika, Alaska (65°N, 213°E) have been ongoing since the National Institute of Information and Communications Technology (NICT) Rayleigh lidar was installed at Poker Flat Research Range (PFRR) in November 1997. The lidar observations were initiated during the Alaska Project [Murayama et al., 2007] to study the Arctic middle atmosphere and it is operated jointly by the Geophysical Institute (GI) of the University of Alaska Fairbanks and NICT. Cutler et al. [2001] analyzed 27 nights of Rayleigh lidar observations at Chatanika from

1997 through 2000 and reported MILs in 39 h out of the total 210 h of observations. MILs were found on five occasions with mean amplitude of 18 K, peak altitude of 60 km, and topside lapse rates approaching the adiabatic lapse. The MILs characterized in 2 h temperature profiles had a mean phase progression of 0.2 km h^{-1} (0.3 to –0.3 km h^{-1}). MILs were found to have an hourly occurrence rate of 30% in March, 30% in October, and 50% in November, with none observed during the 111 h of observations from December through February. The current study uses temperature profiles measured by the NICT Rayleigh lidar from November 1997 – April 2005 and November 2007 – May 2009 to investigate the occurrence and characteristics of MILs over Chatanika, Alaska. Lidar temperature retrievals are only available from August – May due to the high solar background levels in June and July at Chatanika. Therefore, this study does not attempt to speculate on the formation mechanism of MILs during summer months.

This chapter is organized as follows; in section 2 the methods used for MIL detection in NICT Rayleigh lidar temperatures, and SABER instrument are introduced. Section 3 presents the characteristics of MILs observed by the NICT Rayleigh lidar at Chatanika from 1997 through 2009, and section 4 presents MILs observed by lidar in the context of planetary wave activity using SABER data at 65°N. Section 5 discusses the implications of our results in terms of previously proposed formation mechanisms, and section 6 gives a summary.

4.2. Methods

4.2.1. NICT Rayleigh lidar MIL detection metric

The NICT Rayleigh lidar system was described in Chapter 2. This study uses 149 nightly averaged temperature profiles measured by the NICT Rayleigh lidar from November 1997 – April 2005 and November 2007 – May 2009 (Figure 4.1) to investigate the occurrence and characteristics of MILs over Chatanika, Alaska (65°N, 213°E). This study was restricted to the 149 observation periods with a duration greater than 4.0 h to eliminate small scale noise and transient gravity wave activity [Duck and Greene, 2004],

totaling 1220 h of nightly mean temperature profiles from 4.1 h to 15.4 h with an average of 8.2 h. Density was determined from the 2 km smoothed raw photon count profile to reduce uncertainty due to the photon counting noise. Temperatures were then calculated using downward integration from an assumed initial temperature at 80 km. In this study, the SPARC reference atlas temperature at 80 km [SPARC, 2002; Randel et al., 2004] is used as the initial temperature. Due to the propagating contribution from this initial temperature, the characteristics of MILs reported are restricted to those with a peak altitude less than or equal to 70 km in the average nightly temperature profile (79 MILs in 55 days). However, when examining the qualitative relationship between the occurrence of MILs and planetary wave structure, all MILs with a peak altitude below 80 km (138 MILs in 89 days) observed in the average lidar temperature profile are considered. The uncertainties considered are only uncertainty due to the statistical uncertainty in the raw photon count profile below 70 km.

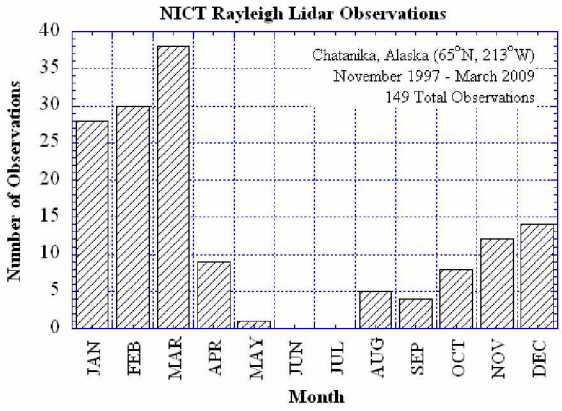

Figure 4.1. Monthly distribution of NICT Rayleigh lidar observations at Chatanika

The MIL detection metric used in this study is as follows: a MIL is characterized if the lapse in temperature changed from positive to negative (i.e. from decreasing temperature with altitude to increasing temperature with altitude) in the region between the stratopause and 70 km. The point at which the negative lapse rate begins is defined as the base altitude of the MIL (MIL minimum), and the peak altitude (MIL maximum) is defined as the altitude where temperatures reach a maximum and above which positive

lapse is restored. The MIL is significant if the temperature difference between base and peak altitude is greater than the associated statistical error due to photon counting ($T_{min} + \delta T_{min} < T_{max} - \delta T_{max}$) in the average nightly temperature profile. If the inversion is significant, the MIL is characterized by its amplitude ($T_{max} - T_{min}$), depth ($z_{max} - z_{min}$), and the temperature lapse rate above (topside) and below (bottom side) the MIL max. The bottom side lapse rate is the negative lapse rate (increasing temperature with height) between the MIL min and MIL max. The topside lapse rate is the steepest 2 km slope fit found in the first 5 km above MIL max. The characteristics of the MIL are found in the data smoothed by 1 km, then reloaded and reported in the unsmoothed data. This method is used to avoid incorrectly reporting the peak altitude of the MIL due to a noisy profile.

Once the MIL is identified as significant in the average temperature profile, the MIL characteristics are calculated in the sequential 2 h temperature profiles. The 2 h temperature profiles are calculated from the 2 h integrated raw photon count profiles, with the first 2 h profile centered on the hour closest to the acquisition time of the first raw photon count profile. The MIL evolution over the observational period is visible in the sequence of 2 h profiles and is used to determine the phase progression. The 2 h MIL characteristics are reported for the profile with maximum amplitude. Note that if an inversion that was insignificant in the average nightly temperature profile is significant (the amplitude is larger than the associated errors) in the 2 h profile, the MIL is characterized and included in the occurrence rate and statistics reported. Therefore, the occurrence rate (number of observations with one or more MIL) is larger for the MILs characterized in the 2 h profiles than those characterized in the average profiles.

Three observations are presented of MILs observed by the NICT Rayleigh lidar at Chatanika. The average nightly temperature profile measured by the NICT Rayleigh lidar on 25–26 January 2003, 27–28 January 2005, and 3 February 2008 are shown in Figure 4.2. On all three nights, the temperature measured by the lidar show disturbed thermal structures that differ from the climatological temperatures reported by the SPARC reference atlas (dotted lines with open circles). The most dramatic departure is

seen on 3 February 2008 when the lidar measures a large inversion, classified as a MIL in this study, above 65 km. These temperature profiles accentuate the variability observed at Chatanika and underscore the challenge of generalizing the characteristics of MILs and the mechanism(s) responsible for their formation at this high latitude site.

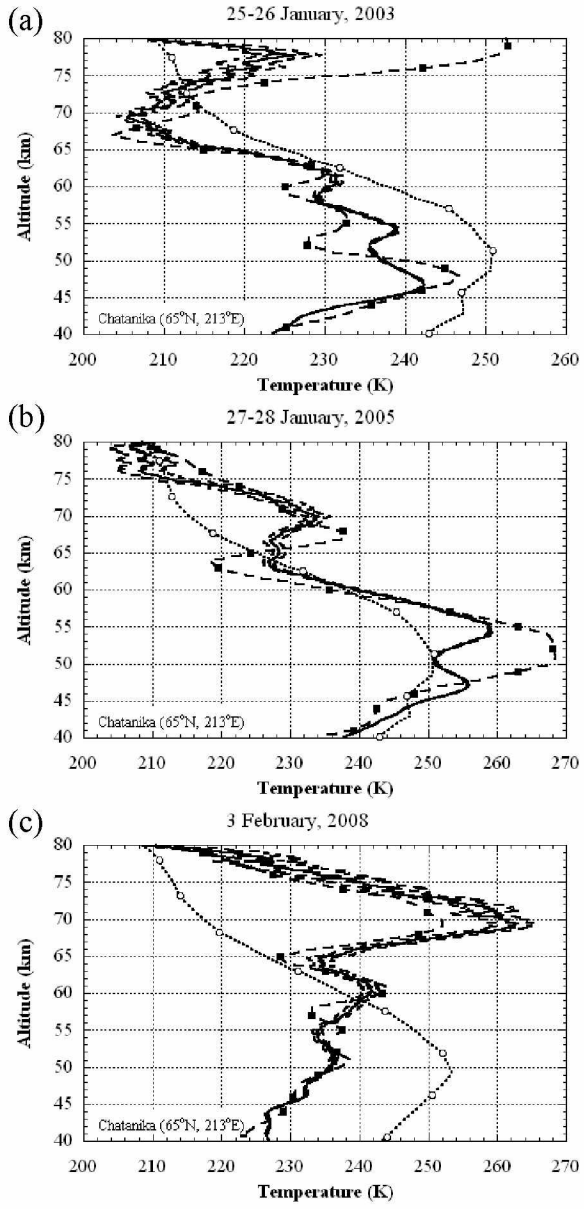

Figure 4.2. (a) Total temperature profiles as a function of altitude measured by the NICT Rayleigh lidar on (a) 25–26 January 2003 LST (b) 27–27 January 2005, and (c) 3 February 2008 (thin solid line). The uncertainty due to the photon counting profile (thin dashed line), SPARC temperatures (dotted line with open circles), and SABER temperature measured on (a) 26 January 2003 UT at 2353 LST (66.5°N, 216.0°E), (b) 28 January 2005 UT at 2307 LST (63.5°N, 223.5°E), and (c) 4 February 2008 at 2132 LST (65.7°N, 212.8°E) (dashed line with solid boxes) are also plotted.

The MIL characteristics measured in the average temperature profiles (Figure 4.2) are tabulated in Table 4.1. A large amplitude MIL is seen above 70 km in Figure 4.2a from approximately 70–78 km. Although MILs with a peak altitude above 70 km have been characterized at Chatanika, they are excluded from the statistics reported in this study due to the nature of the temperature estimate at 80 km. However, it should be noted that MILs, similar to the one seen above 70 km on 25–26 January 2003, are a persistent feature in the mesosphere temperature structure over Chatanika. The inversion in the SABER temperature, measured on a single orbit near local midnight, reaches a maximum temperature of 252 K at 78 km (Figure 4.2a). The temperature measured by the lidar at 78 km is ~26 K colder than SABER, illustrating the limitations of MILs measured and characterized in the lidar temperature profiles above 70 km.

The average temperature profile measured from 2155–0807 LST on 25–26 January 2003 (Figure 4.2a) shows the stratopause at 46.8 km with a temperature of 242.3 K. The stratopause was determined to be at this altitude because it stayed relatively constant throughout the night, apparent in the sequential 2 h temperatures in Figure 4.3. Two MILs are observed between the stratopause and 70 km, with peak altitudes of 54.1 km and 60.7 km. The SABER temperature measured during a single orbit at 2353 LST shows the same disturbed structure, with a warmer more robust stratopause, and a much larger amplitude MIL above 70 km. Differences between the SABER temperature profile and lidar average profile (Figure 4.2) are due to the lidar temperature retrieval method, which forces the temperature at 80 km to a climatological value, and averaging over the lidar temperature whole observations period, which washes out small scale variability.

On 27–28 January 2005, the lidar operated for 13.0 h from 1945–0846 LST and measured a stratopause at 46.8 km with a temperature of 242.3 K. On 3 February 2008 the lidar operated for 4.2 h from 1801–2211 LST with no clear stratopause identifiable in the nightly average temperature profile. A temperature inversion is seen to peak just below 70 km in Figure 4.2c and is the largest amplitude MIL measured by the lidar at Chatanika. It is important to note that the 2007 – 2008 winter was characterized by four

pulses of warming events on 23 January, 4, 15, and 22 February 2008 [Thurairajah, 2010b]. Thus, the feature defined to be a MIL in this study, observed on 3 February 2008, may be related to an elevated stratopause event.

Table 4.1. Characteristics of MILs reported in the average temperature profile.

Date	Altitude Range (km)	Amplitude (K)	Depth (km)	Topside Lapse Rate (-K/km)	Bottom Gradient (K/km)
25–26 Jan 2003	51.9-54.1	3.3 ± 0.5	2.25	3.13 ± 0.07	1.81 ± 0.05
	58.6-60.7	2.2 ± 0.8	2.10	5.44 ± 0.15	1.36 ± 0.05
	69.5-77.8	19.6 ± 3.5	8.32	10.35 ± 0.38	2.19 ± 0.05
27–28 Jan 2005	66.5-69.8	6.8 ± 1.9	3.30	6.61 ± 0.20	2.35 ± 0.08
3 Feb 2008	64.4-69.3	27.7 ± 3.2	4.88	7.04 ± 0.37	6.58 ± 0.11

The detection metric used in this study is different than Cutler et al. [2001] who used the total error in the temperature measurement (due to photon counting and initial temperature). The current study allows for the detection of smaller MILs than reported by Cutler and co-workers. Hauchecorne and co-workers also limited their study to large amplitude MILs (i.e. greater than 10 K) [e.g., Hauchecorne et al., 1987].

4.2.2. TIMED–SABER instrument

The Sounding of the Atmosphere using Broadband Emission Radiometry (SABER) is one of four instruments aboard the Thermosphere-Ionosphere-Mesosphere Energetics and Dynamics (TIMED) satellite launched on 7 December 2001. SABER uses the technique of limb-infrared radiometry and is capable of continuously sounding the atmosphere both day and night. The SABER instrument scans the horizon, observing limb emission in 10 broadband spectral channels ranging from 1.27 to 17 μm [Russell et al., 1999]. The SABER instrument description and temperature data product derivations are presented in Appendix B.

The TIMED satellite's orbit provides constant latitudinal coverage from 52°N to 52°S and latitudes poleward of 52° are viewed in approximately 60 day cycles. Thus, SABER data at Chatanika (65°N, 213°E) is only available for the periods of mid-September through mid-November, mid-January through mid-March, and mid-May through mid-July, when the satellite is viewing the Northern Hemisphere. The lidar at Chatanika operates August – May and observations are highly weather dependent. There are a total 74 nights of observations for the mid-January through mid-March 2002 – 2005, 2008 and 2009 seasons and mid-September through mid-November 2002, 2003, and 2008 seasons when SABER and the lidar at Chatanika were making simultaneous measurements. The fall season accounts for only 10 of the 74 total nights.

This study uses SABER Level 2A (version 1.07) temperature and geopotential height data from 2002 – 2005 and 2008 – 2009 available at 65°N. The SABER instrument does not directly measure geopotential. However, it has been shown that SABER data is suitable for quantitative studies of the large-scale geopotential height variability in the middle atmosphere [Remsberg et al., 2003]. SABER has a native vertical resolution of approximately 2 km [Mertens et al., 2004] and is interpolated to 1 km resolution in this study. García-Comas et al. [2008] report errors of ±1–2 K below 95 km and ±4 K at 100 km for temperature retrievals using a non-LTE algorithm. García-Comas and co-workers note that errors increase when there is significant vertical structure in the temperature profile, such as a strong inversion layer (see Appendix B for further discussion).

4.3. MILs at Chatanika

There are few high latitude lidar studies of MILs reported compared to middle and low latitudes [see review by Meriwether and Gerrard, 2004]. High latitude MILs seen by lidar are found to have a lower occurrence rate than midlatitudes [Cutler et al., 2001; Duck and Greene, 2004]. Duck and Greene [2004] reported MILs with an occurrence rate of 5% observed at a high latitude site (80°N, 86°W) from 1993 through 1998, a period when no stratospheric sudden warmings were reported [Manney et al., 2005]. The previous study of MILs at Chatanika [Cutler et al., 2001] reported a MIL occurrence rate

of 19% from 1997 through 2000, with the highest hourly occurrence in November (50%), and no MILs reported from December through February. As mentioned previously, the detection criteria employed by Cutler et al. considered the accuracy in the absolute value of the temperatures (i.e. error due to the uncertainty in the initial temperature estimate and statistical uncertainty due to photon counting). This analysis considers only the statistical uncertainty in the raw lidar data which gives the relative accuracy of the temperature in a given profile.

The average nightly temperature profiles measured by the NICT Rayleigh lidar have been examined for the occurrence of MILs from November 1997 through April 2005 and November 2007 through March 2009. The average daily occurrence rate of 37% is determined by the number of average nighttime temperature profiles with one or more MILs (55) divided by the total number of average nighttime temperature profiles (149) measured by the NICT Rayleigh lidar at Chatanika from November 1997 – March 2009. The daily occurrence rate increases to 47% (70 out of 149) when considering the number of MILs in the 2 h temperature profile where the amplitude is largest and the peak altitude is below 70 km. The use of an initial temperature at 80 km restricts the MIL characteristic statistics reported in this thesis to those MILs with a peak altitude below 70 km in the average profile (consistent with Duck and Greene [2004]). The average daily occurrence (one or more MILs in the average profile) increases to 89 out of the 149 nightly average profiles when considering MILs that extend up to 80 km. When a stratopause was identifiable (i.e. there is no elevated stratopause event or significantly disturbed behavior), the stratopause had a mean altitude of 49.3 km and a mean temperature of 250 K in the average temperature profile. The stratopause mean altitude and temperature fall within the stratopause monthly mean values reported by Thurairajah et al. [2009]. Thurairajah and co-workers reported the stratopause monthly mean altitude varied between 47.5 km and 54.7 km, with monthly mean temperatures varying between 243 K and 273 K measured by the NICT Rayleigh lidar over an 8-year period from 1997 through 2005.

The sequential 2 h temperature profiles (separated by 25 K) are shown in Figure 4.3 for 25–26 January 2003, 27–28 January 2005, and 3 February 2008. The last profile in the sequence is generally noisier than the preceding profiles due to the method used in calculating the 2 h profiles. Observations on 3 February 2008 were made over 4.2 h, resulting in the first and last 2 h profiles being noisy. The characteristics of the inversions seen in the 2 h temperature profiles are given in Table 4.2. The MIL duration is determined as the number of 2 h profiles after the MIL is first identified as significant to the last 2 h profile, multiplied by 2 h. For example, on 3 February 2008 the duration of the MIL is reported as 6 h because it was a significant feature in the three 2 h temperature profiles. However, the duration of the observations was less than 6 h, so the MIL duration is reported but may not accurately reflect the true lifetime of the inversion. As mentioned above, MILs that were not significant in the average temperature profile may be characterized in the 2 h profiles if their amplitudes become larger than the associated errors. Such is the case on 25–26 January 2003 when a statistically significant MIL appears in the third profile just below 70 km but is not significant in the average temperature profile. The average MIL characteristics reported in the average profile and 2 h profile are given in Table 4.3 with uncertainties taken as the standard deviation of the measurements.

The characteristics of MILs identified in average and 2 hour observations at Chatanika over a 12-year period from 1997 through 2009 are presented in Figure 4.4. The analysis of the 2 h temperature profiles highlights features that are not evident in the nightly average profiles. The altitude distribution of MILs appears to be bi-modal with MILs occuring in the lower mesosphere (~55 km) and upper mesosphere (65 km and above). The MIL amplitudes are generally 5–10 K, with depths of 2–3 km, topside lapse rates of 6–8 K km^{-1} and bottomside gradients of 2–4 K km^{-1}. The average characteristics are tabulated in Table 4.3.

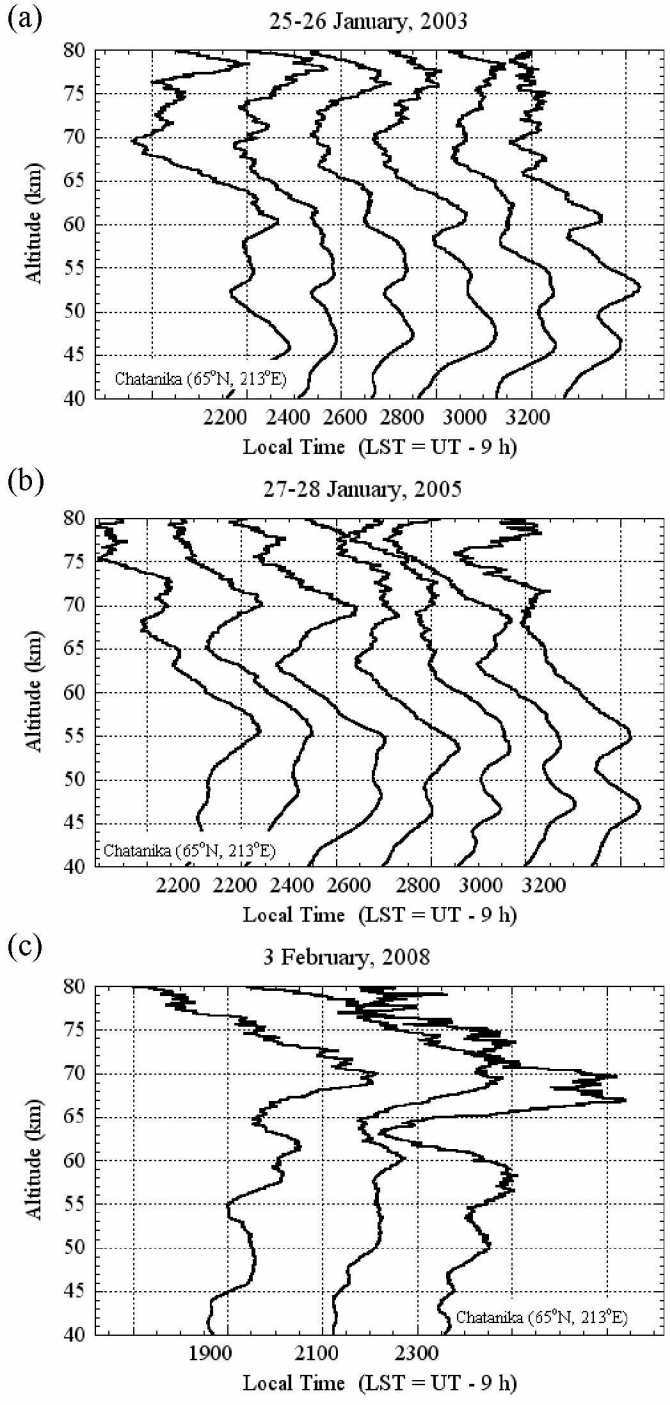

Figure 4.3. Sequential 2 h temperature profiles on (a) 25–26 January 2003, (b) 27–28 January 2005, and (c) 3 February 2008. Successive profiles are separated by 25 K.

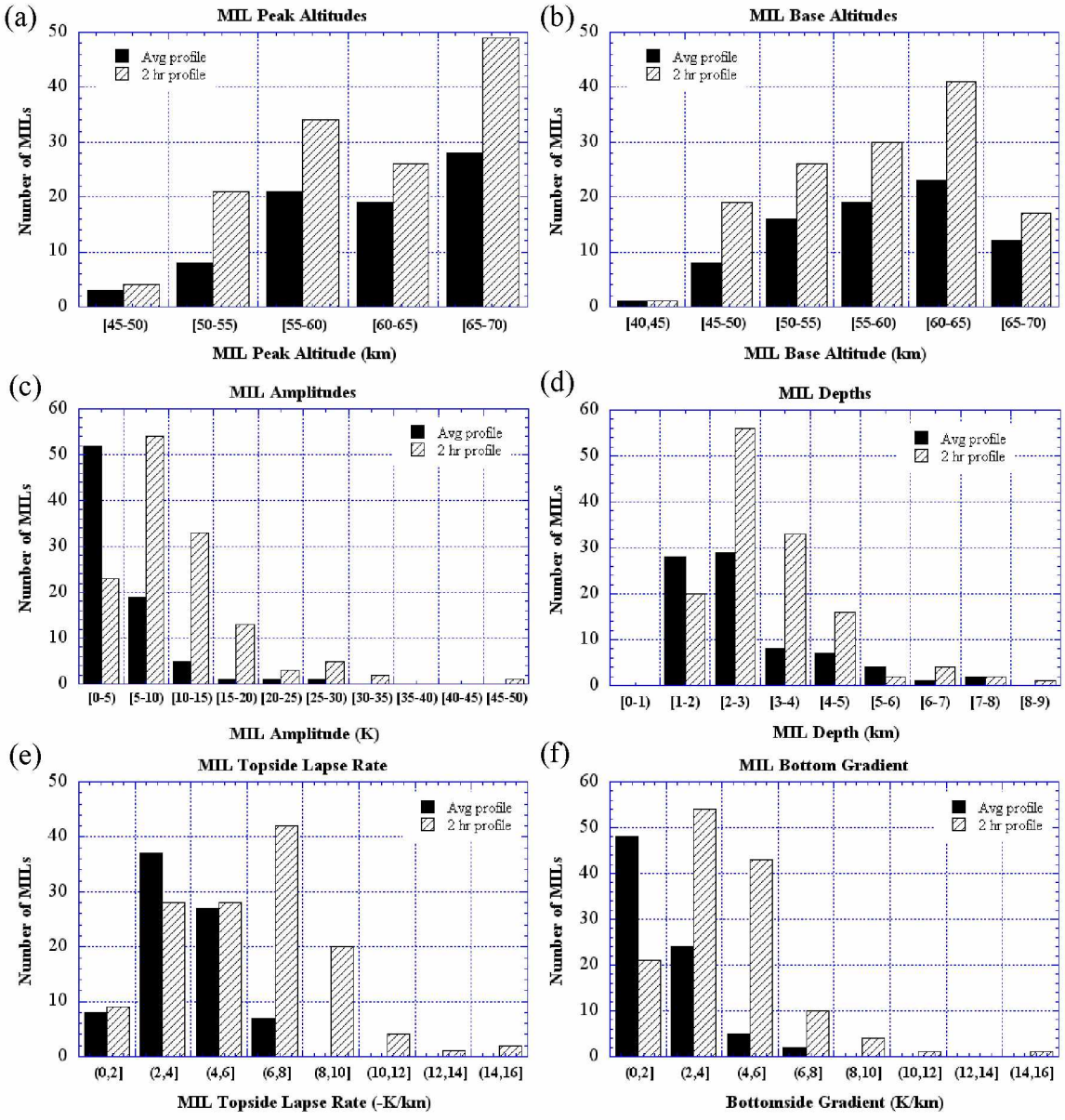

Figure 4.4. Characteristics of MILs identified in the average and 2 h temperature profiles measured by the NICT Rayleigh lidar at Chatanika. Shown are (a) peak altitude in km, (b) base altitude in km, (c) amplitude in K, (d) depth in km, (e) topside lapse rate in K km^{-1}, and (f) temperature gradient below the MIL in K km^{-1}, in the average temperature profile (79 MILs, solid bars) and 2 h profile (134 MILs, dashed bars).

Table 4.2. Characteristics of MILs reported in the 2 h temperature profile where the amplitude is largest.

Date	Altitude Range (km)	Amplitude (K)	Depth (km)	Duration (h)	Topside Lapse Rate (-K/km)	Bottom Gradient (K/km)	Phase progression (km/h)
25–26 Jan 2003	49.5-52.8	14.5 ± 1.2	3.30	12	6.01 ± 0.12	5.25 ± 0.12	-0.23 ± 0.62
	57.7-60.3	11.3 ± 2.5	2.63	12	8.29 ± 0.33	5.13 ± 0.14	0.03 ± 0.99
	65.9-67.6	6.6 ± 4.5	1.73	8	6.86 ± 0.27	4.54 ± 0.30	-0.06 ± 0.98
	73.6-77.9	28.4 ± 9.5	4.35	10	30.30 ± 3.05	5.83 ± 0.21	-0.10 ± 0.91
27–28 Jan 2005	63.0-69.4	29.8 ± 4.1	6.38	12	8.12 ± 0.37	4.59 ± 0.14	-0.26 ± 1.01
3 Feb 2008	63.2-67.1	49.0 ± 1.3	3.90	6	14.22 ± 0.93	15.2 ± 0.47	-0.62 ± 0.41

Table 4.3. Average MIL characteristics[1] for all MILs at Chatanika, AK.

	Average Profile	2 Hour Profile
Number of MILs	79	134
Number of days	55	70
Peak Altitude (km)	61.3	61.0
Base Altitude (km)	58.6	58.0
Amplitude (K)	4.8 ± 0.8	10.6 ± 7.2
Depth (km)	2.7	3.1
Topside Lapse Rate (-K/km)	3.8 ± 1.5	5.9 ± 2.7
Bottom Gradient (K/km)	1.9 ± 1.3	4.0 ± 2.2
Duration (h)	-	7
Phase progression (km/h)[2]	-	-0.2 ± 0.5

1: Restricted to maximum altitudes ≤ 70.0 km

2: 129 MILs had a reported phase progression

The phase progression was calculated when the MIL was identified as significant in more than one 2 h profile. The phase progressions were calculated in 129 of the 134 MILs identified in the 2 h profiles. MILs were found to have a downward phase progression

(i.e. less than 0 km h^{-1}) in 88 of the 129 MILs and the average vertical phase progression in the 129 MILs was -0.2 km h^{-1}. Figure 4.5 shows a histogram of the phase progressions from the 129 MILs identified in the 2 h temperature profiles.

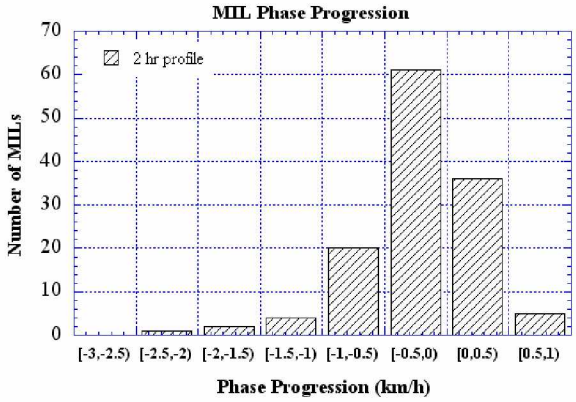

Figure 4.5. MIL phase progression calculated for MILs identified as significant in two or more 2 h temperature profiles.

The detection metric used in this study excluded only MILs with an amplitude less than the associated statistical photon counting errors (i.e. not statistically significant). The goal of the detection scheme employed was to characterize MILs generated by different processes and allow for the identification of small scale and short lived (2 – 4 h) MILs, as well as persistent MILs that were observed over multiple nights. For example, the mechanism responsible for the generation of MILs with a topside lapse rate approaching the adiabatic lapse (e.g., breaking gravity waves) may be different than the large amplitude MILs that persist over multiple days (e.g., breaking planetary waves).

Past studies have limited their analyses of MILs by defining criteria that includes only MILs with an amplitude of 10 K [Hauchecorne et al., 1987; Das and Pan, 2011] or 12 K [Leblanc and Hauchecore, 1997; Gan et al., 2012]. Duck and Greene [2004] reported only those MILs with a depth of 2.4 km or greater, amplitudes larger than two standard errors, and topside lapse rates in excess of –8.0 K km^{-1}. Sica et al. [2007] limited their analysis to measurements with SNR greater than 4.5 and inversions with amplitudes greater than 1 K. In an effort to compare the MIL occurrence seen at Chatanika to those

previously reported, Table 4.4 presents the characteristics of MILs with a peak altitude below 70 km and an amplitude of 10.0 K or greater. Using this criterion, the daily occurrence rate (number of days with one or more MILs in the temperature profile divided by total number of NICT Rayleigh lidar observations) is reduced to 5% in the average profiles and 28% in the 2 h profiles.

Table 4.4. Average MIL characteristics[1] of large amplitude MILs at Chatanika, AK

	Average Profile	2 Hour Profile
Number of MILs	8	57
Number of days	8	41
Peak Altitude (km)	61.6	62.1
Base Altitude (km)	56.7	58.3
Amplitude (K)	15.6 ± 1.2	16.5 ± 7.3
Depth (km)	4.9	3.8
Topside Lapse Rate (-K/km)	4.2 ± 1.5	7.0 ± 2.7
Bottom Gradient (K/km)	4.1 ± 1.9	5.4 ± 2.4
Duration (h)	-	8
Phase progression (km/h)	-	-0.2 ± 0.4

1: Restricted to maximum altitude ≤ 70.0 km and amplitude ≥ 10 K

If the detection criterion is restricted to include only MILs with a peak altitude below 70 km and a topside lapse rate in excess of -8.0 K km^{-1}, 27 MILs in 23 days are found in the 2 h temperature profiles and no MILs were found in the average temperature profile. The 27 MILs in the 2 h temperature profiles had a mean base and peak altitude of 60.7 km and 64.1 km, respectively, mean amplitude of 15.4 ± 9.4 K, mean depth of 3.5 km, mean topside lapse rate of -9.6 ± 1.7 K km^{-1}, and a mean phase progression of -0.3 ± 0.6 km h^{-1}. The uncertainties reported are the standard deviation. The restriction of MILs with a lapse rate approaching the adiabatic lapse (arbitrarily chosen as -8.0 K km^{-1}) results in a daily occurrence rate of 16% in the 2 h profiles (23 days out of 147 total days). This is again larger than the occurrence rate of 5% reported in the High Arctic at Eureka (80°N,

274°E) [Duck and Greene, 2004]. Furthermore, Duck and Greene [2004] restricted their study to MILs with a depth of 2.4 km or larger. Using both the MIL depth and topside lapse rate criteria of Duck and Greene [2004], 22 MILs in 19 days were found in the 2 h temperature profiles between a mean base altitude of 59.8 km and peak altitude of 63.6 km, with a mean amplitude of 17.1 ± 9.5 K, mean depth of 3.8 ± 1.4 km, mean topside lapse rate of -9.6 ± 2.0 K km^{-1}, and mean phase progression of -0.3 ± 0.6 km h^{-1}. This detection criteria results in a daily occurrence rate of 13%, still larger than the 5% reported in the High Arctic at Eureka (80°N, 274°E) [Duck and Greene, 2004].

We find that the vertical phase progression does not change when restricting the analysis of all MILs to large amplitude MILs (> 10 K) and is only slightly steeper for MILs with overlying adiabatic lapse. Gravity waves have typical phase progressions of -0.6 km h^{-1} and below [e.g., Collins and Smith, 2004; Liu and Meriwether, 2004]. The phase progressions observed in MILs at Chatanika are significantly smaller, suggesting that gravity waves are not the primary mechanism responsible for the formation of MILs.

4.4. MILs and their relationship to planetary waves

The planetary wave structure at 65°N is examined in the three observations presented above, as well as over the period of mid-January through mid-March when SABER is viewing the Northern Hemisphere. In this section, the relationship between MILs and planetary waves is introduced and a review of Salby et al. [2002] is presented as an introduction to the behavior expected in the region of breaking planetary waves. In the troposphere, planetary waves are forced by large-scale orographic and thermal contrasts, and can propagate vertically into the stratosphere and mesosphere only in the presence of westerly winds [e.g., Schoeberl and Hartmann, 1991; Holton, 2004]. Wave breaking can occur when background winds approach a critical value equal to the phase velocity of the wave, or when the wave reaches unsustainable amplitude as vertically propagating planetary waves amplify with decreasing density. In the winter mesosphere, a reversal of the zonal mean circulation above 75 km is formed due to deposition of easterly momentum by gravity waves that propagate through the stratosphere. As planetary

waves break in the mesosphere and stratosphere, their amplitudes rapidly decay and their momentum is deposited into the system, and can lead to the formation of large spatiotemporal mesospheric inversion layers [Wu, 2000; Salby et al., 2002].

The planetary wave field is characterized by isobaric geopotential, Φ, which is proportional to a streamfunction. Geopotential is the work required to raise a unit mass to a height z and is given by,

$$\Phi = \int_{z_0}^{z} g dz \tag{4.1}$$

where g is gravity (9.81 m s^{-2}). Under hydrostatic balance (Equation 2.16), and using the ideal gas law (Equation 2.17), geopotential can be rewritten as,

$$\Phi = -\int_{p_0}^{p} \left(\frac{RT}{p}\right) dp \tag{4.2}$$

where R is the universal gas constant (8.314 J K^{-1} mol^{-1}), p is pressure, and T is temperature. Thus, using the atmospheric scale height ($H = RT/g_0$), temperature determines the rate at which geopotential changes with altitude ($\partial\Phi/\partial z = RT/H$). The temperature lapse rate ($\Gamma = -\partial T/\partial z$) is related to geopotential through its vertical curvature [e.g., Salby, 1996; Salby et al., 2002; Holton, 2004],

$$\Gamma = -\frac{H}{R}\frac{\partial^2 \Phi}{\partial z^2} \tag{4.3}$$

Salby et al. [2002] used geopotential (m^2 s^{-2}) and temperature data from the UARS satellite to study the global structure of MILs observed during December 1991 and January 1993 by Rayleigh lidar at Observatoire de Haute-Provence (OHP) in France (44°N, 6°E). Salby and co-workers showed that the wave component (perturbation) of geopotential, taken as the average minus the zonal mean (e.g., $\Phi' = \Phi - \bar{\Phi}$ and $\Gamma' = \Gamma - \bar{\Gamma}$), can generate an inversion when Γ' is sufficiently negative. Likewise, an inversion can form when the vertical curvature of Φ' (or Z') is sufficiently positive, given

by Equation 4.4. This study uses geopotential height perturbation (Z′ in km) and temperature data from SABER. The perturbation in geopotential height describes the same field as wave geopotential (average minus the zonal mean) only scaled by the gravitational constant.

$$\Gamma' = -\frac{H}{Rg_0}\frac{\partial^2 Z'}{\partial z^2} < -\bar{\Gamma} \tag{4.4}$$

The method Salby et al. [2002] used for describing the planetary wave field in the presence of MILs with UARS wave geopotential is presented prior to the observations at Chatanika.

4.4.1. Review of Salby et al. [2002]

Salby et al. [2002] presented MILs observed at OHP on 25 and 26 December 1991, and on 1 and 3 January 1993 (not shown). On 25 December 1991 the MIL had a depth of 6 km (66–72 km), amplitude of ~25 K, a lapse rate of –5 K km^{-1}, and was capped overhead by an isothermal layer extending upwards of 5 km. On the next day, the inversion narrowed to 4 km (67–71 km), 20 K, and steepened above the inversion to –10 K km^{-1}. The MIL was part of a large scale temperature anomaly in the upper mesosphere measured by UARS, shown as shaded contours in Figure 4.6. Temperature and wave geopotential as cross section of longitude and height observed by UARS on 25 December 1991 is shown in Figure 4.6a and Figure 4.6b, respectively.

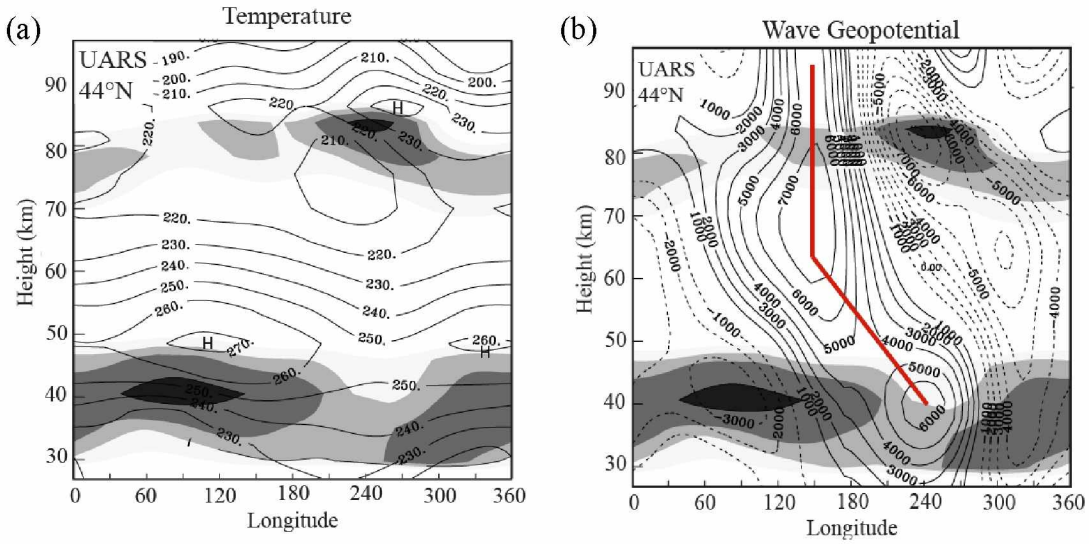

Figure 4.6. (a) Temperature (K) and (b) wave geopotential (m^2 s^{-2}) at 44°N, as a cross section of longitude and height, observed by UARS on 25 December 1991. Superposed are regions of negative lapse rate (shaded). Highlighting the phase tilt with height is a solid red line (adapted from Salby et al. [2002]).

In Figure 4.6, the negative lapse rate (shaded contours) below 50 km shows the stratopause, variable with height around the globe. The negative lapse rate is strongest and highest in the Eastern Hemisphere just west of the temperature maximum at ~120°E and 50 km and is weakest from approximately 200°E to 250°E. In the mesosphere, an isothermal layer extending ~15 km deep is noticeable from ~90°E to 270°E. In the Western Hemisphere mesosphere, the minimum temperature at 72 km is capped overhead by an inversion to the east. The strongest and highest negative lapse rate is observed between the temperature minimum and maximum, coincident with an abrupt shift of wave temperature T′.

Figure 4.6b shows wave geopotential Φ′ as a cross section of longitude and height on 25 December 1991. Φ′ slopes westward and amplifies with height through the stratosphere and mesosphere, consistent with vertical propagation of planetary waves. The amplitude maximizes in the mesosphere, above which phase contours are nearly vertical,

corresponding to barotropic structure. This behavior is most evident from 90°E to 270°E where Φ' is large and positive, and coincides with the isothermal layer. The inversion is steepest in and slightly above the negative maximum of Φ', at approximately 85 km and 240°E. Above the region of negative maximum in Φ', sharp decay in wave amplitudes and strong positive vertical curvature generate an inversion through hydrostatic balance. Above the inversion, the vertical phase tilt relaxes rapidly and is replaced by nearly barotropic structure, corresponding to strong absorption of planetary waves. The inversion is weaker at other longitudes but follows the region of maximum positive vertical curvature in Φ' and maximum amplitude in Φ', capping the westward tilt.

The inversion measured by the OHP lidar is part of a mesospheric temperature anomaly that spans much of the globe. Where the inversion is positioned above the positive maximum of Φ' (just west of 180°) is described as a region where planetary wave structure becomes external. Here, wave energy decays upward with little or no phase tilt and then assumes positive curvature overhead. At intermediate longitudes the inversion is found at lower altitudes, coinciding with maximum vertical curvature as Φ' transitions from negative to positive. Salby and co-workers concluded that MILs that extend over large horizontal dimensions and timescales are closely related to planetary wave structure. Distortions in the circulation related to planetary waves are shown to produce thermal inversions. Even if the lapse rate is not fully reversed, the strengthened stability can support the production of isolated inversions by gravity waves or tides. The authors note that individual UARS soundings include variability not seen on the global scale, attributed as a possible a signature of gravity waves.

4.4.2. SABER observations at 65°N

The MILs observed by the lidar when SABER is viewing 65°N have similar characteristics compared to the whole Chatanika lidar data set. SABER geopotential height perturbation, geopotential planetary wave amplitude for zonal wave number one (wave-one) and for zonal wave number two (wave-two), and Eliassen-Palm (EP) flux divergence data are used to study the relationship between MILs and planetary wave

structure. Negative EP flux divergence corresponds to the westward zonal force exerted by eddies on the atmosphere. Explanation of the EP flux calculation using SABER data can be found in Thurairajah [2009]. The temperature (left panel) and geopotential height perturbation (right panel) are presented in Figure 4.7 for the UT days corresponding to lidar observations on 25–26 January 2003, 27–28 January 2005, and 3 February 2008 at Chatanika.

Figure 4.7a shows lined contours of the SABER average temperature field on 26 January 2003 UT as a function of longitude and height at 65°N. Regions of negative lapse rate are shaded contours. In the Western Hemisphere, temperatures are very disturbed and inversions appear at intermittent altitudes extending up through the stratosphere and mesosphere. The strongest inversion in the mesosphere extends from approximately 90°E at 13 scaled heights (SH) to approximately 250°E at 11 SH. The SABER geopotential height perturbation Z' observed on 26 January 2003 UT (Figure 4.7b) exhibits significant westward tilt below ~11 SH. Amplitude maximizes at approximately 6 SH and 11 SH in the Western Hemisphere with weaker amplitudes maximizing below 6 SH in the Eastern Hemisphere. The highly disturbed temperature structure in Figure 4.7a is located in the negative phase of Z' and the intermittent inversions are associated with regions of the negative maximum in Z'. The strong inversion in the upper mesosphere is just above the negative maximum in Z' at 11 SH, and positioned slightly west of Chatanika. Above the negative maximum in Z', the westward tilt weakens and is replaced with barotropic structure over Chatanika.

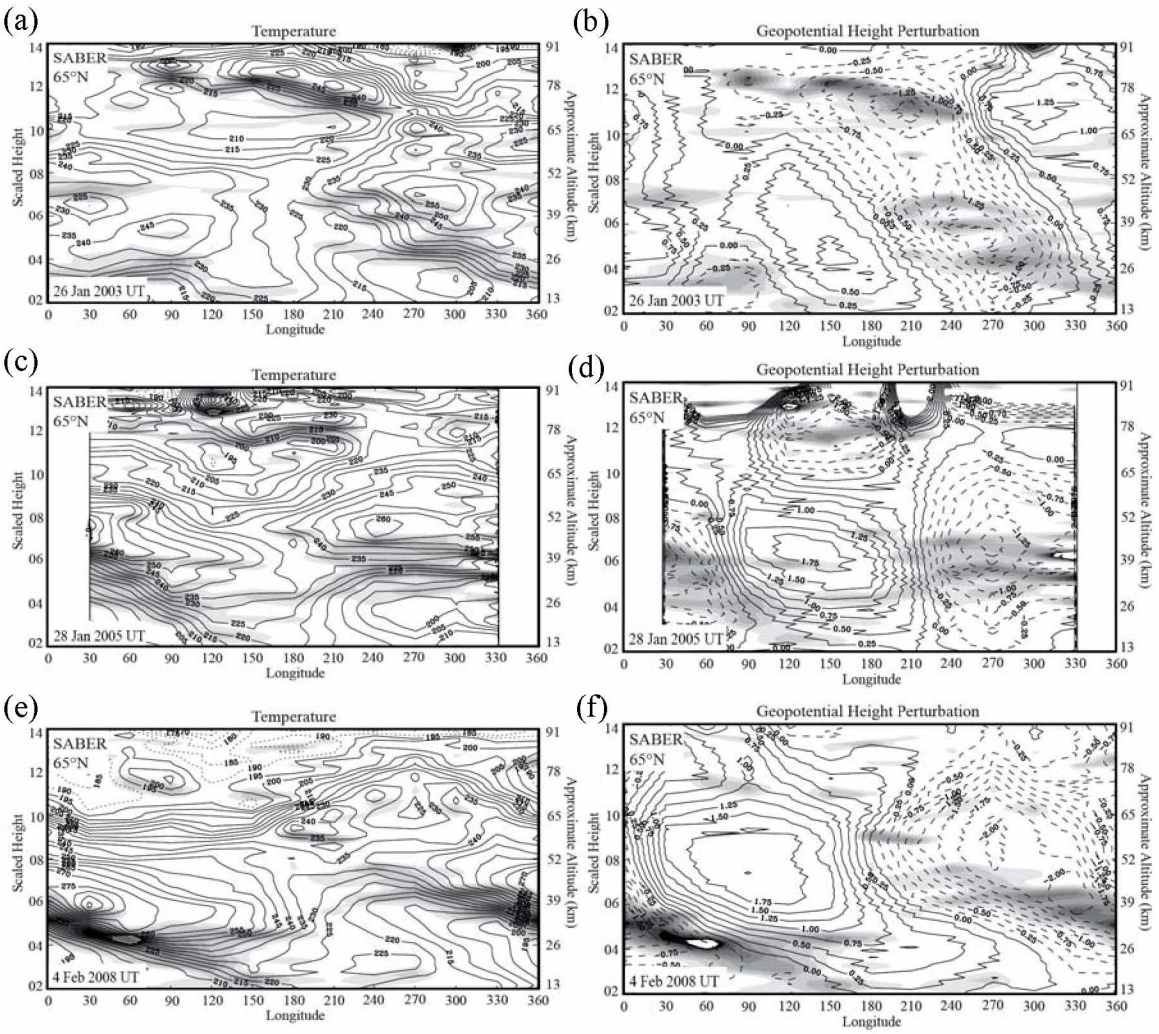

Figure 4.7. (Left) Average temperature (K) and (right) geopotential height perturbation (km) at 65°N as a cross section of longitude and altitude observed by SABER on 26 January 2003 (top), 28 January 2005 (middle) and 4 February 2008 UT (bottom). Shaded contours are regions of negative lapse rate from 1 to 10 K km^{-1}, with an interval of 1 K km^{-1}, and a scale height of 6.5 km is used to approximate altitude.

On 28 January 2005 UT (Figure 4.7c and d), data is not available at longitudes west of 30°E and east of 330°E and is noisy above approximately 12 SH. The SABER temperature field in Figure 4.7c shows the stratopause from 6 to 8 SH with the highest temperatures at ~30°E and 250°E and the coldest temperature over 180°E. The region of

strongest and steepest inversions below the stratopause is coincident with the negative phase in Z′. There is clear westward tilt in the Eastern Hemisphere, with the negative phase of the wave dominating the Western Hemisphere. East of 210°, Z′ does not appear to be westward tilting. However, the external structure in the western mesosphere points to a westward tilting wave that has undergone strong absorption [Salby et al., 2002]. The inversion measured by the lidar over Chatanika on 27–28 January 2005 LST is not resolved in the global SABER field with the interval presented. However, the SABER temperature in a single orbit measured near Chatanika does show a strong inversion (Figure 4.2) and if the lapse rate interval is extended to include those from 0 K km^{-1}, the inversion does appear as a robust feature at 10 SH (not shown).

On 4 February 2008 UT (Figure 4.7e and f), temperatures in the Eastern Hemisphere exhibit very stratified structure with temperatures falling below 180 K in the mesosphere. A local inversion interrupts the positive lapse rate from ~40° to 120°E. The stratopause reaches a maximum temperature of ~290 K at 6 SH and 30°E and then descends in height to ~5 SH over 180°E. The temperature field in the Western Hemisphere is more disturbed, with very wavy contours and local temperature maxima throughout the mesosphere. The stratopause appears to tilt westward with height from 360°E, with no clear stratopause structure over Chatanika. This supports our assumption that the large amplitude MIL seen at 70 km in the lidar profile is not an elevated stratopause event, but rather a strong local temperature maximum. In Figure 4.7f, the Western Hemisphere is again dominated by negative Z′, with a maximum at 6 SH over 330°E and a second maximum at 9 SH over 270°E. Above approximately 9 SH, amplitude sharply decays and westward tilt disappears. Inversions are found at and just above the level of maximum wave amplitude, where sharp decay above produces strong vertical curvature in Z′. The inversion is found just below 10 SH from ~160° to 240°E and coincides with a change in phase from negative to positive Z′, consistent with Salby et al. [2002].

Planetary wave-one and wave-two geopotential amplitudes (Figure 4.8) and EP flux divergence (Figure 4.9) is presented for the period of mid-January through mid-March in

2003, 2005 and 2008. If MILs are indeed related to planetary wave activity, we expect their presence to coincide with periods of large planetary wave geopotential amplitudes and negative EP flux divergence. In general, SABER is able to resolve the inversions seen in the lidar temperature profiles (Figure 4.2) and confirms that inverted thermal structures seen above 70 km by the lidar represent true features. Therefore, inversions seen above 70 km by the lidar are included in the discussion of MILs and their relationship to the synoptic planetary wave field and are included in Figure 4.8 and Figure 4.9.

Figure 4.8 shows the planetary wave-one and wave-two geopotential amplitudes at 65°N over the ~60 day window in early spring 2003, 2005 and 2008 when SABER data is available. Vertical lines indicate days when the lidar was taking measurements at Chatanika and the red boxes denote the approximate altitude (using a 6.5 km scale height) of MILs characterized in the lidar profile. No distinction is made between MILs with peak altitudes above or below 70 km. MILs were observed on 12 of the 15 occasions when lidar measurements at Chatanika and SABER measurements coincided in 2003, in 5 of the 9 occasions in 2005, and in 4 of the 9 occasions in 2008. Lidar observations made at Chatanika depend on local weather conditions (and the academic calendar), and thus are not distributed uniformly throughout the season. The availability of lidar measurements makes it difficult to determine an absolute relationship between the occurrence of MILs and planetary wave geopotential amplitudes.

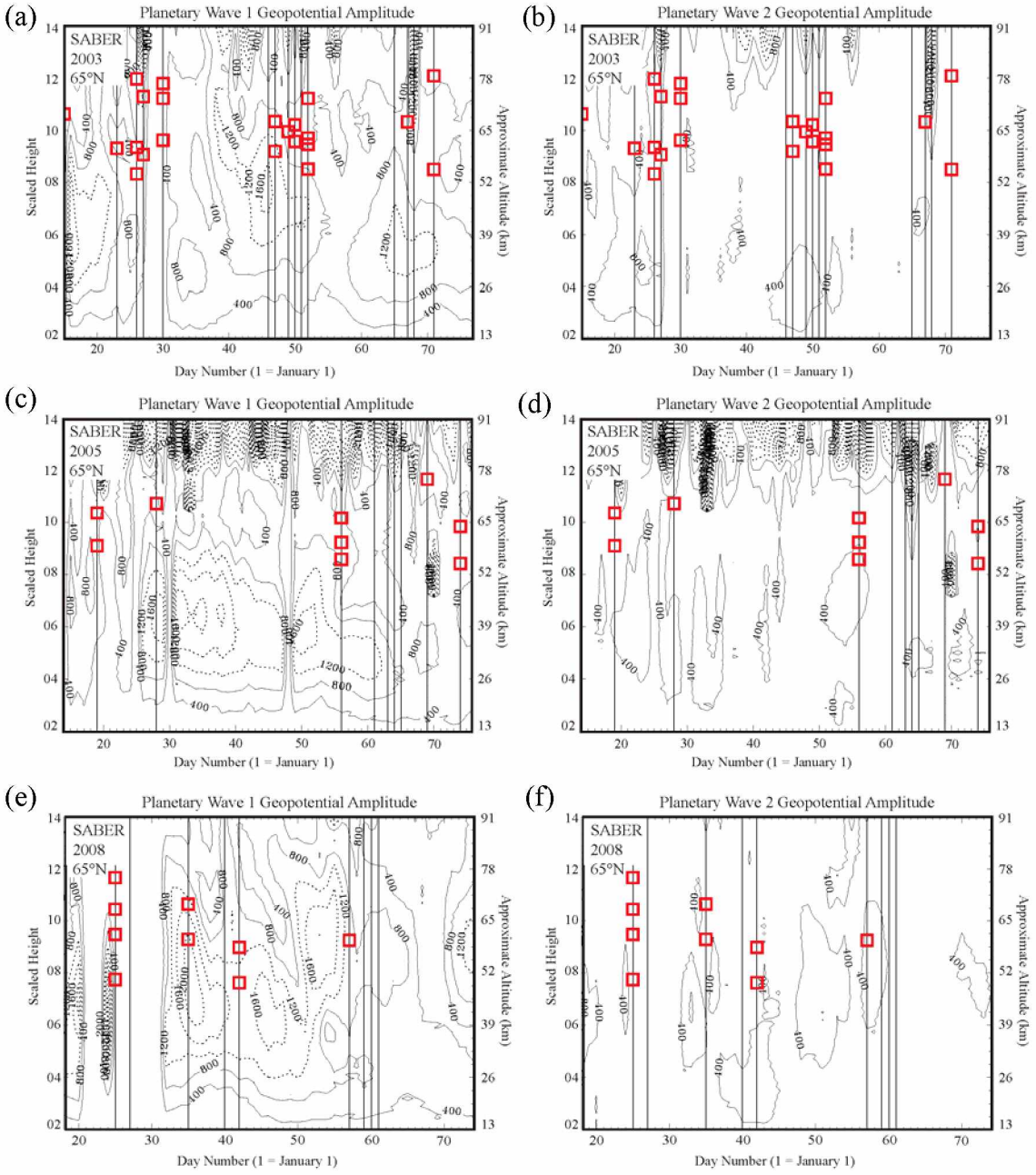

Figure 4.8. SABER planetary wave-one (left) and wave-two (right) geopotential amplitudes at 65°N. Geopotential amplitudes greater than 1000 m are dotted and the contour interval is 400 m. Vertical lines show days when lidar data available and red boxes indicate a MIL in the lidar temperature profile.

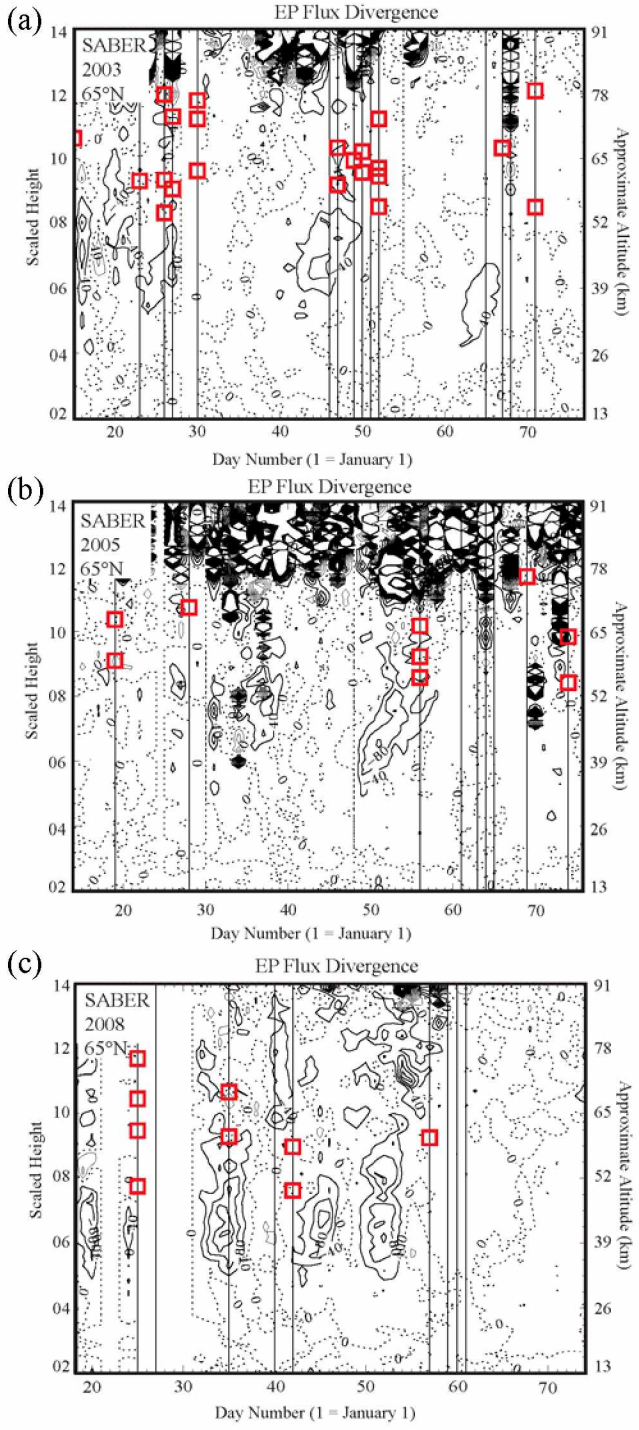

Figure 4.9. SABER EP flux divergence at 65°N. Negative EP flux divergence is solid lines with a contour interval of 40 $ms^{-1}day^{-1}$. Lines are the same as in Figure 4.8.

Figure 4.8a shows the planetary wave-one geopotential amplitude at 65°N as a function of day number from 14 January to 18 March 2003 UT. MILs were seen often during this window and appear after a period of strong wave-one amplification, seen from 6 to 8 SH in mid-January 2003 with wave-two amplitudes also amplifying. On day 30, SABER data is unavailable but 29–30 January lidar observations at Chatanika are still included in this analysis. In early February, wave-one geopotential amplitudes reach 1200 m at 10 SH and 1600 m at 8 SH several days later. Wave-two amplitudes increased to 400 m during this period. During this period, the lidar took data and MILs were seen in every temperature profile except on day 46, corresponding to measurements taken on 14–15 February 2003 at Chatanika. On 14–15 February 2003 (not shown), the stratopause was not visible in the lidar and temperatures were near isothermal. Observations in early March coincided with large wave-one and wave-two geopotential amplitudes. On 5–6 March (UT day 65), no MIL is characterized in the lidar temperature profile (not shown), although inverted thermal structure is evident in the top altitudes. The lidar temperature profile observed on 8–9 March (UT day 68, not shown) showed an elevated stratopause. The scarcity of lidar observations complicate the task of generalizing the relationship of MILs observed by the lidar at Chatanika to the SABER planetary wave field and is further complicated by the high level of variability seen in the lidar temperature profiles.

The planetary wave-one and wave-two geopotential amplitude structure at 65°N in 2005 highlights the year to year variability in the Western Arctic. The geopotential amplitude structure is different than that observed in 2003, with high wave activity from mid-January through early March. The 2005 season is dominated by planetary wave-one structures, with geopotential amplitudes reaching 1600 m in late January and lasting through March. No stratospheric warming events were recorded during the 2004 – 2005 winter over Chatanika [e.g., Thurairajah, 2009; Thurairajah et al., 2010a].

January and February 2008 marked a period of strong planetary wave activity over Chatanika, during which four stratospheric warming events were recorded [Thurairajah et al., 2010b]. The MIL observed on 3 February is coincident with large planetary wave-

one and wave-two amplification where wave-one and wave-two amplitudes increase to 2000 m, and 400 m on 4 February UT, respectively. In the mid-January through mid-March periods considered above, planetary wave-one amplitudes dominate the middle atmosphere at 65°N. Consistent with previous studies [e.g., Oberheide et al., 2006], the Western Arctic appears to be dominated by the quasistationary planetary wave-one wave.

Regions of planetary wave breaking are also examined during these three seasons. Figure 4.9 presents SABER EP flux divergence at 65°N as a function of day number over the ~60 day window in early spring 2003, 2005 and 2008 when SABER data is available. Negative EP flux divergence values are solid lines and positive values are dashed lines, with a contour interval of 40 m s^{-1} day^{-1}. In 2003, 2005, and 2008, there is enhanced wave breaking associated with the periods of geopotential wave-one and wave-two amplification. In 2005 (Figure 4.9b), no MILs are characterized at Chatanika in four consecutive observations from UT day 61 through UT day 65. These days correspond to positive EP flux divergence, supporting the proposed mechanism of wave breaking (negative EP flux divergence values) as being partially responsible for the formation of MILs.

4.5. Discussion

The MILs observed with the NICT Rayleigh lidar on 25–26 January 2003, 27–28 January 2005, and 3 February 2008 are closely related to the planetary wave activity, with synoptic structures similar to those described by Salby et al. [2002]. The MILs are found above regions of enhanced wave dissipation, seen in the negative EP flux divergence in Figure 4.9. These days correspond to periods when major stratospheric warming events were observed at Chatanika [Thurairajah, 2009]. Inverted thermal structure observed by SABER reaches its maximum in the negative phase of geopotential height perturbation, consistent with hydrostatic balance. The results show a strong relationship between planetary wave structure and MILs observed by lidar at Chatanika. 70% of the MILs observed by the lidar at Chatanika when SABER data was available were found to be located in a region of negative geopotential height perturbation, Z'. Similarly, 60% of the

MILs were found within positive curvature of the geopotential height perturbation field. This is compelling evidence that MILs observed by lidar at Chatanika are strongly related to planetary wave structure.

However, MILs also occur outside regions of negative maximum in Z', suggesting other process may be responsible for the generation of MILs at Chatanika. Lidar observations of MILs at Chatanika are not always associated with regions of planetary wave breaking, consistent with Sica et al. [2007]. Sica et al. [2007] gave a simple theory for the formation of MILs due to wave saturation in the mesosphere. Using the Canadian Middle Atmosphere Model (CMAM) with orographic gravity wave drag, they found that for an inversion to form, the environmental lapse rate must be less than half the adiabatic lapse rate. If this condition is not met, then a saturated wave does not lead to an inversion. The authors note that planetary wave breaking in the region of the mesospheric surf zone [e.g., Sassi et al., 2002] is not a necessary condition for the formation of mesospheric inversions, since their model does not have a zonal wind reversal.

From Figure 4.9, periods of enhanced wave breaking appear to precede the occurrence of MILs in the lidar temperature profile. The turbulence generated by wave breaking can condition the atmosphere for further disruption and absorption of waves. Although this study does not quantitatively determine the relationship of wave breaking to the formation of MILs, the behavior presents an intriguing idea. A more quantitative analysis of the relationship between planetary wave breaking and MILs at Chatanika will be presented in a forthcoming paper [Irving et al., 2012]. Salby et al. [2002] note that even if the lapse rate is not fully reversed during periods of strong planetary wave activity, the synoptic pattern of strengthened stability favors the generation of isolated inversions. These isolated inversion can be produced locally and intermittently by breaking gravity waves and tides.

This study did not explicitly investigate the transient structure of planetary waves at Chatanika and therefore cannot comment on the contribution proposed by Gan et al. [2012]. In a previous study by Lieberman et al. [2012], the relationship between

planetary waves and MILs was examined during 27–28 January 2005. The EP flux divergence was computed for January 2005 and used to determine the wave stress associated with planetary wave-one and wave-two. The temperature anomaly arising from the planetary wave forcing (not shown) was shown to be consistent with the amplitude and altitude of a MIL observed at Chatanika on 27–28 January 2005. The winter occurrence rate is similar to that observed by satellite studies at middle and high latitudes [e.g., Leblanc et al., 1995; Sassi et al., 2002; Gan et al., 2012] with maximum observed in winter. However, since lidar data is not available during the summer months of June and July, this study does not address MIL formation mechanisms in summer.

Whiteway et al. [1995] proposed that the presence of near adiabatic lapse rates above MILs are indicative of a well-mixed turbulent layer and interpreted MILs as a direct result of turbulent mixing and dissipation. Topside lapse rates less than –8.0 K km^{-1} are seen in 20% of the 2 h MILs (restricted to those below 70 km) and increases to 32% when extended to –7.0 K km^{-1}. The occurrence of topside lapse rates approaching the adiabatic lapse rate point to conditions where convective instability and wave-breaking can occur due to the enhanced development of turbulence above the MIL. To fully understand the significance of adiabatic lapse rates, studies that quantify turbulence in the presence of MILs are needed, such as Collins et al. [2011].

Gravity waves have long been thought to play a role in the formation of MILs [e.g., Hauchecorne et al., 1987; Whiteway et al., 1995; Liu and Hagan, 1998; Liu et al., 2000; Meriwether and Gerrard, 2004]. Although the vertical phase velocities found in this study are steeper than those reported by Cutler et al. [2001] (mean phase progression of –0.2 km h^{-1} compared to 0.2 km h^{-1}), they are shallower than those expected from gravity waves [Collins and Smith, 2004; Liu and Meriwether, 2004]. However, higher than average rms density perturbations during spring 2003 have been reported in the presence of MILs [Wang, 2003], suggesting gravity wave activity is related to MILs. Gravity wave activity was not investigated in this thesis, but will be in future studies [Irving et al., 2012].

4.6. Summary

This study has investigated the classic "lower" MIL [Meriwether and Gerrard, 2004] at a high latitude site in the Western Arctic. The MILs observed by the NICT Rayleigh lidar at Poker Flat Research Range, Chatanika, Alaska (65°N, 213°E), have characteristics similar to those reported at midlatitudes but are seen less often and included small amplitude MILs (< 10 K). Namely, the occurrence rate of MILs appears to exhibits an annual cycle with largest occurrence rates in winter, although lidar measurements are not available during summer months of June and July. Interannual variability seen in lidar temperature profiles and planetary wave structure makes it difficult to find the definitive formation mechanism responsible for MILs.

Planetary wave structure has been shown to play an important role in the formation of MILs at a high latitude site (65°N, 213°E). MILs observed by Rayleigh lidar are often part of a large spatiotemporal inversion in the upper mesosphere associated with regions of negative geopotential height perturbation, Z'. Inversions have been found just above the region of negative maximum of Z', capping a region of westward tilt and amplification with height below. Above the inversion, westward tilt weakens and is replaced overhead by barotropic structure, evidence of strong wave dissipation. The examples supporting this are during active periods of stratospheric warmings. When studying the relationship between the MILs (with a peak altitude below 80 km, 73 MILs in 45 days) observed by lidar at Chatanika, when coincident SABER data is available, 70% of the MILs are found in regions of negative Z', and 60% of the MILs are found in the positive vertical curvature of Z'. These observations are not always associated with planetary wave breaking, supporting the idea proposed by Sica et al. [2007] that MILs can form through wave saturation (hydrostatic balance) without the necessity of a wind reversal in the mesosphere.

The interannual variability observed in the SABER planetary wave structure at 65°N adds complexity to elucidating the formation mechanisms of MILs. Except 2005, stratospheric warmings have occurred in every winter/spring season where concurrent

lidar and SABER data are available. Further work is required to understand the impact of topside lapse rates approaching the adiabatic lapse rates the effect on the inversion stability and lifetime. Furthermore, the transient structure of the quasistationary planetary wave-one and westward 16-day wave should be investigated in light of the recent findings by Gan et al. [2012], and Lieberman et al. [2012].

The statistics of MIL characteristics at Chatanika reported in this study were restricted to those with a peak altitude in the lidar temperature profile below 70 km. This limited the ability to quantitatively analyze the upper altitude MILs that are thought to be most closely related to planetary waves. Temperature retrievals from the extended Rayleigh lidar system (discussed in Chapter 3) have to potential to extend the 70 km boundary. This will allow the future classification of MILs to extend above 85 km, the upper bound associated with lower MIL [Meriwether and Gerrard, 2004].

Chapter 5. Conclusions and Recommendations for Future Work

In this thesis, I have presented a scientific study of mesospheric inversion layers (MILs) and a technical study of the performance of the Rayleigh lidar system Poker Flat Research Range, Chatanika, Alaska (65°N, 213°E). I have extended the scope of previous MIL studies in two ways. First, I have developed a new algorithm to detect MILs in lidar temperature profiles. Second, I have analyzed satellite data to understand MILs and their relationship to global scale planetary wave structure.

I have identified and characterized MILs in the 149 average temperature profiles with a duration greater than 4.0 h using data from ongoing observations over a 12-year period from 1997 – 2009. My investigation of MILs over this 12-year period considered only the statistical error due to photon counting in the temperature retrieval when determining whether the MIL was statistically significant. Once I identified a MIL in the average temperature profile between the stratopause (if applicable) and 80 km, I used an algorithm to test its significance. If the MIL was a statistically significant inversion, I then inspected the individual sequential 2 h temperature profiles and identified the statistically significant MIL. I determined the vertical phase progression, or phase velocity (km h^{-1}), of MILs in the 2 h temperature profiles over the course of the observation (i.e. a 10 h observation would have 5 individual 2 h temperature profiles). In investigating the 2 h profiles, I found some statistically significant MILs that were averaged out over the whole observation period. Thus, I found that the occurrence rate of MILs identified in the 2 h temperature profiles (i.e., 47%) is larger than that estimated from the average temperature profiles (i.e., 37%). This occurrence rate is higher than the occurrence rate of 19% reported by Cutler and co-workers in the first study of MILs at PFRR [Cutler et al., 2001], and is due to the lower error used in the algorithm to test for the presence of a significant MIL. When I limited the detection to large amplitude MILS ($\geq$ 10 K), I found an occurrence rate of 28% (in the 2 h temperature profiles) which is significantly less than the ~70% reported at midlatitudes [Hauchecorne et al., 1987]. However, when I limited the detection (significance) criteria to MILs with a topside lapse

rate approaching the adiabatic lapse rate ($\geq$ -8 K km^{-1}) and a depth of at least 2.4 km, I found an occurrence rate of 13% which is significantly more than the 5% reported at a high latitude site by Duck and Greene [2004].

I used data from the SABER instrument aboard the TIMED satellite to investigate the planetary wave structure associated with MILs at Chatanika. I employed SABER geopotential height, temperature, and EP flux data to study the relationship to MILs at 65°N over 74 (out of the 149) days when coincident lidar and satellite data were available. The common observations presented in this thesis were over the periods of mid-January through mid-March and mid-September through mid-November in 2002 through 2009. I found that 70% of the MILs at Chatanika were located in the negative phase and 60% of the MILs were located in positive vertical curvature of the geopotential height perturbation field (departure from the zonal mean). I found that the occurrence of MILs in the lidar temperature profile appear to be preceded by periods of negative EP flux divergence. These findings suggest that MILs are closely related to planetary wave activity over Chatanika, although a quantitative analysis of the contribution of planetary wave breaking to the formation of MILs was not performed.

I found that MILs have vertical phase speeds (-0.2 $\pm$ 0.5 km h^{-1}) that are slower than those associated with gravity waves (typically less than –1 km h^{-1}), suggesting that the MILs are not primarily formed by gravity waves. However, higher than average rms density perturbations during spring 2003 have been reported in the presence of MILs [Wang, 2003] suggesting some linkage between gravity wave activity and MILs. Gravity wave activity was not further investigated in this thesis.

I did not attempt to form a complete theory of the mechanisms responsible for the formation of MILs at Chatanika for two primary reasons. First, the statistics reported in this thesis were restricted to MILs with a peak altitude below 70 km due to the contribution of the initial temperature estimate at 80 km. Extending the analysis of MILs above 70 km would greatly increase the population statistics (from 37% to approximately 60%), allowing for a more comprehensive understanding and provide better insight into

planetary wave and gravity wave influences. Second, lidar measurements are currently available from August through May but not during the summer months due to the high solar elevation at Chatanika in June and July. The lidar observation rates in fall and early winter are low due to cloudier weather compared to late winter and spring. Without year round lidar measurements, elucidating whether the formation mechanism of MILs is primarily from, for example, gravity waves or planetary waves is difficult. If summer measurements were available, the contribution of planetary waves to the formation of winter MILs may become more apparent because planetary waves cannot propagate vertically in the summer stratospheric westward jet. Previous studies report differences in the characteristics of summer and winter MILs [e.g., Hauchecorne et al., 1987; 1991], suggesting different formation mechanisms.

I have extended the scope of earlier lidar studies by integrating a more powerful Nd:YAG laser (22.5 W rather than 7.5 W) and larger aperture receiving telescope (104 cm rather than 62 cm) into an extended Rayleigh lidar system at PFRR. I have conducted comprehensive field tests of the extended lidar system with the goal of establishing an improved in system performance and the data acquisition techniques. I have shown that the extended Rayleigh lidar system performance permits the upper altitude used for temperature retrieval to be extended to 90 km. This is significant for future studies of MILs at Chatanika, as MILs are a common feature above 70 km in the lidar temperature profile.

I found that the extended Rayleigh lidar system does not currently permit temperature retrievals below approximately 50 km because the increased signals yield a higher photon count rate than receiver's maximum photon count rate and results in pulse pileup. Pulse pileup results in a nonlinear lidar signal where the signal is no longer proportional to the atmospheric density. I have modeled this effect and demonstrated that the nonlinearity in signal can be corrected. By modeling pulse pileup, I was able to experimentally determine the detector dead time of 8.7 ns. This nonlinear response in the receiver results in artificially higher temperatures reported below 50 km. Therefore, it is crucial to

correct for pulse pileup in future studies, and especially when investigating long term temperature trends. The receiver system's dead time provides a measure of the maximum photon count rate and determines the linear operating range of the system. Thus, the value of the dead time that I determined can be used in the temperature retrieval algorithm to correct for pulse pileup and yield more accurate temperatures without changes to the extended Rayleigh lidar system. Pulse pileup can also be avoided by upgrading the receiver system.

Based on my field tests, I propose the following solution to circumvent nonlinear signals at the lowest altitudes while maintaining the signal gains at the higher altitudes. The field tests revealed that using a dual telescope receiver to detect signal from the stratosphere below the pulse pileup count rate threshold is not feasible. The two telescopes cannot be aligned with sufficient accuracy to ensure bore-sighting of both telescopes with the laser. A solution would be to install a beam splitter in the receiver chain of a single telescope to yield two independent signal channels. The first channel would receive a fraction (e.g., 10%) of the total lidar signal with counting rates below the pulse pileup threshold and account for a "low altitude" channel (e.g., measurements below 50 km). The remainder of the signal (e.g., 90%) would be used as a "high altitude" channel (e.g., measurements above 50 km). With this improvement, the lidar system would provide integrated measurements over the 30 km to 90 km altitude region. Measurements over this range would immediately allow the lidar to resolve the high altitude MILs above 70 km that are often seen in the lidar observations and that appear routinely in the SABER observations. More generally, the lidar could then support more complete studies of the middle atmosphere that address wave coupling from the mid-stratosphere to the lower-thermosphere at Chatanika.

References

Alpers, M., R. Eixmann, C. Fricke-Begemann, M. Gerding, and J. Höffner (2004), Temperature lidar measurements from 1 to 105 km altitude using resonance, Rayleigh, and Rotational Raman Scattering, *Atmos. Chem. Phys. 4*, 793-800, doi:1680-7324/acp/2004-4-793.

Atkinson, R. J., W. A. Matthews, P. A. Newman, and R. A. Plumb (1989), Evidence of the mid-latitude impact of Antarctic ozone depletion, *Nature*, *340*(6231), 290-294, doi:10.1038/340290a0.

Baker, D. J., and A. T. Stair Jr. (1988), Rocket measurements of the altitude distributions of the hydroxyl airglow, *Physica Scripta, 37*, 611–622, doi:10.1088/0031-8949/37/4/021.

Bishop, R. L., M. F. Larsen, J. H. Hecht, A. Z. Liu, and C. S. Gardner (2004), TOMEX: Mesospheric and lower thermospheric diffusivities and instability layers, *J. Geophys. Res.*, *109*, D02S03, doi:10.1029/2002jd003079.

Brinksma, E. J., Y. J. Meijer, I. S. McDermid, R. P. Cageao, J. B. Bergwerff, D. P. J. Swart, W. Ubachs, W. A. Matthews, W. Hogervorst, and J. W. Hovenier (1998), First lidar observations of mesospheric hydroxyl, *Geophys. Res. Lett.*, *25*(1), 51–54, doi:10.1029/97GL53561.

Bureau, R. (1946), Altimetry clouds by light pulses, *La Météorologie,* 3, 292.

Chandran, A., R. L. Collins, R. R. Garcia, and D. R. Marsh (2011), A case study of an elevated stratopause generated in the Whole Atmosphere Community Climate Model, *Geophys. Res. Lett.*, *38*(8), doi:10.1029/2010gl046566.

Charney, J. G., and P. G. Drazin (1961), Propagation of Planetary-Scale Disturbances from the Lower into the Upper Atmosphere, *J. Geophys. Res.*, *66*(1), 83-109, doi:10.1029/JZ066i001p00083.

Collins, R. L. (2004), *Pan-Arctic Study of the Stratospheric and Mesospheric circulation (PASSMeC),* Expressions of Intent for International Polar Year 2007- 2008 activities, ID no.11.

Collins, R. L., and R. W. Smith (2004), Evidence of damping and overturning of gravity waves in the Arctic mesosphere: Na lidar and OH temperature observations, *J. Atmos. Sol. Terr. Phys., 66*, 867–879, doi:10.1016/j.jastp.2004.01.038.

Collins, R. L., G. A. Lehmacher, M. F. Larsen, and K. Mizutani (2011), Estimates of vertical eddy diffusivity in the upper mesosphere in the presence of a mesospheric inversion layer, *Ann. Geophys.*, *29*(11), 2019-2029, doi:10.5194/angeo-29-2019-2011.

Collins, R. L., M. C. Kelley, M. J. Nicolls, C. Ramos, T. Hou, T. E. Stern, K. Mizutani, and T. Itabe (2003), Simultaneous lidar observations of a noctilucent cloud and an internal wave in the polar mesosphere, *J. Geophys. Res., 108*, 8435, doi:10.1029/2002JD002427.

Collins, R. L., M. J. Taylor, K. Nielsen, K. Mizutani, Y. Murayama, K. Sakanoi, M. T. DeLand (2009), Noctilucent Cloud in the Western Arctic in 2005: Simultaneous Lidar and Camera Observations and Analysis, *J. Atmos. Sol. Terr. Phys.*, *71*, 446-452, doi:10.1016/j.jastp.2008.09.044.

Cutler, L. J. (2000), *Rayleigh lidar studies of the Arctic middle atmosphere,* M.S. Thesis, University of Alaska, Fairbanks.

Cutler, L. J., R. L. Collins, K. Mizutani, and T. Itabe (2001), Rayleigh lidar observations of mesospheric inversion layers at Poker Flat, Alaska (65 °N, 147°W), *Geophys. Res. Lett.*, *28*(8), 1467, doi:10.1029/2000gl012535.

Dao, P. D., R. Farley, X. Tao, and C. S. Gardner (1995), Lidar observations of the temperature profile between 25 and 103 km: Evidence of strong tidal perturbation, *Geophys. Res. Lett.*, *22*(20), 2825–2828, doi:10.1029/95GL02950.

Das, U., and C. J. Pan (2011), The temperature structure of the mesosphere over Taiwan and comparison with other latitudes, *J. Geophys. Res., 116*, D00P06, doi:10.1029/2010JD015034.

de la Torre, L., R. R. Garcia, D. Barriopedro, and A. Chandran (2012), Climatology and characteristics of stratospheric sudden warmings in the Whole Atmosphere Community Climate Model, *J. Geophys. Res.*, *117*, D04110, doi:10.1029/2011JD016840.

Dewan, E. M., and R. H. Picard (1998), Mesospheric bores, *J. Geophys. Res.*, *103*(D6), 6295–6305, doi:10.1029/97JD02498.

Dewan, E. M., and R. H. Picard (2001), On the origin of mesospheric bores, *J. Geophys. Res.*, *106*(D3), 2921–2927, doi:10.1029/2000JD900697.

Donovan, D. P., J. A. Whiteway, and A. I. Carswell (1993), Correction for nonlinear photon-counting effects in lidar systems, *Appl. Opt.*, *32*(33), 6742, doi:10.1364/ao.32.006742.

Duck, T. J., and M. D. Greene (2004), High Arctic observations of mesospheric inversion layers, *Geophys. Res. Lett.*, *31*(2), L02105, doi:10.1029/2003gl018481.

Duck, T. J., D. P. Sipler, J. E. Salah, and J. W. Meriwether (2001), Rayleigh lidar observations of a mesospheric inversion layer during night and day, *Geophys. Res. Lett.*, *28*(18), 3597–3600, doi:10.1029/2001GL013409.

Elterman, L. (1951), The measurement of stratospheric density distribution with the searchlight technique, *J. Geophys. Res., 56*(4), 509-520, doi:10.1029/JZ056i004p00509.

Evans, R. D. (1955), *The Atomic Nucleus*, 972 pp., McGraw-Hill, New York.

Farman, J. C., B. G. Gardiner, and J. D. Shanklin (1985), Large losses of total ozone in Antarctica reveal seasonal ClOx/NOx interaction, *Nature*, *315*(6016), 207-210, doi:10.1038/315207a0.

Fechine, J., C. M. Wrasse, H. Takahashi, M. G. Mlynczak, and J. M. Russell (2007), Lower-mesospheric inversion layers over Brazilian equatorial region using TIMED/SABER temperature profiles, *Adv. Space Res., 41*(9), 1447-1453, doi:10.1016/j.asr.2007.04.070.

Fritts, D. C., and M. J. Alexander (2003), Gravity wave dynamics and effects in the middle atmosphere, *Reviews of Geophysics*, *41*(1), doi:10.1029/2001rg000106.

Fujii, T., and T. Fukuchi (2005), *Laser remote sensing*, 888 pp., CRC Press, Florida.

Gan, Q., S. D. Zhang, and F. Yi (2012), TIMED/SABER observations of lower mesospheric inversion layers at low and middle latitudes, *J. Geophys. Res.*, *117*, D07109, doi:10.1029/2012jd017455.

Garcia, R. R., and S. Solomon (1985), The effect of breaking gravity waves on the dynamics and chemical composition of the mesosphere and lower thermosphere, *J. Geophys. Res.*, *90*, 3850-3868, doi:10.1029/JD090iD02p03850.

García-Comas, M., M. López-Puertas, B. T. Marshall, P. P. Wintersteiner, B. Funke, D. Bermejo-Pantaleón, C. J. Mertens, E. E. Remsberg, L. L. Gordley, M. G. Mlynczak, and J. M. Russell III (2008), Errors in Sounding of the Atmosphere using Broadband Emission Radiometry (SABER) kinetic temperature caused by non-local-thermodynamic-equilibrium model parameters, *J. Geophys. Res.*, *113*(D24), doi:10.1029/2008jd010105.

Hamamatsu Photonics K. K. (2005), Photon counting using photomultiplier tubes, Hamamatsu Photonics K.K., Technical Information, *TPHO9001E04*.

Hamamatsu Photonics K. K. (2006), Photomultiplier tubes: Basics and applications, Hamamatsu Photonics K.K., Electron Tube Division, *TOTH9001E03*.

Harvey, V. L., R. B. Pierce, T. D. Fairlie, M. H. Hitchman (2002), A climatology of stratospheric polar vortices and anticyclones, *J. Geophys. Res., 104*, 4442-4464, doi:10.1029/2001JD001471

Hauchecorne, A., and M.-L. Chanin (1980), Density and temperature profiles obtained by lidar between 35 and 70 km, *Geophys. Res. Lett.*, *7*(8), 565, doi:10.1029/GL007i008p00565.

Hauchecorne, A., M. L. Chanin, and R. Wilson (1987), Mesospheric temperature inversion and gravity wave breaking, *Geophys. Res. Lett.*, *14*(9), 933, doi:10.1029/GL014i009p00933.

Hauchecorne, A., M.-L. Chanin, and P. Keckhut (1991), Climatology and trends of the middle atmospheric temperature (33–87 km) as seen by Rayleigh lidar over the south of France, *J. Geophys. Res.*, *96*(D8), 15,297–15,309, doi:10.1029/91JD01213.

Hedin, A. E. (1991), Extension of the MSIS Thermosphere Model into the Middle and Lower Atmosphere, *J. Geophys. Res.*, *96*(A2), 1159-1172, doi:10.1029/90ja02125.

Holton, J. R. (1983), The influence of gravity wave breaking on the general circulation of the middle atmosphere, *J. the Atmos. Sci.*, *40*(10), 2497-2507, doi:10.1175/1520-0469(1983)040<2497:tiogwb>2.0.co;2.

Holton, J. R. (2004), *An introduction to dynamic meteorology*, 535 pp. Elsevier Academic Press, Massachusetts.

Holton, J. R., and M. J. Alexander (2000), The role of waves in the transport circulation of the middle atmosphere, in *Atmospheric Science Across the Stratopause*, *Geophys. Monogr. Ser.*, vol. 123, edited by D. E. Siskind, S. D. Eckermann, and M. E. Summers, pp. 21–35, AGU, Washington, D. C., doi:10.1029/GM123p0021.

Holton, J. R., P. H. Haynes, M. E. McIntyre, A. R. Douglass, R. B. Rood, and L. Pfister (1995), Stratosphere-troposphere exchange, *Reviews of Geophysics*, *33*(4), 403, doi:10.1029/95rg02097.

Houghton, J. T. (1978), The stratosphere and mesosphere, *Quarterly Journal of the Royal Meteorological Society*, *104*(439), 1-29, doi:10.1002/qj.49710443902.

ICSU (International Council for Science) (2004), *A framework for the International Polar Year 2007-2008*, www.ipy.org, pp73.

Irving, B. K., R. L. Collins, R. A. Lieberman, B. Thurairajah, K. Mizutani (2012), Mesospheric inversion layers seen by Rayleigh lidar and their relationship to planetary wave structure over Chatanika, Alaska, *paper in preparation for submission to J. Geophys. Res.*.

Keckhut, P., A. Hauchecorne, M. L. Chanin (1995), Midlatitude long-term variability of the middle atmosphere: Trends and cyclic and episodic changes, *J. Geophys. Res.*, *100*(D9), 18,887–18,897, doi:10.1029/95JD01387.

Kelley, M. C., M. J. Nicolls, R. H. Varney, R. L. Collins, R. Doe, J. M. C. Plane, J. Thayer, M. Taylor, B. Thurairajah, and K. Mizutani (2010), Radar, lidar, and optical observations in the polar summer mesosphere shortly after a space shuttle launch, *J. Geophys. Res.*, *115*, A05304, doi:10.1029/2009ja014938.

Kent, G. S., B. R. Clemesha, and R. W. Wright (1967), High altitude atmospheric scattering of light from a laser beam, *J. Atmos. Terr. Phys.*, *29*(2), 169-181, doi:10.1016/0021-9169(67)90131-6.

Labitzke, K. (1972), Temperature changes in the mesosphere and stratosphere connected with circulation changes in winter, *J. Atmos. Sci., 29*(4), 756-766, doi:10.1175/1520-0469(1972)029<0756:tcitma>2.0.co;2.

Leblanc, T., A. Hauchecorne, M. Chanin, C. Rodgers, F. Taylor, and N. Livesey (1995), Mesospheric temperature inversions as seen by ISAMS in December 1991, *Geophys. Res. Lett., 22*(12), 1485–1488, doi:10.1029/94GL03274.

Leblanc, T., and A. Hauchecorne (1997), Recent observations of mesospheric temperature inversions, *J. Geophys. Res.*, *102*, 19471-19482, doi:10.1029/97jd01445.

Leblanc, T., I. S. McDermid, A. Hauchecorne, and P. Keckhut (1998), Evaluation of optimization of lidar temperature analysis algorithms using simulated data, *J. Geophys. Res.*, *103*, 6177-6187, doi:10.1029/97jd03494.

Lehmacher, G., and F.-J. Lübken (1995), Simultaneous observation of convective adjustment and turbulence generation in the mesosphere, *Geophys. Res. Lett.*, *22*(18), 2477-2480, doi:10.1029/95gl02351.

Lieberman, R. A., R. L. Collins, B. K. Irving, D. A. Ortland (2012), Breaking waves, *International Innovation, 3*, 48-50.

Light, A., (2009), *Theoretical and Experimental Investigations of Resonance Fluorescence Lidar for Measurements of N^+_2 in the Auroral Atmosphere*, MS Thesis, University of Alaska Fairbanks.

Liou, K.-N. (1980), *An Introduction to Atmospheric Radiation*, 392 pp., Academic, New York.

Liu, H.-L., and J. W. Meriwether (2004), Analysis of a temperature inversion event in the lower mesosphere, *J. Geophys. Res.*, *109*, D02S07, doi:10.1029/2002JD003026.

Liu, H.-L., and M. E. Hagan (1998), Local heating/cooling of the mesosphere due to gravity wave and tidal coupling, *Geophys. Res. Lett.*, *25*(15), 2941-2944, doi:10.1029/98gl02153.

Liu, H.-L., M. E. Hagan, and R. G. Roble (2000), Local mean state changes due to gravity wave breaking modulated by the diurnal tide, *J. Geophys. Res.*, *105*(D10), 12381–12396, doi:10.1029/1999JD901163.

Liu, Z., Z. Li, B. L, and R. Li (2009), Analysis of saturation signal correction for the troposphere lidar, *Chinese Opt. Lett. 7*(11), 1051-1054, doi:10.3788/COL20090711.1051.

Lübken, F.-J (1997), Seasonal variation of turbulent energy dissipation rates at high latitudes as determined by in situ measurements of neutral density fluctuations, *J. Geophys. Res., 102*(D12), 13,441–13,456, doi:10.1029/97JD00853.

Lübken, F.-J. (1999), Thermal structure of the Arctic summer mesosphere, *J. Geophys. Res., 104*(D8), 9135-9149, doi:10.1029/1999JD900076.

Manney G. L., M. L. Santee1, M. Rex, N. J. Livesey, M. C. Pitts, P. Veefkind, E. R. Nash, I. Wohltmann, R. Lehmann, L. Froidevaux, L. R. Poole, M. R. Schoeberl, D. P. Haffner, J. Davies, V. Dorokhov, H. Gernandt, B. Johnson, R. Kivi, E. Kyro, N. Larsen, P. F. Levelt, A. Makshtas, C. T. McElroy, H. Nakajima, M. Concepción Parrondo, D. W. Tarasick, P. von der Gathen, K. A. Walker, and N. S. Zinoviev (2011), Unprecedented Arctic ozone loss in 2011, *Nature, 478*(7370), 469–477, doi:10.1038/nature10556.

Manney, G. L., K. Krüger, J. L. Sabutis, S. A. Sena, and S. Pawson (2005), The remarkable 2003–2004 winter and other recent warm winters in the Arctic stratosphere since the late 1990s, *J. Geophys. Res.*, *110*, D04107, doi:10.1029/2004jd005367.

Manney, G. L., M. J. Schwartz, K. Krüger, M. L. Santee, S. Pawson, J. N. Lee, W. H. Daffer, R. A. Fuller, and N. J. Livesey (2009), Aura Microwave Limb Sounder observations of dynamics and transport during the record-breaking 2009 Arctic stratospheric major warming, *Geophys. Res. Lett.*, *36*(12), L12815, doi:10.1029/2009gl038586.

Matsuno, T. (1971), A dynamical model of the stratospheric sudden warming, *J. Atmos. Sci.*, *28*, 1479–1494, doi:10.1175/1520-0469(1971)028<1479:ADMOTS>2.0.CO;2.

McIntyre, M. E., and T. N. Palmer (1984), The 'surf zone' in the stratosphere, *J. Atmos. Terr. Phys.*, *46*(9), 825-849, doi:10.1016/0021-9169(84)90063-1.

Measures, R. M. (1984), *Laser remote sensing fundamentals and applications*, 510 pp., Krieger, Florida.

Meriwether, J. W., and A. J. Gerrard (2004), Mesosphere inversion layers and stratosphere temperature enhancements, *Reviews of Geophysics*, *42*(3), RG3003, doi:10.1029/2003rg000133.

Meriwether, J. W., and M. G. Mlynczak (1995), Is chemical heating a major cause of the mesosphere inversion layer?, *J. Geophys. Res.*, *100*, 1379-1387, doi:10.1029/94jd01736.

Mertens, C. J., F.J. Schmidlin, R. A. Goldberg, E. E. Remsberg, W. D. Pesnell, J. M. Russell III, M. G. Mlynczak, M. López-Puertas, P. P. Wintersteiner, R. H. Picard, J. R. Winick, and L. L. Gordley (2004), SABER observations of mesospheric temperatures and comparisons with falling sphere measurements taken during the 2002 summer MaCWAVE campaign, *Geophys. Res. Lett.*, *31*(3), L03105, doi:10.1029/2003gl018605.

Mertens, C. J., M. G. Mlynczak, M. López-Puertas, P. P. Wintersteiner, R. H. Picard, J. R. Winick, L. L. Gordley, and J. M. Russell III (2002), Retrieval of kinetic temperature and carbon dioxide abundance from nonlocal thermodynamic equilibrium limb emission measurements made by the SABER experiment on the TIMED satellite, *Proc. SPIE Int. Soc. Opt. Eng., 4882*, 162–171.

Middleton, W. E. K., and A. F. Spilhaus (1953), *Meteorological Instruments*, 286 pp., Toronto Press, Toronto.

Mizutani, K., T. Itabe, M. Yasui, T. Aoki, Y. Murayama, and R. L. Collins (2000), Rayleigh and Rayleigh Doppler lidars for the observations of the Arctic middle atmosphere, *IEICE Trans. Fundam. Electron. Commun. Comput. Sci.,* E83-B, 2003.

Murayama, Y., M. Ishii, M. Kubota, M. Hirotaka, K. Mizutani, S. Ochiai, Y. Kasai, S. Kawamaura, Y. Tanaka, H. Masuko, T. Iguchi, H. Kumagai, T. Kikuchi, K. Sata, R. L. Collins, B. J. Watkins, M. Conde, W. B. Bristow, and R. W. Smith (2007), Comprehensive Arctic atmosphere observing system and observed results for system performance demonstration, *J. Nat. Instit. Info. Comms. Tech*, *54*(1/2), 5-16.

Nadakuditi, S. (2005), *Spectral estimation of wave-driven fluctuations in Rayleigh lidar temperature measurements*, MS Thesis, University of Alaska Fairbanks.

Newman, P. A., E. R. Nash, and J. E. Rosenfield (2001), What controls the temperature of the Arctic stratosphere during the spring?, *J. Geophys. Res.*, *106*(D17), 19999-20010, doi:10.1029/2000jd000061.

Nielsen, K., R. L. Collins, P.-D. Pautet, Y. Zhao, B. K. Irving, M. J. Taylor, M. Negale, and Y. Murayama (2012), Successive Thermally Ducted Arctic Mesospheric Frontal Events, *paper in preparation for submission to Geophys. Res. Lett.*.

NRC (National Research Council) (2004), *A vision for the International Polar Year 2007-2008*, Washington D. C., National Academy Press, pp96.

Oberheide, J., H. L. Liu, O. A. Gusev, and D. Offermann (2006), Mesospheric surf zone and temperature inversion layers in early November 1994, *CRISTA 1and2 Results in the Mesosphere and Lower Thermosphere*, *68*(15), 1752-1763, doi:10.1016/j.jastp.2005.11.013.

Papoulis, A. (1984), *Probability, random variables, and stochastic processes,* 576 pp., McGraw-Hill, New York.

Petty, G. W. (2006), *A First Course in Atmospheric Radiation*, 445 pp., Sundog Publishing, Wisconsin.

Randel, W., P. Udelhofen, E. Fleming, M. Geller, M. Gelman, K. Hamilton, D. Karoly, D. Ortland, S. Pawson, R. Swinbank, F. Wu, M. Baldwin, M.-L. Chanin, P. Keckhut, K. Labitzke, E. Remsberg, A. Simmons, and D. Wu (2004), The SPARC intercomparison of middle–atmosphere climatologies, *J. Climate*, *17*(5), 986-1003, doi:10.1175/1520-0442(2004)017<0986:TSIOMC>2.0.CO;2

Remsberg, E., G. Lingenfelser, V. L. Harvey, W. Grose, J. Russell III, M. Mlynczak, L. Gordley, and B. T. Marshall, (2003), On the verification of the quality of SABER temperature, geopotential height, and wind fields by comparison with Met Office assimilated analyses, *J. Geophys. Res., 108*(D20), 4628, doi:10.1029/2003JD003720.

Remsberg, E.E., B. T. Marshall, M. García-Comas, D. Krueger, G. S. Lingenfelser, J. Martin-Torres, M. G. Mlynczak, J. M. Russell III, A. K. Smith, Y. Zhao, C. Brown, L. L. Gordley, M. J. Lopez-Gonzalez, M. Lopez-Puertas, C.-Y. She, M. J. Taylor, R. E. Thompson (2008), Assessment of the quality of the retrieved temperature versus pressure profiles of the middle atmosphere from TIMED/SABER, *J. Geophys. Res.*, *113*, D17101, doi:10.1029/2008jd010013.

Russell, J. M., III, M. G. Mlynczak, L. L. Gordley, J. Tansock, and R. Esplin (1999), An overview of the SABER experiment and preliminary calibration results, *Proc. SPIE Int. Soc. Opt. Eng.,* 3756, 277–288.

Salby, M. L. (1996), *Fundamentals of atmospheric physics*, 627 pp., Academic Press, California.

Salby, M., F. Sassi, P. Callaghan, D. Wu, P. Keckhut, and A. Hauchecorne (2002), Mesospheric inversions and their relationship to planetary wave structure, *J. Geophys. Res.*, *107*, 4041, doi:10.1029/2001JD000756.

Sassi, F., R. R. Garcia, B. A. Boville, and H. Liu (2002), On temperature inversions and the mesospheric surf zone, *J. Geophys. Res.*, *107*, 4380, doi:10.1029/2001jd001525.

Schmidlin, F. J. (1976), Temperature inversions near 75 km, *Geophys. Res. Lett.*, *3*(3), 173-176, doi:10.1029/GL003i003p00173.

Schoeberl, M. R., and D. L. Hartmann (1991), The dynamics of the stratospheric polar vortex and its relation to springtime ozone depletions, *Science*, *251*(4989), 46-52, doi:10.1126/science.251.4989.46.

Schroeder, D. J. (2000), *Astronomical Optics*, 478 pp., Academic Press, California.

Sica, R. J., P. S. Argall, T. G. Shepherd, and J. N. Koshyk (2007), Model-measurement comparison of mesospheric temperature inversions, and a simple theory for their occurrence, *Geophys. Res. Lett.*, *34*(23), L23806, doi:10.1029/2007gl030627.

Silfvast, W. T. (1996), *Laser Fundamentals*, 521 pp., Cambridge University Press, New Delhi.

Smith, A. K., R. R. Garcia, D. R. Marsh, and J. H. Richter (2011), WACCM simulations of the mean circulation and trace species transport in the winter mesosphere, *J. Geophys. Res., 116,* D20115,doi:10.1029/2011JD016083.

Smith, K. (2010), SABER - Sounding of the Atmosphere Using Broadband Emission Radiometry, January 2010, <http://saber.gats-inc.com/index.php>.

Solomon, S., R.R. Garcia, F.S. Rowland, and D.J. Wuebbles (1986), On the depletion of Antarctic ozone, *Nature, 321*, 755-758, doi:10.1038/321755a0.

SPARC (2002), *SPARC intercomparison of middle atmosphere climatologies*, SPARC Rep. 3, 96 pp.

States, R. J., and C. S. Gardner (2000), Thermal Structure of the Mesopause Region (80–105 km) at 40°N Latitude. Part II: Diurnal Variations, *J. the Atmos. Sci, 57*(1), 78-92, doi:10.1175/1520-0469(2000)057<0078:tsotmr>2.0.co;2.

Stevens, M. H., J. Gumbel, C. R. Englert, K. U. Grossmann, M. Rapp, and P. Hartogh (2003), Polar mesospheric clouds formed from space shuttle exhaust, *Geophys. Res. Lett.*, *30*(10), 1546, doi:10.1029/2003gl017249.

Stevens, M. H., R. R. Meier, X. Chu, M. T. DeLand, and J. M. C. Plane (2005), Antarctic mesospheric clouds formed from space shuttle exhaust, *Geophys. Res. Lett.*, *32*(13), L13810, doi:10.1029/2005gl023054.

Strutt, J. W. (Lord Rayleigh) (1899), On the transmission of light through an atmosphere containing small particles in suspension, and on the origin of the blue of the sky, *Phil. Mag. XLVII*, pp. 375-384.

Taylor, J. R. (1996), *An introduction to error analysis: the study of uncertainties in physical measurement*, 327 pp., University Science Books, California.

Taylor, M. J., D. N. Turnbull, and R. P. Lowe (1995), Spectrometric and imaging measurements of a spectacular gravity wave event observed during the ALOHA-93 Campaign, *Geophys. Res. Lett.*, *22*(20), 2849–2852, doi:10.1029/95GL02948.

Taylor, M. J., Y. Zhao, P.-D. Pautet, M.J. Nicolls, R.L. Collins, J. Baker-Tvedtness, C.D. Burton, B. Thurairajah, J. Reimuller, R.H. Varney, C.J. Heinselman, and K. Mizutani (2009), Coordinated optical and radar image measurements of noctilucent clouds and polar mesospheric summer echoes, *J. Atmos. Sol. Terr. Phys.*, *71*, 675-687, doi:10.1016/j.jastp.2008.12.005.

Thomas, L., A. K. P. Marsh, D. P. Wareing, I. Astin, and H. Chandra (1996), VHF echoes from the midlatitude mesosphere and the thermal structure observed by lidar, *J. Geophys. Res.*, *101*, 12867-12877, doi:10.1029/96jd00218.

Thurairajah, B. (2009), *Role of waves in the circulation of the Arctic middle atmosphere: Rayleigh lidar measurements and analysis*, PhD Dissertation, University of Alaska Fairbanks.

Thurairajah, B., R. L. Collins, and K. Mizutani (2009), Multi-year temperature measurements of the middle atmosphere at Chatanika, Alaska (65°N, 147°W), *Earth, Planets and Space*, *61*(6), 755-764.

Thurairajah, B., R. L. Collins, V. L. Harvey, R. S. Lieberman, and K. Mizutani (2010a), Rayleigh lidar observations of reduced gravity wave activity during the formation of an elevated stratopause in 2004 at Chatanika, Alaska (65°N, 147°W), *J. Geophys. Res.*, *115*, D13109, doi:10.1029/2009jd013036.

Thurairajah, B., R. L. Collins, V. L. Harvey, R. S. Lieberman, M. Gerding, K. Mizutani, and J. M. Livingston (2010b), Gravity wave activity in the Arctic stratosphere and mesosphere during the 2007–2008 and 2008–2009 stratospheric sudden warming events, *J. Geophys. Res.*, *115*, D00N06, doi:10.1029/2010jd014125.

Toon, O. B., and R. P. Turco (1991), Polar Stratospheric Clouds and Ozone Depletion, *Scientific American*, *264*(6), 68-74, doi:10.1038/scientificamerican0691-68.

USNO (2012), *Sun or Moon Altitude/Azimuth Table*, United States Naval Observatory, March 2012, <http://aa.usno.navy.mil/data/docs/AltAz.php>.

USSA (1976), *United States Standard Atmosphere*, 241pp., NOAA-S/T 76-1562U.S. Gov. Printing Office, Washington D.C.

Varney, R. H., M. C. Kelley, M. J. Nicolls, C. J. Heinselman, R. L. Collins (2011), The electron density dependence of polar mesospheric summer echoes, *J. Atmos. Sol. Terr. Phys.*, *73*, 2153-2165, doi:10.1016/j.jastp.2010.07.020.

Verdeyen, J. T. (1981), *Laser electronics*, 444 pp., Prentice-Hall, Inc., New Jersey.

von Zahn, U., G. von Cossart, J. Fielder, K. H. Fricke, G. Nelke, G. Baumgarten, D. Rees, A. Hauchecorne, K. Adolfsen (2000), The ALOMAR Rayleigh/Mie/Raman lidar: objectives, configuration, and performance, *Ann. Geophsysicae., 18*, 815-833, doi:10.1007/s00585-000-0815-2.

Wallace, J. M., and P. V. Hobbs (2006), *Atmospheric science: An introductory survery*, 483 pp., Elsevier Academic Press, Massachusetts.

Wang, W. (2003), *Spectral estimation of signal and noise power in Rayleigh lidar measurements of the middle atmosphere*, MS Thesis, University of Alaska Fairbanks.

Weitkamp, C. (2005), *Lidar: Range resolved optical remote sensing*, 460 pp., Springer, Singapore.

Whiteway, J. A., A. I. Carswell, and W. E. Ward (1995), Mesospheric temperature inversions with overlying nearly adiabatic lapse rate: An Indication of a well-mixed turbulent layer, *Geophys. Res. Lett.*, *22*(10), 1201-1204, doi:10.1029/95gl01109.

Wu, D. (2000), Mesospheric temperature inversion layers: Recent observations from UARS ISAMS and MLS, *Recent Res. Devel. Geophys., 3*, 37–44.

Appendix A. Chapter 3 Tables

Table A.1. Lidar signal statistics for the 24-inch telescope measurements on 18–19 February 2012 (2245–0654 LST).

Altitude (km)	Total Signal, N_{TOT}[1,2] (Photon count)	Signal, N_S[1,2,3] (Photon count)	Relative Error $\Delta N_S/N_S$ (%)
42.5	193734	193726	2.3×10^{-1}
47.5	71403	71396	3.7×10^{-1}
52.5	28214	28207	6.0×10^{-1}
57.5	11899	11892	9.2×10^{-1}
62.5	5422	5414	1.4×10^{0}
67.5	2497	2489	2.0×10^{0}
72.5	1049	1041	3.1×10^{0}
77.5	432	425	4.9×10^{0}
82.5	185	178	7.7×10^{0}
87.5	81	73	1.2×10^{1}
92.5	35	27	2.2×10^{1}
97.5	19	11	3.8×10^{1}
102.5	11	4	9.0×10^{1}

1: Signals are averaged over 5 km altitude and represents signal in 75 m range bins

2: Numbers are rounded to the nearest whole number

3: Background signal, $N_B + N_D = 7.6$ photon counts

Table A.2. Lidar signal statistics for the 41-inch telescope measurements on 18–19 February 2012 (2245–0654 LST).

Altitude (km)	Total Signal, N_{TOT}[1,2] (Photon count)	Signal, N_S[1,2,3] (Photon count)	Relative Error $\Delta N_S/N_S$ (%)
42.5	534641	534555	1.4×10^{-1}
47.5	197219	197133	2.3×10^{-1}
52.5	77527	77441	3.6×10^{-1}
57.5	32679	32593	5.5×10^{-1}
62.5	14816	14729	8.3×10^{-1}
67.5	6857	6771	1.2×10^{0}
72.5	2899	2813	1.9×10^{0}
77.5	1241	1155	3.1×10^{0}
82.5	559	473	5.0×10^{0}
87.5	282	196	8.6×10^{0}
92.5	161	75	1.7×10^{1}
97.5	116	30	3.6×10^{1}
102.5	99	13	7.8×10^{1}

1: Signals are averaged over 5 km altitude and represents signal in 75 m range bins

2: Numbers are rounded to the nearest whole number

3: Background signal, $N_B + N_D = 86.1$ photon counts

Table A.3. Lidar signal statistics for the 41-inch telescope measurements on 22–23 March 2012 (2133–2329 LST).

Altitude (km)	Total Signal, N_{TOT}[1,2] (Photon count)	Signal, N_S[1,2,3] (Photon count)	Relative Error $\Delta N_S/N_S$ (%)
42.5	47245	47227	4.6×10^{-1}
47.5	19137	19119	7.2×10^{-1}
52.5	8119	8101	1.1×10^{0}
57.5	3558	3540	1.7×10^{0}
62.5	1576	1558	2.5×10^{0}
67.5	680	662	3.9×10^{0}
72.5	281	263	6.4×10^{0}
77.5	123	105	1.1×10^{1}
82.5	63	45	1.8×10^{1}
87.5	37	19	3.2×10^{1}
92.5	24	6	7.9×10^{1}
97.5	20	2	2.0×10^{2}
102.5	20	2	2.7×10^{2}

1: Signals are averaged over 5 km altitude and represents signal in 75 m range bins

2: Numbers are rounded to the nearest whole number

3: Background signal, $N_B + N_D = 18.0$ photon counts

Table A.4. Lidar signal statistics for the 41-inch telescope measurements on 22–23 March 2012 (2359–0223 LST).

Altitude (km)	Total Signal, N_{TOT}[1,2] (Photon count)	Signal, N_S[1,2,3] (Photon count)	Relative Error $\Delta N_S/N_S$ (%)
42.5	91855	91820	3.3×10^{-1}
47.5	37537	37503	5.2×10^{-1}
52.5	15980	15946	7.9×10^{-1}
57.5	7041	7007	1.2×10^{0}
62.5	3095	3061	1.8×10^{0}
67.5	1347	1313	2.8×10^{0}
72.5	561	527	4.5×10^{0}
77.5	244	210	7.4×10^{0}
82.5	125	90	1.2×10^{1}
87.5	72	38	2.2×10^{1}
92.5	49	15	4.7×10^{1}
97.5	39	5	1.3×10^{2}
102.5	36	2	2.8×10^{2}

1: Signals are averaged over 5 km altitude and represents signal in 75 m range bins

2: Numbers are rounded to the nearest whole number

3: Background signal, $N_B + N_D = 34.3$ photon counts

Table A.5. Lidar signal statistics for 23–24 April 2008 (0007–0215 LST).

Altitude (km)	Total Signal, N_{TOT}[1,2] (Photon count)	Signal, N_S[1,2,3] (Photon count)	Relative Error $\Delta N_S/N_S$ (%)
42.5	45713	45704	4.7×10^{-1}
47.5	18486	18477	7.4×10^{-1}
52.5	7975	7966	1.1×10^{0}
57.5	3553	3543	1.7×10^{0}
62.5	1595	1586	2.5×10^{0}
67.5	717	708	3.8×10^{0}
72.5	323	314	5.7×10^{0}
77.5	140	131	9.0×10^{0}
82.5	60	51	1.5×10^{1}
87.5	28	19	2.7×10^{1}
92.5	16	7	6.0×10^{1}
97.5	12	3	1.2×10^{2}
102.5	9	0.2	1.3×10^{3}

1: Signals are averaged over 5 km altitude and represents signal in 75 m range bins

2: Numbers are rounded to the nearest whole number

3: Background signal, $N_B + N_D = 9.0$ photon counts

Table A.6. Lidar signal statistics for 23–24 April 2012 (0004–0211 LST).

Altitude (km)	Total Signal, N_{TOT}[1,2] (Photon count)	Signal, N_S[1,2,3] (Photon count)	Relative Error $\Delta N_S/N_S$ (%)
42.5	152822	152782	2.6×10^{-1}
47.5	64452	64412	3.9×10^{-1}
52.5	28580	28540	5.9×10^{-1}
57.5	13117	13077	8.8×10^{-1}
62.5	6082	6042	1.3×10^{0}
67.5	2761	2721	1.9×10^{0}
72.5	1194	1154	3.0×10^{0}
77.5	495	455	4.9×10^{0}
82.5	213	173	8.4×10^{0}
87.5	104	64	1.6×10^{1}
92.5	66	26	3.1×10^{1}
97.5	46	6	1.1×10^{2}
102.5	43	3	2.3×10^{2}

1: Signals are averaged over 5 km altitude and represents signal in 75 m range bins

2: Numbers are rounded to the nearest whole number

3: Background signal, $N_B + N_D = 40.0$ photon counts

Table A.7. Lidar signal statistics for 24–25 April 2012 (0002–0210 LST).

Altitude (km)	Total Signal, N_{TOT}[1,2] (Photon count)	Signal, N_S[1,2,3] (Photon count)	Relative Error $\Delta N_S/N_S$ (%)
42.5	168645	168617	2.4×10^{-1}
47.5	71425	71397	3.7×10^{-1}
52.5	31565	31537	5.6×10^{-1}
57.5	14221	14193	8.4×10^{-1}
62.5	6663	6635	1.2×10^{0}
67.5	3023	2995	1.8×10^{0}
72.5	1290	1262	2.8×10^{0}
77.5	530	502	4.6×10^{0}
82.5	220	192	7.7×10^{0}
87.5	97	70	1.4×10^{1}
92.5	54	26	2.8×10^{1}
97.5	35	7	7.9×10^{1}
102.5	29	1	4.2×10^{2}

1: Signals are averaged over 5 km altitude and represents signal in 75 m range bins

2: Numbers are rounded to the nearest whole number

3: Background signal, $N_B + N_D = 27.9$ photon counts

Table A.8. Comparison of power compensated lidar signals for April 2008 and 2012.

	24 April 2012		25 April 2012	
Altitude (km)	N_S/N_{S2008}	N_S^*/N_{S2008} [1]	N_S/N_{S2008}	N_S^*/N_{S2008} [1]
42.5	3.34	3.72	3.69	4.12
47.5	3.49	3.88	3.86	4.31
52.5	3.58	3.98	3.96	4.42
57.5	3.69	4.11	4.01	4.47
62.5	3.81	4.24	4.18	4.67
67.5	3.84	4.27	4.23	4.72
72.5	3.67	4.08	4.02	4.48
77.5	3.48	3.87	3.83	4.27
82.5	3.36	3.73	3.74	4.17
87.5	3.32	3.69	3.58	3.99
92.5	3.92	4.36	3.96	4.41
97.5	2.20	2.45	2.68	2.99
102.5	11.87	13.21	5.37	6.00

1: Signal compensated relative to April 2008 laser energy

Table A.9. Lidar signal statistics for the 24-inch telescope measurements on 28–29 March 2012 (2259–2358 LST).

Altitude (km)	Total Signal, N_{TOT}[1,2] (Photon count)	Signal, N_S[1,2,3] (Photon count)	Relative Error $\Delta N_S/N_S$ (%)
42.5	26098	26096	6.2×10^{-1}
47.5	10207	10206	9.9×10^{-1}
52.5	4311	4310	1.5×10^{0}
57.5	1906	1905	2.3×10^{0}
62.5	869	868	3.4×10^{0}
67.5	392	391	5.1×10^{0}
72.5	163	161	7.9×10^{0}
77.5	67	66	1.2×10^{1}
82.5	30	29	1.9×10^{1}
87.5	12	11	3.2×10^{1}
92.5	5	4	5.7×10^{1}
97.5	3	2	1.0×10^{2}
102.5	2	0.	2.6×10^{2}

1: Signals are averaged over 5 km altitude and represents signal in 75 m range bins

2: Numbers are rounded to the nearest whole number

3: Background signal, $N_B + N_D = 1.1$ photon counts

Table A.10. Lidar signal statistics for the 41-inch telescope measurements on 28–29 March 2012 (0035–0111 LST).

Altitude (km)	Total Signal, N_{TOT}[1,2] (Photon count)	Signal, N_S[1,2,3] (Photon count)	Relative Error $\Delta N_S/N_S$ (%)
42.5	104263	104251	3.1×10^{-1}
47.5	41268	41255	4.9×10^{-1}
52.5	17788	17776	7.5×10^{-1}
57.5	7932	7919	1.1×10^{0}
62.5	3544	3532	1.7×10^{0}
67.5	1605	1592	2.5×10^{0}
72.5	688	676	3.9×10^{0}
77.5	284	271	6.2×10^{0}
82.5	126	113	9.9×10^{0}
87.5	56	43	1.7×10^{1}
92.5	30	18	3.1×10^{1}
97.5	20	8	5.9×10^{1}
102.5	15	3	1.4×10^{2}

1: Signals are averaged over 5 km altitude and represents signal in 75 m range bins

2: Numbers are rounded to the nearest whole number

3: Background signal, $N_B + N_D = 12.6$ photon counts

Table A.11. Set by set acquisition method for 4 April 2012.

Time Period	Set Name	Telescope	Laser	Number Laser Pulses
0024–0051 LST	1/1-2/16	Cassegrain 41-inch	PL8020	3,200
0109–0117 LST	3/1-3/16	Cassegrain 41-inch	PL9030	1,600
0118–0132 LST	4/1-4/16	Cassegrain 41-inch	PL8020	1,600
0133–0141 LST	5/1-5/16	Cassegrain 41-inch	PL9030	1,600
0142–0156 LST	6/1-6/16	Cassegrain 41-inch	PL8020	1,600
0157–0205 LST	7/1-7/16	Cassegrain 41-inch	PL9030	1,600
0206–0219 LST	8/1-8/16	Cassegrain 41-inch	PL8020	1,600
0221–0229 LST	9/1-9/16	Cassegrain 41-inch	PL9030	1,600
0230–0243 LST	10/1-10/16	Cassegrain 41-inch	PL8020	1,600
0245–0253 LST	11/1-11/16	Cassegrain 41-inch	PL9030	1,600
0254–0307 LST	12/1-12-16	Cassegrain 41-inch	PL8020	1,600
0309–0317 LST	13/1-13/16	Cassegrain 41-inch	PL9030	1,600
0318–0331 LST	14/1-14/16	Cassegrain 41-inch	PL8020	1,600
0333–0341 LST	15/1-15/16	Cassegrain 41-inch	PL9030	1,600
0342 - 0355 LST	16/1-16/16	Cassegrain 41-inch	PL8020	1,600
0357 - 0414 LST	17/1-18/16	Cassegrain 41-inch	PL9030	3,200

Table A.12. Lidar signal statistics for the PL8020 measurements on 4 April 2012 (0024–0355 LST).

Altitude (km)	Total Signal, N_{TOT}[1,2] (Photon count)	Signal, N_S[1,2,3] (Photon count)	Relative Error $\Delta N_S/N_S$ (%)
42.5	116163	116015	2.9×10^{-1}
47.5	46874	46725	4.6×10^{-1}
52.5	20502	20353	7.0×10^{-1}
57.5	9245	9096	1.1×10^{0}
62.5	4275	4127	1.6×10^{0}
67.5	1997	1848	2.4×10^{0}
72.5	969	820	3.8×10^{0}
77.5	510	362	6.2×10^{0}
82.5	289	140	1.2×10^{1}
87.5	208	59	2.4×10^{1}
92.5	170	21	6.2×10^{1}
97.5	153	5	2.6×10^{2}
102.5	150	1	1.1×10^{3}

1: Signals are averaged over 5 km altitude and represents signal in 75 m range bins

2: Numbers are rounded to the nearest whole number

3: Background signal, $N_B + N_D = 148.6$ photon counts

Table A.13. Lidar signal statistics for the PL9030 measurements on 4 April 2012 (0024–0355 LST).

Altitude (km)	Total Signal, N_{TOT}[1,2] (Photon count)	Signal, N_S[1,2,3] (Photon count)	Relative Error $\Delta N_S/N_S$ (%)
42.5	272738	272567	1.9×10^{-1}
47.5	111316	111146	3.0×10^{-1}
52.5	48834	48664	4.5×10^{-1}
57.5	21881	21710	6.8×10^{-1}
62.5	10023	9852	1.0×10^{0}
67.5	4608	4437	1.5×10^{0}
72.5	2148	1978	2.3×10^{0}
77.5	1037	866	3.7×10^{0}
82.5	518	347	6.6×10^{0}
87.5	312	142	1.2×10^{1}
92.5	228	57	2.6×10^{1}
97.5	193	22	6.3×10^{1}
102.5	180	9	1.5×10^{2}

1: Signals are averaged over 5 km altitude and represents signal in 75 m range bins

2: Numbers are rounded to the nearest whole number

3: Background signal, $N_B + N_D = 170.6$ photon counts

Appendix B. SABER Temperature Retrieval in LTE and non-LTE Atmospheric Regions

B.1. Introduction

The Sounding of the Atmosphere using Broadband Emission Radiometry (SABER) is one of four instruments aboard NASA's Thermosphere Ionosphere Mesosphere Energetics Dynamics (TIMED) satellite. TIMED was launched on 7 December 2001 with the scientific objective of studying the mesosphere and lower thermosphere/ionosphere (MLTI) region to understand the energetics and resulting dynamics. The SABER instrument is a broadband limb-infrared radiometer operating from 1.27 to 15 μm (7865 to 650 cm^{-1}), developed with the goal of exploring the mesosphere and lower thermosphere (MLT) on a global scale to achieve a major improvement in the current understanding of the processes governing the structure, energetics, chemistry, dynamics, and transport in this region with high vertical resolution [Smith, 2010]. The thermal structure of the atmosphere is essential to exploring these processes.

The density decays exponentially with height in the atmosphere and can be assumed to be in hydrostatic balance under local-thermodynamic equilibrium (LTE). The assumption of LTE is correct in regions where the population densities of atmospheric molecules are governed solely by collisions. In regions above where LTE applies, atmospheric molecules are in a state of non-LTE where the physics is governed by collisions, radiation, and chemical reactions of the atmospheric constituents. The chemical and physical processes occurring in these two regions of the atmosphere differ greatly, and thus the determination of temperature from emission radiances will be governed by LTE or non-LTE processes depending on the altitude where the emission originated. SABER exploits the CO_2 15 μm band to study the thermal structure of the atmosphere.

This appendix presents a review of the SABER instrument and discusses the temperature retrieval algorithms in the LTE and non-LTE regions of the atmosphere using the recent

studies by Remsberg et al. [2008] and García-Comas et al. [2008]. In section B.2, the technique of limb emission scanning is reviewed and the SABER instrument is introduced. In section B.3, SABER retrievals of temperature from the CO_2 15 μm measured radiances are presented for both temperature versus pressure (T(p)) under LTE conditions, and kinetic temperature (T_k) under non-LTE conditions. The observed thermal structure from T(p) and T_k are shown and comparisons are highlight from Rayleigh lidar and a climatology from fall spheres. The random and systematic errors for T(p) and T_k are also shown. Section B.5 summarizes the key points and highlights the importance that SABER provides to the study of the middle atmosphere.

B.2. SABER experiment

The primary altitude range of interest to SABER extends from 60 km to 180 km and has been essentially unexplored on a global scale due to the difficulty in sounding the region from orbit using in-situ methods, as well as the past emphasis on studying the troposphere and stratosphere. SABER measures vertical horizon radiance profiles in ten broad spectral bands from 1.27 to 15 μm with high vertical resolution, as low as 2 km [Mertens et al., 2004]. SABER's limb is scanned vertically over an altitude range of ~400 km (~350 km in García-Comas et al., [2008]) to below the Earth's surface [Russell et al., 1999]. The application of SABER measurements are shown in Table B.1.

Table B.1. SABER measurements and applications[1].

Parameter	Wavelength (μm)	Application	Altitude Range (km)
CO_2	14.9 and 15.0	T, density, IR cooling rates, P(Z), non-LTE	10 - 130
O_3	9.3	O_3 conc., cooling rates, solar heating, chemistry inference of [O] and [H], and dynamics studies	15 - 105
$O_2(^1\Delta)$	1.27	O_3 conc. (day), inferred [O] at night, energy loss for solar heating efficiency	50 - 105
CO_2	4.3	CO_2 conc., mesosphere solar heating; tracer	85 - 150
OH (v)	2.1 and 1.6	HO_y chem., chemical heat source, dynamics, inference of [O] and [H], PMC studies	80 - 100
NO	5.3	Thermosphere cooling, NO_x chemistry	90 - 180
H_2O	6.9	HO_y source gas, dynamical tracer	15- 80

1: Adapted from Russell et al. [1999]

B.2.1 Limb scanning method

The technique of employed by a limb scanning radiometer has inherent advantages over a nadir viewing, or zenith pointing radiometer. These advantages are outlined by Liou [1980], and Russell et al. [1999] and are as follows:

- due to the exponential decrease in atmospheric density, the measured radiance comes from the few kilometers immediately above the tangent point, H0, which results in high vertical resolution
- unlike a nadir viewing radiometer, the radiance from the earth's surface is absent in the measurement and cold space is taken as the background signal
- high gas column density (30 to 60 times that in a nadir view) along the horizontal field of view allows for measurements of very tenuous atmospheric gases
- the viewing direction can be oriented in any azimuthal direction relative to the satellite motion and covers a large area

The limb scanning technique is most applicable for studying the stratosphere and mesosphere due to the horizontal ray path. Disadvantages arise in the presence of clouds,

which act as bodies of infinite opacity and which would considerably alter the measured radiance. Other disadvantages arise if there is horizontal discontinuity in the atmospheric state along the ray path [Liou, 1980]. These are important considerations when studying SABER radiances, especially in the presence of polar mesospheric clouds (PMCs), or when the limb is viewing high latitudes from south to north where temperature gradients may be large (i.e. in the presence of the polar vortex in winter).

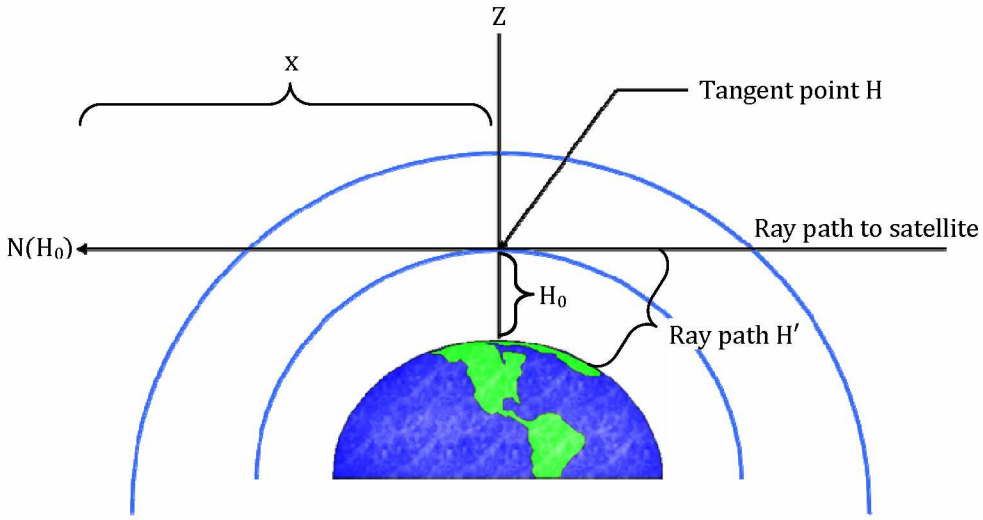

Figure B.1. Geometry of the SABER limb approach with a tangent height H_0 (adapted from Russell et al. [1999]).

The tangent height H_0 is the altitude of the point of closest approach of a ray pay from the earth (see H_0 compared to H' in Figure B.1). The measured radiance ($N(H_0)$) is a function of the tangent height and depends on the source function (J_ν),

$$N(H_0) \cong \iint_{\Delta\nu\Delta x} J_\nu(x) \frac{d\Gamma(\nu, q, T, p)}{dx} dx d\nu \qquad (B.1)$$

Where J_ν is a function of the wavenumber (ν), and the distance along the ray path (x) originating at H_0. Under non-LTE conditions, J_ν is determined by the relative populations

of the upper and lower states of the observed transitions, which are dependent on the relative importance of collisional, radiative and chemical excitation and loss processes. The transmission (Γ) depends on ν, the mixing ratio (q), temperature (T), and pressure (p). Non-LTE processes must also be taken into consideration when calculating Γ [Russell et al., 1999]. The weighting function ($d\Gamma/d\tau$) is defined as the derivative of transmission with respect to optical depth (τ).

The CO_2 15 μm measured radiances are used to infer temperature because the mixing ratio is assumed to be well known in the atmosphere. Radiances measured from other spectral bands are then used to infer species specific mixing ratio. For example, $q(O_3)$ is inferred from the channel-4 radiances. Liou [1980] illustrated the weighting function of a hypothetical instrument with an infinitesimal vertical field-of-view (FOV) and a wide spectral band covering most of the 15 μm CO_2 band (585–705 cm^{-1}), Figure B.2a. From Figure B.2a, it is clear that for tangent heights above 25 km the major contribution to the measured radiance comes from within the few kilometers above the tangent height. Below about 25 km, the weighting function broadens and does not decrease with height as sharply and more resembles the nadir viewing weighting function [Liou, 1980].

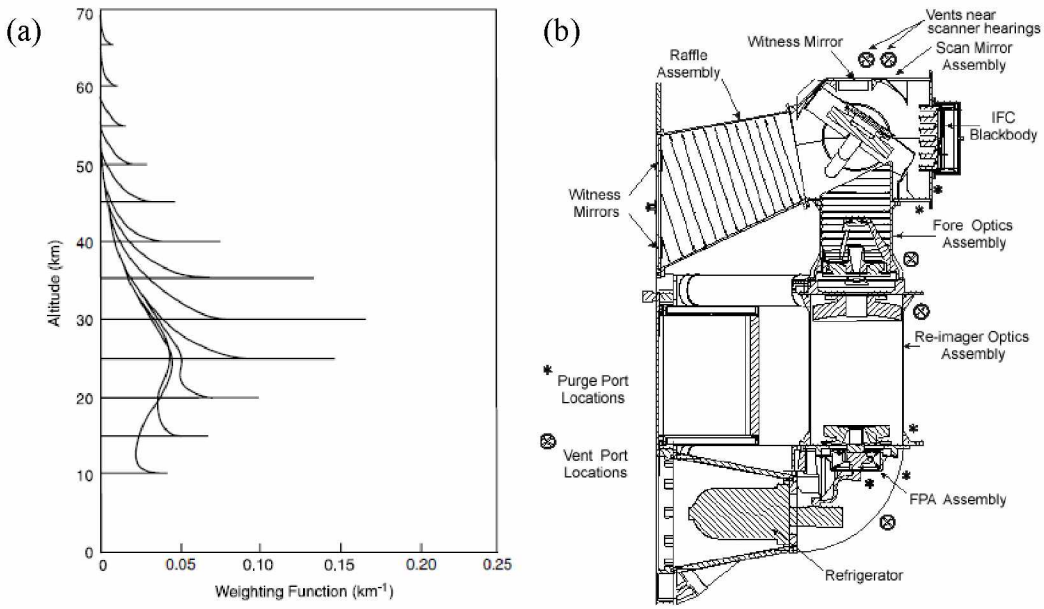

Figure B.2. (a) Limb viewing weighting function for an ideal instrument with a spectral band of 585–705 cm^{-1} [Liou, 1980] and (b) cross sectional view of the SABER instrument [Smith, 2010].

SABER's wide band CO_2 channel (channel-3) extends from 580–763 cm^{-1} and has an instantaneous field-of-view (IFOV) of 1.49 km [Remsberg et al., 2008]. Note: García-Comas et al. [2008] report channel-3 extending from 570–780 cm^{-1}. The extent of SABER's channel-3 spectral band is similar to the idealized case of Liou [1980] in that it encompasses most of the 15 μm CO_2 band, but with a larger spectral band pass and a realistic IFOV. The channel-3 weighting function would look similar to Figure B.2a, but with a broader, less "peaky" shape. The weighting functions would also blur together because the measured radiances come from an altitude distribution (due to the IFOV) rather than the idealized infinitesimal FOV.

B.2.2. SABER instrument

SABER measures radiances emitted from the terrestrial atmosphere in ten spectral bands from 1.27 to 15 μm. Further information on the design of SABER can be found in references from the Nimbus 7 Limb Infrared Monitor of the Stratosphere (LIMS) because

measurement and retrieval concepts developed for SABER has its heritage from LIMS [Remsberg et al., 2008]. SABER was developed at the Utah State University Space Dynamics Laboratory. A cross sectional view of SABER is shown in Figure B.2b. A detailed description of the instrument is not explicitly discussed in this appendix but can be found in Russell et al., [1999].

B.3. SABER temperatures

The structure of the thermal atmosphere is crucial to understanding the energetics and dynamics of the atmosphere, one of SABER's primary scientific objectives [Russell et al., 1999; Smith, 2010]. The retrieval of SABER temperatures requires two retrieval algorithms due to the differing dynamical and chemical processes that govern the structure of the atmosphere above and below ~65–70 km. This altitude range is important because it is in the region where the condition of LTE no longer governs the population densities of atmospheric molecules. Below approximately 65 km to 70 km, the SABER temperature retrieval algorithm relies on the assumption that the atmosphere is in LTE to retrieve T(p). Above approximately 65 km to 70 km, SABER uses non-LTE algorithms in the retrieval of T_k.

Two channels (originally three) are devoted to registering the radiances from the CO_2 15 μm band because their radiances are utilized in the retrieval of both T(p) and T_k. García-Comas et al. [2008] reported the band pass where the transmittances of the filters fall to 5% for channel-1 as 635–710 cm^{-1}, and channel-3 as 570–780 cm^{-1}. Whereas Remsberg et al. [2008] report the channel-1 and channel-3 band passes as 649–698 cm^{-1} and 580–763 cm^{-1}, respectively.

B.3.1. CO_2 15 μm bands

García-Comas et al. [2008] examined the responses of the non-LTE retrieval to changes in the collisional parameters, presented the behaviors of the CO_2 vibrational level populations (Figure B.4), and their contributions to the SABER 15 μm channels (Figure B.5). García-Comas et al. [2008] adopted the Herzberg notation to refer to the

vibrational levels, i.e., (υ_1, υ_2^1, υ_3), where υ_1 is the level excited in the symmetric stretching, υ_2 and υ_3 are the excited levels of the bending and asymmetric stretching modes, respectively (Figure B.3). The superscript in υ_2^1 represents the vibrational angular momentum quantum number. The authors also denote the CO_2 isotopes using the last digit of the atomic weight of each atom. For example, the $^{12}C^{16}O_2$ isotope is referred to as 626.

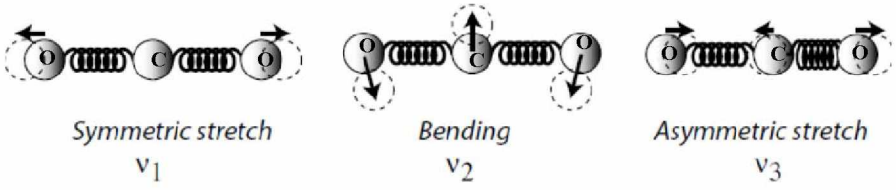

Figure B.3. Vibrational levels of triatomic molecules such as CO_2 (adapted from Petty [2006]).

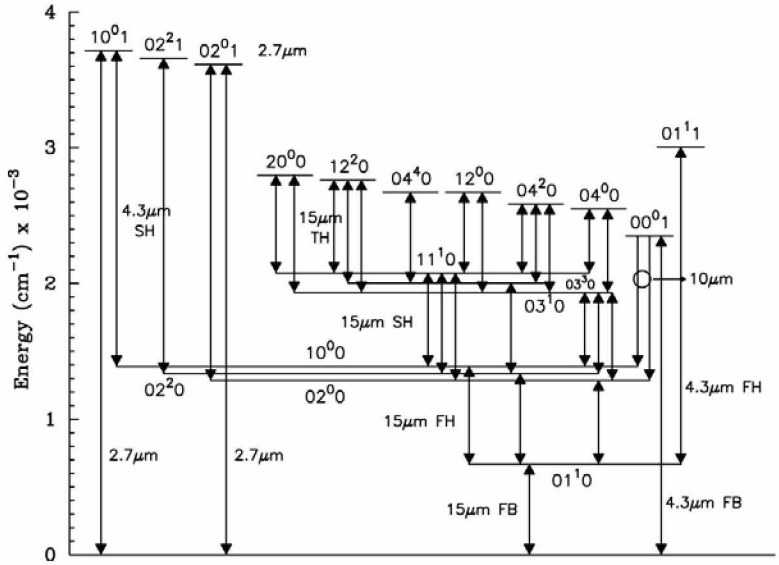

Figure B.4. Main CO_2 vibrational state energies. Arrows indicate the main CO2 bands emitting at 4.3, 10, and 15 μm, where FB is the fundamental band, first hot band FH, second hot band SH, and third hot band TH [García-Comas et al., 2008].

In Figure B.4, the 15 μm fundamental band (FB) is the 01^10–00^00 transition, and the 15 μm first hot band (FH) are the transitions from the 10^00, 02^20, and 02^00 levels to the 01^10

level. These population levels and transitions are important to consider at non-LTE altitudes, where the populations of energy levels are governed by the conflict between radiative and collisional effects. The collisional adjustment rate of the state populations is determined by a relaxation time proportional to the pressure and the rate of radiative adjustment is determined by the natural lifetime of the excited states with respect to radiative transitions [Liou, 1980].

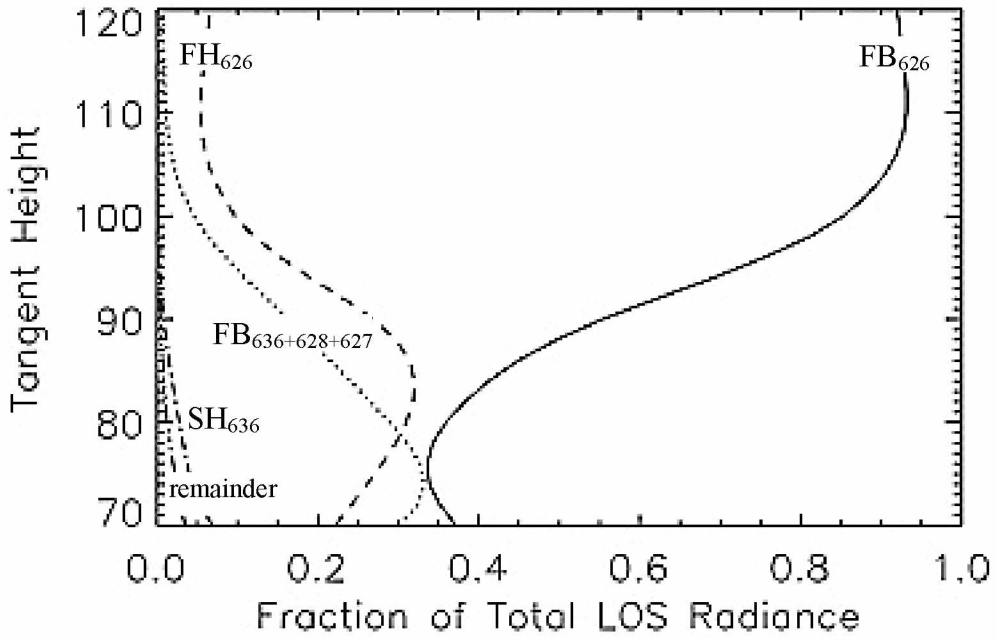

Figure B.5. Fractional contribution of CO_2 vibrational bands to SABER channel-1 simulated radiance for a typical midlatitude profile (adapted from García-Comas et al. [2008]).

Figure B.5 illustrates the relative contributions from different isotopes and vibrational bands in the 15 μm total channel-1 radiance at non-LTE altitudes. These contributions reflect the general behavior but are variable under different atmospheric conditions, e.g., a strong thermal inversion. The main contributor to the 15 μm channel-1 total radiance at all altitudes is the 626-CO_2 υ_2 fundamental band, denoted FB_{626}. Below 80 km the contribution of the minor isotopes (636, 628, and 627) fundamental bands is the next largest contributor, reaching a maximum of 30% of the 15 μm total radiance at 75 km. At

85 km the 626 isotope first hot band contributes about 30%, and is the second largest contributor to the 15 μm total radiance at all altitudes above. The "remainder" (dash-triple-dotted line in bottom left corner) is the contribution from the rest of the CO_2 hot bands and the ozone υ_2 fundamental band.

B.3.2. LTE T(p) retrieval

Under LTE conditions, T(p) is retrieved using SABER channel-1 and channel-3. The assumption that the atmosphere is in a condition of LTE is crucial to the determination of T(p) because it allows radiative effects to be neglected. The algorithm and assumptions presented in this appendix follow Remsberg et al., [2008],

- CO_2 mixing ratio is constant throughout the middle atmosphere
- The increased rate of q_{CO2} is annually updated with values from NOAA ground monitoring sites and lagged by four years to account for transport
- CO_2 line parameters (from HITRAN 2000 line list) were modified to account for the effects of CO_2 in its Q branch
- The effects of line coupling in the P and R branches were not included in the forward model

The model also considers the contribution to the observed radiances from other species. For example, the radiances measured for channel-1 through channel-3 have contributions from O_3, N_2O, H_2O, and N_2O_5 (contribution << 1% and is not modeled). However, the contribution from water vapor is non-negligible above the troposphere. N_2O contributes no more than 1% of the radiance in channel-2 and channel-3 above 30 km. O_3 contributions to the Channel-1 (channel-3) measured radiances are 25% (23%), 15% (18%), 10% (14%), and 5% (10%) at 20 km, 30 km, 40 km, and 50 km, respectively.

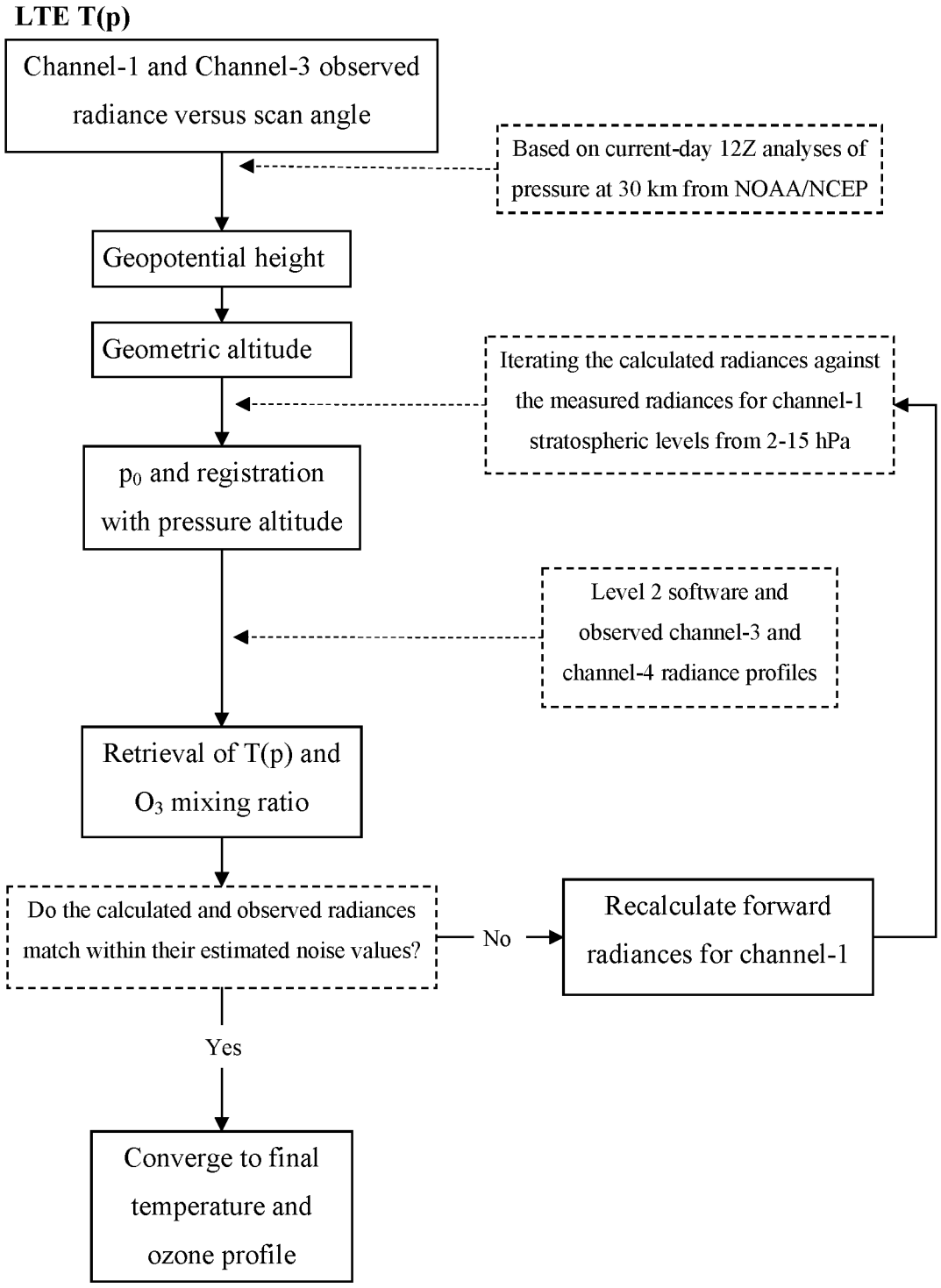

Figure B.6. Simplified T(p) retrieval (adapted from Remsberg et al. [2008]).

Remsberg et al., [2008] conclude that the iterative approach of the LTE algorithm leads to a convergence of T(p) and ozone solutions that may be slightly biased due to the 15 μm limb radiance technique used with only two channels. The bias in the retrieved pressure profiles affect the registration of SABER radiances to high altitudes in the atmosphere. The combined effects of uncertainties for a single LTE T(p) profile are given in Table B.2.

Table B.2. Random and systematic errors for SABER LTE T(p)[1,2].

	Pressure (hPa)						
	100	50	10	3	1	0.4	0.1
	Random (or Precision)						
Pointing jitter (±20 m)	0.3	0.3	0.3	0.6	0.6	0.6	0.5
Noise	0.1	0.1	0.1	0.1	0.2	0.3	0.5
	Systematic (Accuracy)						
CO_2 forward model (<0.2–0.7%)	0.6	0.6	0.7	0.6	0.2	0.2	0.2
Channel-3 radiance error (+1%)	1	1	-0.1	-1.3	-1.6	-1.5	-1
Pressure registration shift (bottom, 15–10 hPa)	-0.5	-0.3	0	0.5	0.8	1	0.8
O_3 correction error (-10%)	-0.5	0.3	0.2	-0.1	-0.5	-0.7	-0.7
Root-sum-square (±) of random and bias errors	1.4	1.3	0.8	1.6	2	2.1	1.6

1: Units are in Kelvin
2: Adapted from Remsberg et al. [2008]

B.3.3. Non-LTE T_k retrieval

In atmospheric regions where non-LTE processes dominate, the population densities of atmospheric constituents are no longer dominated solely by collisions, but are also governed by radiation and chemical reactions. The following algorithm and assumptions were taken from García-Comas et al., [2008]. The non-LTE operational algorithm for the retrieval of T_k is composed of the forward model and the inversion model. For a detailed

description of the algorithm see Mertens et al. [2002]. The temperatures were retrieved assuming the following [García-Comas et al., 2008],

- CO_2 volume mixing ratio from monthly and diurnal averages from WACCM
- N_2, O_2, nighttime O, and daytime O above 95 km volume mixing ratio from NRL-MSISE-90
- SABER daytime O below 95 km as inferred from the O_3 retrieval of SABER 1.27 μm channel
- Nominal values of the collisional rate coefficients.
- The non-LTE T_k is merged with the LTE T_k at an altitude around 65 km

The BANDPAK algorithm is used in the forward calculations at 15 μm includes all known excitation and relaxation mechanisms of the states. These include collisional processes, i.e., thermal collisions, vibrational energy transfer, and electronic to vibrational energy transfer, as well as radiative processes, i.e., energy exchange between atmospheric layers, absorption of solar radiation, spontaneous and induced emission. The retrieval of T_k in non-LTE conditions is susceptible to biases due to thermal variability and trends in the long term (seasonal) and short term (wave-driven dynamics). This seasonal dependence can be seen in Figure B.8 and Figure B.9.

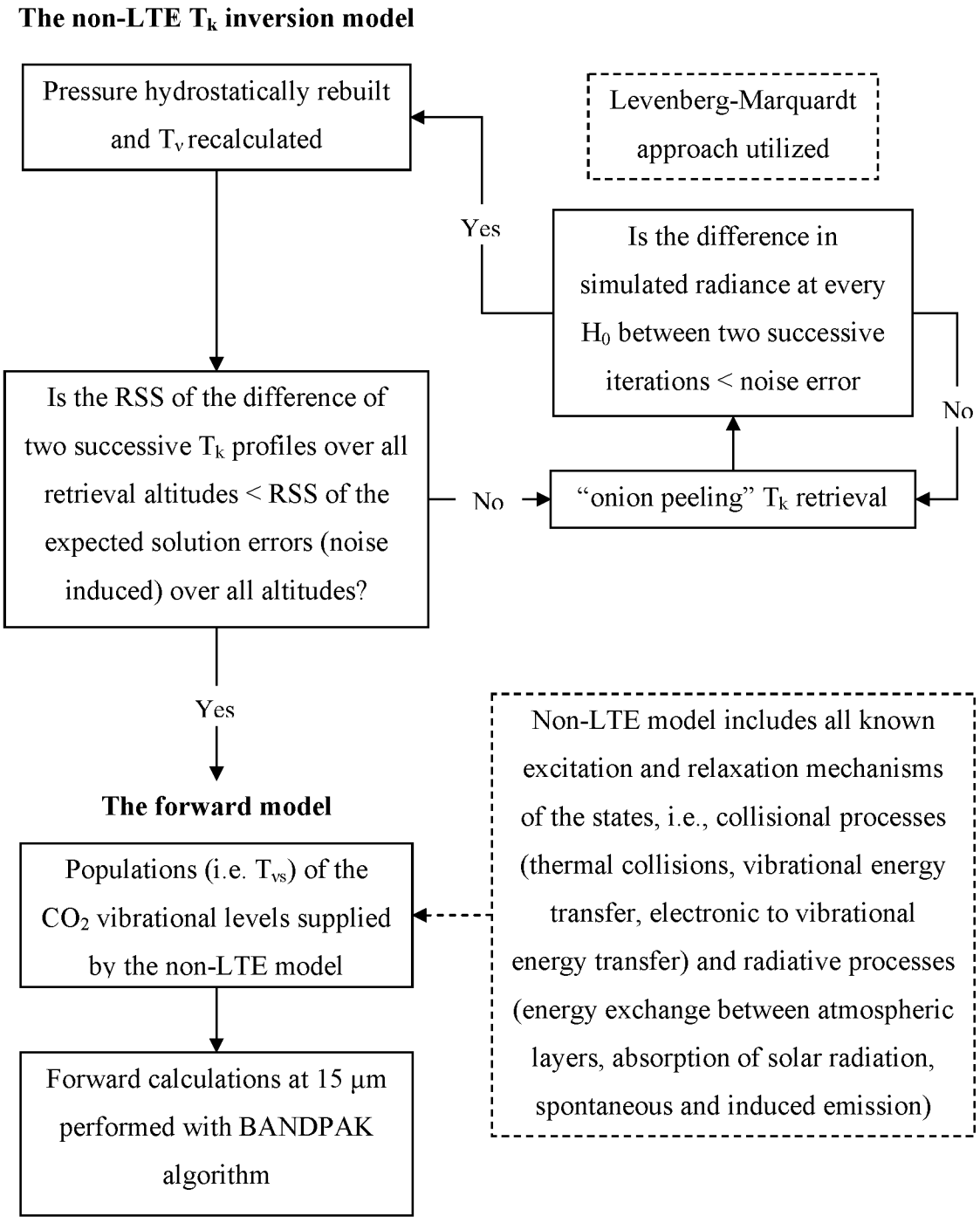

Figure B.7. Simplified T_k retrieval (adapted from García-Comas et al. [2008]).

Figure B.8 shows the SABER T_k on equinox (day 78) and solstice (day 197) with nearly global coverage due to the days being selected on a yaw maneuver (satellite views radiances from 82°S to 82°N). On equinox, the temperature structure follows a roughly latitudinal temperature dependence with some tidal or wave structure in the mesosphere region. For the case of solstice, there is a clear departure from latitudinal structure in the polar summer. The polar summer mesopause is much colder than at other locations or during other seasons, and is coupled with a warmer stratosphere below.

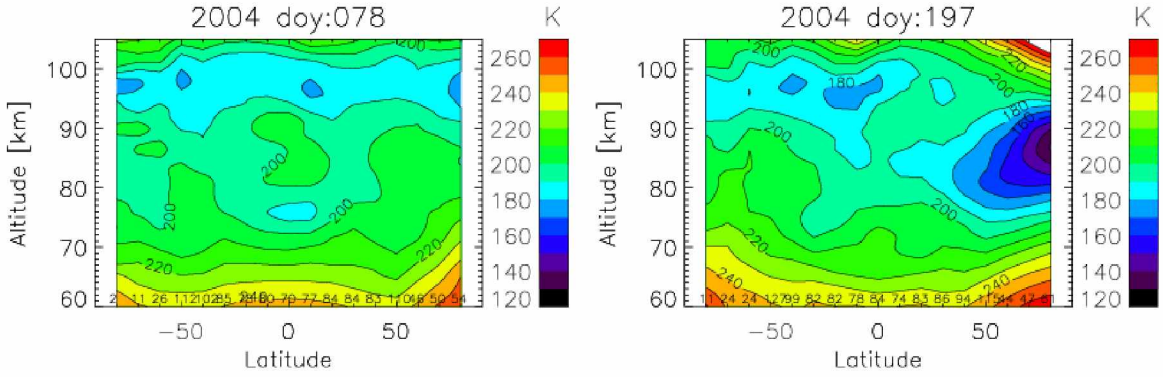

Figure B.8. SABER v1.07 kinetic temperatures for equinox (18 March 2004) and solstice (15 July 2004). The contours are every 10 K. The numbers along the bottom x axis indicate the number of averaged profiles [García-Comas et al., 2008].

During polar summer conditions, the cold mesopause and warmer stratospheric temperatures below leads to vibrational level populations being farther away from LTE. This is because the upwelling radiation from lower levels into the mesosphere is absorbed by molecules and the vibrational temperatures are able to overcome the kinetic temperatures. In midlatitudes and the polar winter, the mesopause is not as low and the absorption of upwelling radiation is not enough for the vibrational temperatures to overcome the local kinetic temperature. This can be seen clearly in Figure B.9 which shows the vibrational temperatures (dashed/dotted lines) and the average kinetic temperature (solid line) for the typical atmospheric scenario at midlatitudes (15 January 2003), polar winter and polar summer (15 July 2004). The zonal means were calculated

using all SABER temperature profiles measured within 10° latitude bins [García-Comas et al., 2008].

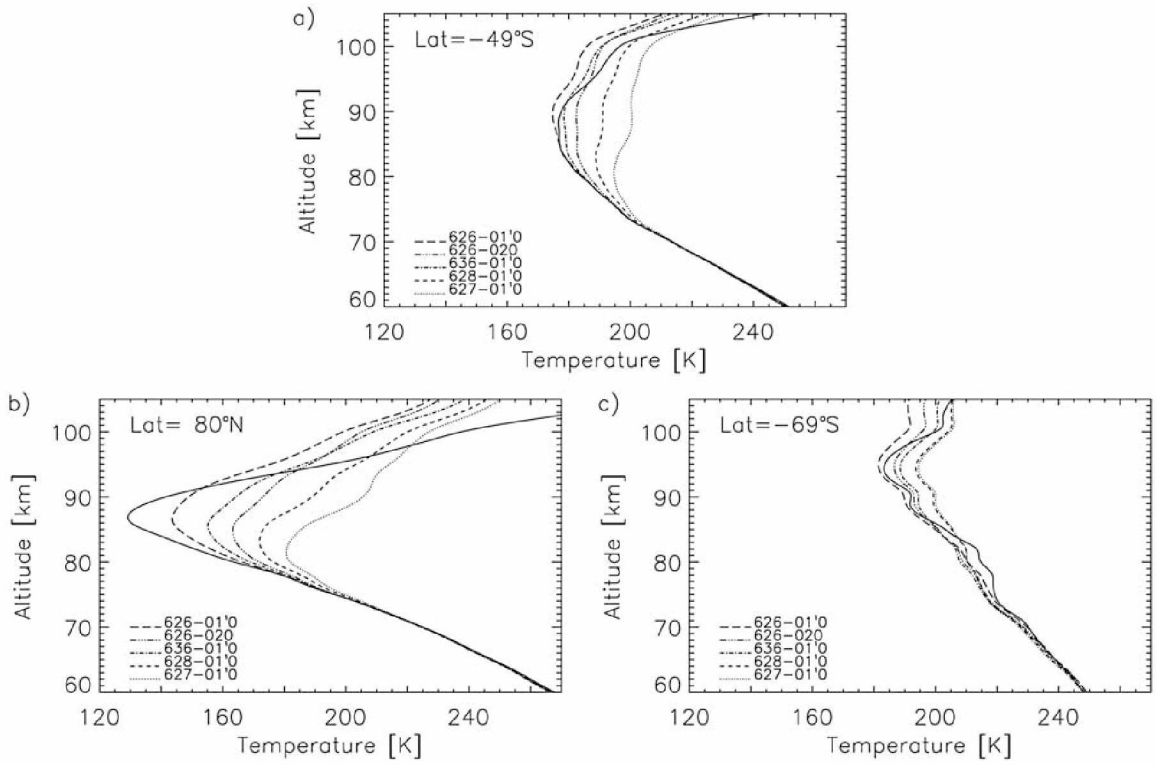

Figure B.9. SABER vibrational temperatures of the main CO2 υ2 vibrational states contributing to the 15-μm channel typical of (a) midlatitudes, (b) polar summer, and (c) polar winter. The profiles are zonal means for 10° latitude boxes at the average latitude shown. The solid line is the kinetic temperature [García-Comas et al., 2008].

Above 90 km, the 626-01^{1}0 level population T_v is smaller than T_k because collisions are not frequent enough to counteract the emission to space in the 01^{1}0-00^{0}0 band. Errors in the retrieved kinetic temperature increase for larger departures from LTE because there is a larger impact of perturbations of the collisional rates [García-Comas et al., 2008]. The non-LTE RSS uncertainties for T_k are given in Table B. for both midlatitude and polar summer conditions.

Table B.3. Random and systematic errors for SABER non–LTE T_k for the upper mesosphere and lower thermosphere for midlatitude and polar summer[1,2].

	Altitude (km)				
	80	85	90	95	100
	Random				
Noise (one scan)	1.8 (2.7)	2.2 (5.4)	3.6 (8.9)	5.4 (10.3)	6.7 (8.9)
	Systematic				
CO_2 (see text)	1.3	2.8	3.6	3.2	1.4
k_o or [O] by +50%	-0.2 (-0.1)	-0.5 (1.2)	-0.5 (-1.2)	-0.6 (-5.4)	-1.7 (-9.8)
k_o or [O] by -50%	0.3 (-0.3)	1.2 (-1.6)	1.7 (3.8)	1.8 (12.1)	4.7 (23.3)
kvv_min	-0.5 (-4.1)	-0.3 (-5.2)	0.1 (1.6)	0.1 (2.7)	0.1 (2.5)
kvv_max	0.1 (1.2)	0.1 (2.6)	-0.1 (-0.6)	-0.1 (-1.3)	-0.1 (-1.3)
Root-sum-square (±) of random and bias errors	2.3 (5.3)	3.8 (8.2)	5.4 (10.4)	6.5 (16.4)	8.4 (25.8)

1: Units are Kelvin with summer values given in parentheses
2: Adapted from Remsberg et al. [2008]

B.3.4. Observed thermal structure

Remsberg et al., [2008] presented the quality of SABER T(p) for the stratosphere and mesosphere through comparisons with averaged temperatures from the U.K. Met Office (MetO), Rayleigh lidar profiles, and various satellite data sets. The authors presented the quality of SABER temperatures in the UMLT region through comparisons with temperatures from airglow measurements, Na lidar measurements, and a climatology from falling spheres. This appendix presents the comparisons with Rayleigh lidar data from Table Mountain, CA (34°N), and the UMLT temperature comparison with the falling sphere climatology of Lübken [1999]. The analysis and details from the full comparisons can be found in Remsberg et al., [2008].

B.3.4.1. T(p) comparison with Rayleigh lidar

Comparisons with Rayleigh lidar were made in terms of T(z) because it is the natural retrieval product due to the time-of-flight range resolved lidar backscatter. The lidar temperature profile represents temperatures from a narrow vertical slice of the atmosphere at a specific geographic location whereas the SABER T(z) represents the temperatures derived over much larger volume. The comparison uses SABER data available within 2 degrees of latitude, 5 degrees of longitude, and 2 hours in time of the lidar data for the purpose of looking at the best available common volume (i.e., when SABER is viewing the same structure as the lidar).

Figure B.10 shows coincident profiles from the Table Mountain site on 8 June, 2002, and 9 October, 2002. The right profiles are the associated SABER minus lidar differences and the total error (shading) from the lidar data. We can see that SABER vertical features in T(p) agree quite well with the lidar.

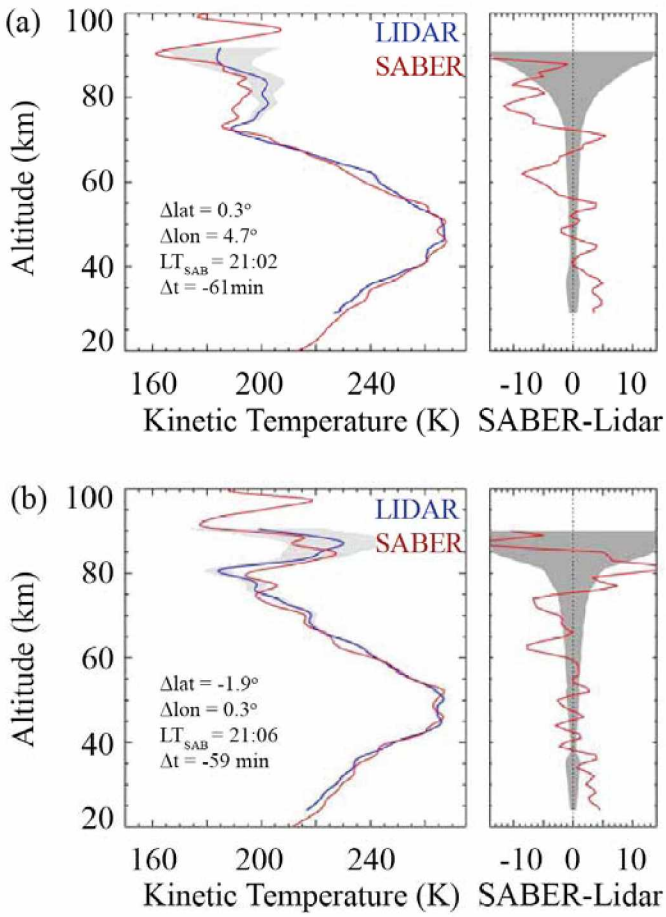

Figure B.10. (a) SABER V1.07 T(z) profile (red curve) compared with a Rayleigh lidar sounding (blue curve) at Table Mountain, California, for 8 June 2002. Right profile shows SABER minus lidar result (in K); shading in the vertical represents the combination of random and systematic errors from the lidar measurement. Average time difference is 61 minutes for the two soundings. (b) As in Figure 9a but for 9 October 2002 (adapted from Remsberg et al. [2008]).

Figure B.11 shows the SABER minus lidar differences for four yearly averages (2002 – 2005). The combined systematic and random errors for the lidar profiles are shaded and the right profile contains an estimate of the precision for the differences and an estimate of the precision of the SABER data (shaded). The differences are negatively biased below 40 km and change to positive above, with the exception of ~50 km and for some years in

the upper mesosphere. These results are similar to the comparison with Rayleigh lidar data from Mauna Loa, HI (20°N).

The bias for SABER temperatures to be higher than lidar below 40 km is consistent with the fact that ozone measured by SABER is less than reported by the MIPAS satellite data near 40 hPa hPa. This is an expected result if the associated SABER temperatures are too high for the retrieval of the 9.6 μm ozone from its radiances. The SABER temperatures are generally lower than lidar in the mesosphere which is consistent with an under prediction of the 4.3 μm radiances [Remsberg et al., 2008].

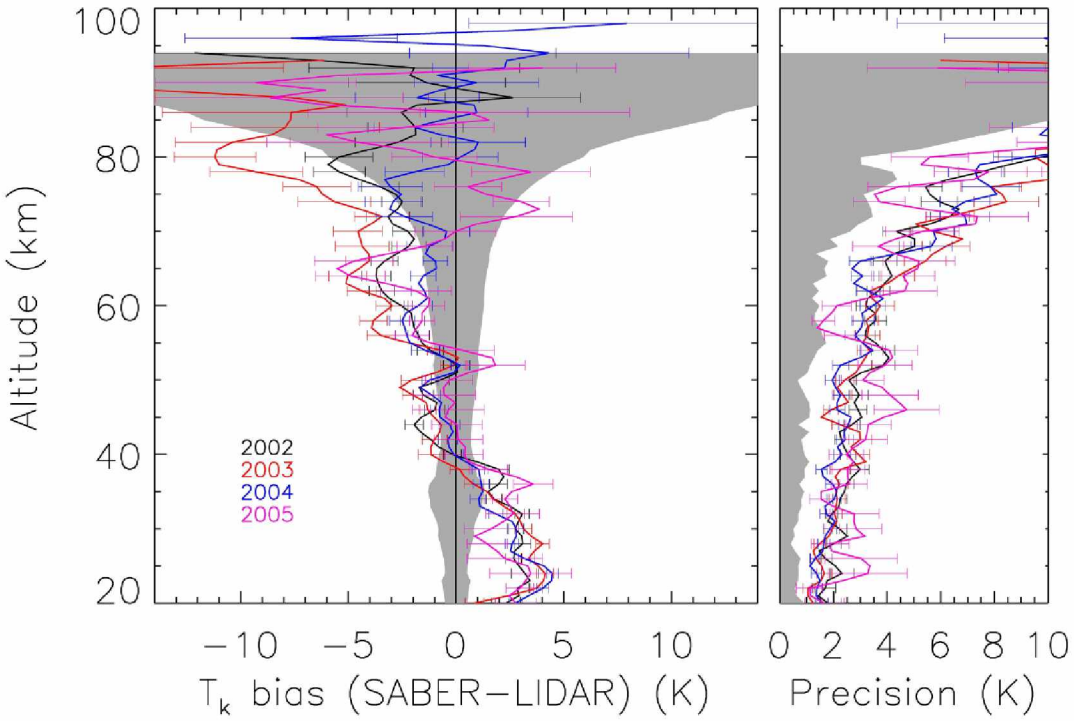

Figure B.11. Profile of the average temperature differences, SABER minus Rayleigh lidar, from the sets of profile pairs at Table Mountain for 2002 (39 pairs), 2003 (25 pairs), 2004 (28 pairs), and 2005 (8 pairs). Shaded region is the combined random and systematic error for the lidar data. The average variability of the paired differences for each year is to the right, along with the estimated precision for the SABER profiles (shaded) [Remsberg et al., 2008].

B.3.4.2. Temperature comparison with falling sphere climatology

It is unreasonable to expect excellent agreement between individual SABER profiles and falling sphere measurements in the polar summer mesopause because the retrieval of T_k for the polar summer mesopause region is subject to larger uncertainties [García-Comas et al., 2008], and the atmosphere experiences significant interannual variability. Therefore, a comparison with a15 July temperature climatology [Lübken, 1999] is made using July averages of SABER profiles for each year 2002-2007. The uncertainties for sphere profiles are 7 K, 3 K, and 1.5 K at 90, 80, and 70 km respectively.

Figure B.12 shows the comparison for the SABER profile 6-year zonal mean average at both 69°N (a) and poleward of 70°N (b). The horizontal bars are the range of the means of the individual years about the average and not the standard deviation of the individual profiles, which is larger. At 69°N, SABER agrees with the climatology (taking into account the combined errors) from approximately 68 km to 86 km and is higher from 86 km to 93 km. The SABER temperatures are lower below 65 km which agree with the lidar comparisons at that altitude.

For latitudes poleward of 70°N (Figure B.12b), the comparison shows improved agreement but with a mesopause altitude ~1.5 km lower than the climatology. Remsberg et al., [2008] noted that SABER measurements in the UMLT region at this latitude are for twilight conditions, and the SABER forward model is based on its assumed nighttime conditions for solar zenith angle > 85 degrees. However, the meridional temperature gradient is essentially zero poleward of 69°N and nearly every SABER profile has a solar zenith angle of less than 85 degree. Therefore, this comparison provides a validation of the SABER daytime algorithm which makes use of retrieved profiles of [O] at 90 km and below.

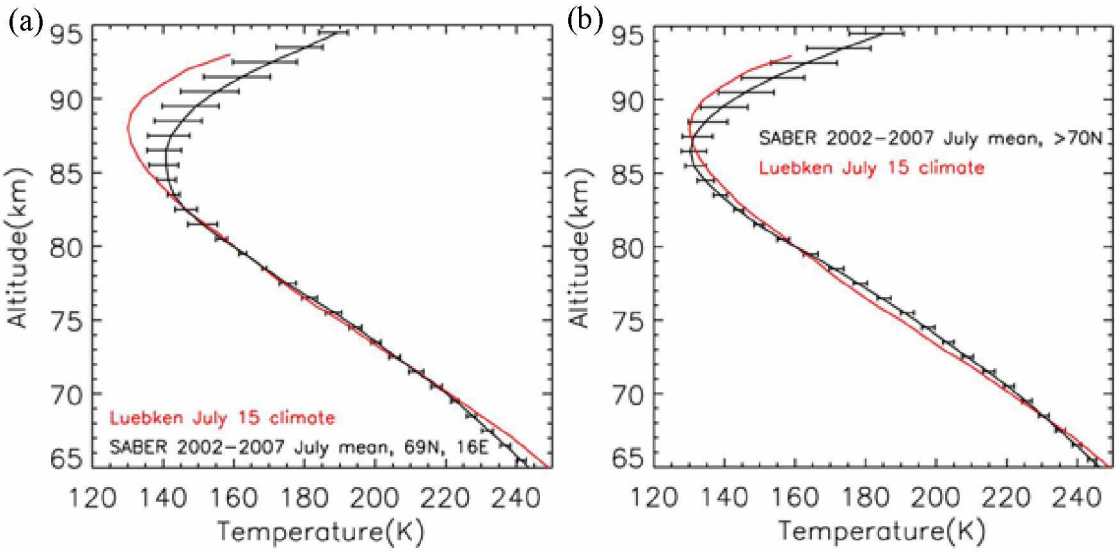

Figure B.12. Comparison of SABER temperature profile for July with the falling sphere climatology for 15 July at (a) 69°N and (b) of 70°N. The horizontal bars are the annual differences about the 6-year average [Remsberg et al., 2008].

The random and systematic errors for SABER LTE T(p) and non-LTE T_k are presented in Table B.2 and Table B.3. Overall, the SABER instrument is able to retrieve temperatures with good precision and the study of small-scale variability is possible throughout most regions.

B.4. Summary

The SABER instrument aboard the TIMED satellite is able to provide data with high vertical resolution due to its limb sounding geometry. SABER T_k provides the opportunity to achieve a deep understanding of the physics for the MLT. The non-LTE algorithm improves the T_k retrieval for extreme situations, such as polar summer. Under polar summer conditions, the CO_2 level populations are farther away from LTE due to the increased vibrational temperatures from upwelling radiation from lower levels. This departure from LTE makes the vibrational temperatures more sensitive to changes in the collisional rates which lead to larger errors in the retrieved T_k.

SABER provides unprecedented quality temperature data in regions under both LTE and non-LTE conditions. It is important to have confidence in the retrieval algorithms for the study of long term climate changes.